DISSERTATION

Non-linear Dynamics in Cavity QED: Beyond Two Coupled Springs

zur Erlangung des akademischen Grades eines

Doktors der Naturwissenschaften

eingereicht von

DI Andreas Angerer
Nattergasse 22
1170 Wien

ausgeführt am Atominstitut
der Fakultät für Physik der Technischen Universität Wien

unter der Leitung von
Univ. Ass. Dr. Johannes Majer
und
Univ. Prof. Dr. Hannes-Jörg Schmiedmayer

. . . .
Andreas Angerer

Gutachter:

. . . .	. . . .	. . . .
Univ. Ass. Dr. J. Majer	Univ. Prof. Dr. F. Marquardt	Univ. Prof. Y. Nakamura

Wien, am 28.05.2019

Abstract

Hybrid quantum systems no doubt will play a prominent role in the implementation of quantum technologies in the coming century, due to their versatility and potential in control and manipulation of (complex) quantum systems. Bringing these systems into the realm of solid state physics is the next logical step in scaling up these technologies and making them interesting to use in large scale applications. Many experiments have shown such an implementation in solid state devices and many realizations of quantum technologies nowadays rely on a solid state hybrid quantum system in one way or another. On the other hand most physical systems in nature are inherently non-linear, and used in classical examples ranging from lasers to single photon detectors. In this thesis I try to combine these two principles, something that has not been done yet in a solid state hybrid quantum system.

Starting from a system that is in the linear regime, and in many ways behaves like a two coupled harmonic oscillator system, I present two experiments, where we leave this linear regime and study the occurring non-linearity of the spin system.

In a first experiment I study amplitude bistability, one of the first non-linear effects discovered in quantum optics, where the system undergoes a phase transition between the linear and the non-linear regime. This first implementation of amplitude bistability in such a system allows to study completely new properties of the phase transition and directly observe the temporal evolution of it on an unprecedented time-scale of several tens of thousands of seconds, and allows to extract properties like the critical exponent of the transition.

In a second experiment I show another archetypal non-linear effect, that has not been shown so far in a solid state hybrid system. Superradiance is a collective non-linear effect where multiple emitters coupled to a cavity mode behave qualitatively different than a single emitter, with a collective decay many orders of magnitude faster than a single spin.

Negatively charged nitrogen vacancy centers in diamond act as as the (non-linear) spin system, coupled to either superconducting transmission line resonators or 3 dimensional lumped element resonators. The successful implementations give rise to rather immediate implications in the development of superradiant masers, quantum batteries, microwave switches and single microwave photon detectors.

Zusammenfassung

Hybride Quantensysteme werden ohne Zweifel, aufgrund ihrer Flexibilität und Potential für die Kontrolle und Manipulation von (komplexen) Quantensystemen, einen entscheidenden Einfluss auf die Entwicklung von Quantentechnologien im kommenden Jahrhundert haben. Diese Systeme in das Regime von Festkörperphysik zu bringen ist nur der nächste logische Schritt um sie besser skalierbar und interessant für größer skalierte Anwendungen zu machen. Viele Experimente haben bereits eine erfolgreiche Implementierung gezeigt und eine Reihe von Anwendungen heutzutage verwenden ein Festkörper Hybrides Quantensystem auf die eine oder andere Weise. Andererseits sind fast alle physikalischen Systeme in der Natur nicht-linear, und nicht-lineare Systeme werden erfolgreich in klassischen Beispielen wie dem Laser oder Einzelphotonen Detektoren benutzt. In dieser Arbeit versuche ich diese beiden Prinzipien zu verknüpfen, etwas was bis jetzt noch nicht in einem Festkörper Hybriden Quantensystem gelungen ist.

Ausgehend von einem linearen System, dass sich in vielen Punkten wie zwei gekoppelte harmonische Oszillatoren verhält, präsentiere ich zwei Experimente, bei denen dieses harmonische Regime verlassen wird und die nicht-linearen Eigenschaften der Spins sichtbar werden.

In einem ersten Experiment zeige ich Amplituden Bistabilität, einer der ersten nicht-linearen Effekte der in der Quantenoptik entdeckt wurde, bei dem das System einen Phasenübergang zwischen einem linearen und nicht-linearem Regime aufweist. Diese erste erfolgreiche Implementierung in einem Festkörper Hybriden System gibt uns die Möglichkeit neue Eigenschaften des Phasenüberganges zu studieren und direkt das zeitliche Verhalten zu beobachten, auf einer Zeitskala von beispiellosen zehntausenden von Sekunden. Das gibt die Möglichkeit Eigenschaften wie den kritischen Exponenten des auftretenden Phasenüberganges zu bestimmen.

In einem zweiten Experiment untersuche ich einen anderen archetypischen nicht-linearen Effekt, der bis jetzt noch nicht in einem Festkörper System gezeigt werden konnte. Superradianz ist ein kollektiver nicht-linear Effekt, bei dem viele Emitter sich qualitativ unterschiedlich zu einem einzelnem Emitter verhalten, mit einem kollektiven Zerfall viele Größenordnungen größer als ein einzelner Spin.

Um die Experimente zu realisieren verwenden wir ein Hybrides System mit negativ geladenen Stickstofffehlstellen in Diamant, als das (nicht-lineare) Spin System, dass entweder an einen supraleitende zweidimensionale oder dreidimensionalen Resonator gekoppelt wird. Die erfolgreiche Implementierung wird sehr schnell und sofortigen Einfluss auf die Entwicklung von superradianten Masern, Quantenbatterien, Mikrowellen Switches oder Mikrowellen Einzelphotonendetektoren haben.

Contents

1 Introduction and Outline **1**

2 Cavity Quantum Electrodynamics **3**

2.1 Cavities - Photons in a Box . . . 3

2.1.1 Quantization of a Single-mode Field . . . 4

2.1.2 Fock States . . . 6

2.1.3 Coherent States . . . 6

2.2 Interaction of Light with Matter - From Jaynes-Cummings to Maxwell Bloch Equations . . . 7

2.2.1 Interaction of a Single Spin with Quantized Light . . . 7

2.2.2 The Jaynes-Cummings Model . . . 8

2.2.3 From One to Many – Tavis Cummings Hamiltonian . . . 10

2.2.4 Dicke Model . . . 12

2.2.5 The Driven Tavis-Cummings . . . 14

2.2.6 Maxwell-Bloch Equations . . . 15

2.3 Holstein-Primakoff Approximation - Two Coupled Harmonic Oscillators 17

3 Experimental Setup **19**

3.1 Cavities . . . 19

3.1.1 The Quantized LC-Oscillator . . . 20

3.1.2 Transmission Line Resonators . . . 21

3.1.3 3D Lumped Element Resonators . . . 24

3.1.4 Cavity Input-Output theory . . . 30

3.2 Spin System . . . 32

3.2.1 The Nitrogen-Vacancy Center . . . 33

3.2.2 The Optical Transition and Thermal Polarization . . . 37

3.3 The Experimental Setup . . . 41

3.3.1 Homo-dyne Measurement and IQ-modulation . . . 44

3.3.2 Numerical Modeling . . . 45

4 Experiments 49
4.1 Amplitude Bistability – Operating between the Linear and Non-linear Regime . . . 49
  4.1.1 The Strong Coupling Regime of Cavity QED . . . 50
  4.1.2 Steady-state Bistability . . . 52
  4.1.3 Temporal Behavior of the Phase Transition . . . 61
  4.1.4 Outlook and Discussion . . . 66
4.2 Superradiance – Collective Non-linear Behavior . . . 68
  4.2.1 Superradiance – An Interference Effect . . . 69
  4.2.2 Operating in the “Fast” Cavity Limit of Cavity QED . . . 73
  4.2.3 Experimental Implementation . . . 75
  4.2.4 Thermal Occupation . . . 77
  4.2.5 Optical Measurements . . . 77
  4.2.6 Nonlinear Scaling and Enhanced Decay . . . 78
  4.2.7 Outlook and Discussion . . . 86

5 Outlook and Conclusion 89
5.1 Optimal Control of a Hybrid System . . . 89
5.2 Loop Gap Resonators for Stronger Coupling . . . 92
5.3 Conclusion . . . 94

List of Figures 99

References 109

Curriculum Vitae 121

1 Introduction and Outline

Since its beginnings in the early 20th century, a big part of quantum theory has been related to the study of light-matter interactions, starting with Einsteins insight that light consists of photons [1]. Other important milestones like Dirac using quantum mechanics for the first time to compute the coefficient of spontaneous emission of an atom [2], or the quantization of Maxwells equation by Feynman in the 1940s [3] are only a few of many more examples.

Trying to control and make use of this interaction led to the field of cavity quantum electrodynamics [4] where the quantized field of a cavity gives stronger coupling and more control over the coupled emitter. This led to numerous implementations [5–7] and even a Nobel price in 2012 [8, 9].

After successful demonstration of coherent exchange of energy (and information) between a two-level system and the photon field, these principles were successfully applied in quantum information physics, and up to this day many (if not all) realizations for quantum information physics are using cavities to help the readout, initialization or interaction control. This ranges from trapped ions, superconducting qubits and quantum dots to spin impurities in solids or optomechanical systems [10–16]. But not only for quantum computing, simulation or communication these types of systems play an important role, also for single photon detection or generation [17–19] or high sensitivity sensors [20–23], hybrid cavity – qubit systems are often used for the manipulation of electromagnetic fields.

Many of these applications use single or few qubits coupled to the cavity mode (or the cavity is “only” used as a readout or manipulation device), however, using large ensembles of qubits coupled to cavities are allowing and will allow new quantum technological applications, like multimode quantum memories [24–28], to be realized. In these hybridized systems high cooperativity and strong coupling has been successfully demonstrated with different species of spin systems [29–35].

Even though these types of systems have proven to be extremely successful and will most certainly lead to a breakthrough in the coming century, many of these implementations work in the linear regime of cavity QED [4, 36]. Here the hybrid system very much behaves like two coupled harmonic oscillators, a system we understand very well, but does not make use of one of the defining properties of the coupled qubit system. A two-level-system is by definition natures most an-harmonic system, and even though using a big ensemble of emitters disguises that, so is an ensemble of them.

In the presented thesis I will go one step further and present work that goes beyond the linear regime of cavity QED and explores its non-linear regime, a necessary step towards better understanding the physics of hybrid systems, and a roadmap for quantum technological applications.

Outline

I will start with a theoretical chapter explaining the theory behind light-matter interaction and the nature of quantized electromagnetic fields. The second (short) chapter is then dedicated to the description of the experimental setup, using either superconducting resonators or 3D resonators coupled to a solid state spin system – nitrogen-vacancy centers in diamond. Further, I will show the measurement as well as the numerical software setup necessary to employ and model the results. Finally, the last chapter shows two successful implementations of non-linear effects in our hybrid system, both experiments leaving the linear regime of cavity QED and exploring new and exciting physics.

2 Cavity Quantum Electrodynamics

The interaction of light and matter is beautifully described by Maxwell's equations discovered in the late 19th century. They ingeniously combine both the electric and magnetic fields to form the electromagnetic field. Quantizing these fields leads to quantum electrodynamics, one of the most powerful and precise physical theories and rewarded by a Nobel price for Feynman, Schwinger and Tomonaga in the 1940 [37–39]. This again led to the development of cavity quantum electrodynamics, which describes the interaction of this quantized field in a cavity with matter; be it atoms, spins or even mechanical oscillators.

In this chapter I will introduce the basic building blocks of cavity quantum electrodynamics (cQED) and how combining them allows to develop Hybrid Quantum Systems (HQS)

Parts of this chapter are based on [40–44]

2.1 Cavities - Photons in a Box

Starting from Maxwell's equations I will introduce the basic principles of quantization of the electromagnetic field in free space, with properties like Fock and Coherent states emerging from that, and how introducing boundary conditions leads to the quantized field inside a cavity.

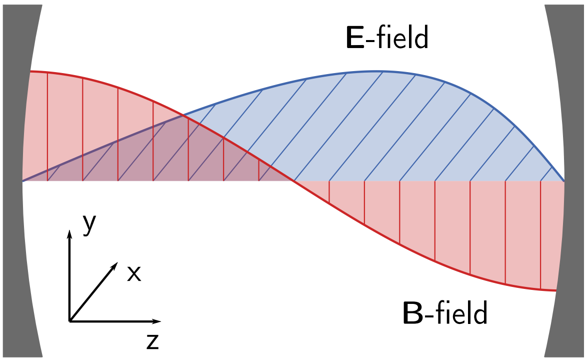

Figure 2.1: Representation of the quantized field inside two perfectly conducting walls. The boundary conditions force the electric field to be zero at 0 and L, whereas the strength of the magnetic field has to be maximum there. The electric field and magnetic field are perpendicular to each other and $\pi/2$ out of phase.

2.1.1 Quantization of a Single-mode Field

The starting point for the quantization of the electromagnetic field are Maxwell's equations in vacuum, given by

$$\begin{aligned} \nabla \cdot \mathbf{B} &= 0, \\ \nabla \cdot \mathbf{E} &= 0, \\ \nabla \times \mathbf{B} &= \mu_0 \varepsilon_0 \frac{\partial \mathbf{E}}{\partial t}, \\ \nabla \times \mathbf{E} &= -\frac{\partial \mathbf{B}}{\partial t}. \end{aligned} \tag{2.1}$$

For a one dimensional cavity along the z-axis (see Fig. 2.1) with perfectly conducting walls, one gets a solution to these equations using mode expansion [41] as (we arbitrarily choose the electric field to be polarized in the x-direction)

$$\begin{aligned} E_x(z,t) &= \sum_j \sqrt{\frac{2\omega_j^2}{V\varepsilon_0}}\, q_j(t) \sin(k_j z), \\ B_y(z,t) &= \sum_j \left(\frac{\mu_0 \epsilon_0}{k_j}\right) \sqrt{\frac{2\omega_j^2}{V\varepsilon_0}}\, \dot{q}_j(t) \cos(k_j z). \end{aligned} \tag{2.2}$$

Here μ_0 and ϵ_0 are the vacuum permeability and permittivity, V the mode volume of the cavity, ω_j the angular frequency of mode j and k_j the wave vector of mode j.

These equations full-fill the boundary conditions of a vanishing E-field at $z = 0, L$ and obey Maxwell's equations. Note that the E and B-field are $\pi/2$ out of phase, and perpendicular to each other. In the following we only consider single mode fields ($j = 1$).

The classical field energy Hamiltonian, is given by,

$$H = \frac{1}{2}\int dV \left[\varepsilon_0 \mathbf{E}^2(\mathbf{r},t) + \frac{1}{\mu_0}\mathbf{B}^2(\mathbf{r},t)\right] = \frac{1}{2}\left(\dot{q}^2 + \omega^2 q^2\right). \tag{2.3}$$

It is obvious that this single-mode field is formally equivalent to a simple harmonic oscillator (with unit mass), where q and $\dot{q}$ are the canonical variables, equivalent to position and momentum for a harmonic oscillator. It is instructive to replace q and $\dot{q}$ by the corresponding operators $\hat{q}$ and $\hat{p}$, that satisfy the commutation relation

$$[\hat{q}, \hat{p}] = i\hbar. \tag{2.4}$$

In order to recover the familiar form of the quantum harmonic oscillator, we introduce the so-called creation and annihilation operators

$$\hat{a}^\dagger = \frac{\omega\hat{q} - i\hat{p}}{\sqrt{2\hbar\omega}} \quad \text{and} \quad \hat{a} = \frac{\omega\hat{q} + i\hat{p}}{\sqrt{2\hbar\omega}}, \tag{2.5}$$

such that they obey the commutation relation $[\hat{a}, \hat{a}^\dagger] = 1$.

We can now express the quantum harmonic oscillator with the quantized fields

$$\begin{aligned} \hat{H} &= \hbar\omega\left(\hat{a}^\dagger\hat{a} + \frac{1}{2}\right), \\ \hat{E}_x(z,t) &= \mathcal{E}_0(\hat{a} + \hat{a}^\dagger)\sin(kz), \\ \hat{B}_y(z,t) &= -i\mathcal{B}_0(\hat{a} - \hat{a}^\dagger)\cos(kz), \end{aligned} \tag{2.6}$$

where $\mathcal{E}_0 = \sqrt{\hbar\omega/\varepsilon_0 V}$ and $\mathcal{B}_0 = \sqrt{\mu_0\hbar\omega/V}$ can be identified as the electric and magnetic field per photon. Note that the time dependence of the field operators is put into the creation and annihilation operators as $\hat{a}(t) = \hat{a}(0)e^{-i\omega t}$ – this is known as the Heisenberg picture.

2.1.2 Fock States

For a single mode field with angular frequency ω we now can consider the eigenstates and eigenvalues of the Hamiltonian in Eq. (2.6). If we define $|n\rangle$ to be the eigenstate of the Hamiltonian with eigenenergy E_n and apply the annihilation operator from the left, we obtain

$$\hat{H}\hat{a}\,|n\rangle = (E_n - \hbar\omega)\hat{a}\,|n\rangle\,. \tag{2.7}$$

This means that the state

$$\hat{a}\,|n\rangle = \sqrt{n}\,|n-1\rangle\,, \tag{2.8}$$

is also an eigenstate of the Hamiltonian with the reduced energy $E_n - \hbar\omega$ (the normalization constant $\sqrt{n}$ is necessary for the normalization of $\langle n-1|n-1\rangle$). If we repeat this procedure n times we move down the energy ladder and end up in the vacuum state $|0\rangle$

$$\hat{H}\hat{a}\,|0\rangle = (E_0 - \hbar\omega)\hat{a}\,|0\rangle\,. \tag{2.9}$$

Since E_0 is defined to be the ground state of the system we must conclude that $\hat{a}\,|0\rangle = 0$, and $E_0 = \hbar\omega/2$ is the zero point energy of the vacuum. $E_n = (n + 1/2)\,\hbar\omega$ is therefore the eigenenergy of the eigenstate $|n\rangle$.

The same line of thought applies to the creation operator giving

$$\hat{a}^\dagger\,|n\rangle = \sqrt{n+1}\,|n+1\rangle\,. \tag{2.10}$$

In general we can conclude that the state $|n\rangle$ is constructed by applying the creation operator n-times on the vacuum state:

$$|n\rangle = \frac{(\hat{a}^\dagger)^n}{\sqrt{n!}}\,|0\rangle\,. \tag{2.11}$$

The operator $\hat{n} = \hat{a}^\dagger\hat{a}$ acts as a number operator counting the number of photons in an energy mode.

2.1.3 Coherent States

The field states that most resemble classical states are the so called coherent states introduced by Roy Glauber 1963 [45] (and awarded with a Nobel price 2005). If a mode contains a large number of photons N, the fluctuations around the average value are small and in the order of $1/\sqrt{N}$ making them behave like classical states.

The coherent states are defined as the eigenstates of the annihilation operator

$$\hat{a}\,|\alpha\rangle = \alpha\,|\alpha\rangle\,, \tag{2.12}$$

which gives, expanded in the Fock basis

$$|\alpha\rangle = e^{-|\alpha|^2/2}\sum_{n=0}^{\infty}\frac{\alpha^n}{\sqrt{n!}}\,|n\rangle\,. \tag{2.13}$$

Calculating the average value of the electric field for a coherent state now gives

$$\langle\alpha(t)|\hat{E}_x(z)|\alpha(t)\rangle = \mathcal{E}_0\sin(kz)|\alpha(0)|\cos(\phi_0-\omega t), \tag{2.14}$$

i.e. a classical field with phase ϕ_0 and amplitude $\alpha(0)$.

The probability to find a coherent state in a Fock state with exactly n-photons is given by

$$|\,\langle\alpha|n\rangle\,|^2 = e^{-\bar{n}}\frac{\bar{n}^n}{n!} \tag{2.15}$$

which is a Poisson distribution with average number of photons $\bar{n} = |\alpha|^2$. The standard deviation $\Delta n = \sqrt{\bar{n}}$ shows that for a large number of photons the width of the distribution $\Delta n/\bar{n}$ goes to zero, i.e. for $\alpha \gg 1$ the coherent state approaches the classical limit.

To create a coherent state we can use the formal solution of Eq. (2.12), which allows to generate a coherent state using a unitary displacement operator acting on the vacuum state as

$$|\alpha\rangle = e^{\alpha\hat{a}^\dagger-\alpha^*\hat{a}}|0\rangle = D(\alpha)|0\rangle. \tag{2.16}$$

2.2 Interaction of Light with Matter - From Jaynes-Cummings to Maxwell Bloch Equations

After quantizing the field inside a resonator, the next step to understand the physics of cavity QED systems. We will look at atoms (or two-level-systems in general) and the interaction of them with the quantized field.

2.2.1 Interaction of a Single Spin with Quantized Light

The interaction of a two-level-system (TLS) with an electromagnetic field, can be described by the interaction energy of a magnetic field with the dipole-moment of a single electron spin (note that for the electric field interacting with an electric dipole-moment the derivation is analogous), given by

$$E_{\text{pot}} = -\boldsymbol{\mu} \cdot \mathbf{B} = -\frac{g_e \mu_B}{\hbar} \mathbf{S} \cdot \mathbf{B}. \tag{2.17}$$

Here g_e is the gyro-magnetic ratio of an electron, and μ_B the Bohr magneton. Without loss of generality we can put the quantization axis of the spin in the $\hat{\sigma}_x$ direction, which then gives $\hat{\boldsymbol{S}} = \hbar\hat{\sigma}_x/2$, and together with the quantized magnetic field (see Eq. (2.6)), we end up with an interaction Hamiltonian

$$\hat{H}_{\text{int}} = -\frac{g_e \mu_B}{\hbar} \hat{\mathbf{S}} \cdot \hat{\mathbf{B}} = i \frac{\mathcal{B}_0 \cos(kz) g_e \mu_B}{2} \hat{\sigma}_x (\hat{a} - \hat{a}^\dagger) = i\hbar g \hat{\sigma}_x (\hat{a}^\dagger - \hat{a}), \tag{2.18}$$

with $g = -\frac{\mathcal{B}_0 \cos(kz) \mu_B g_e}{2\hbar}$ as the interaction strength of a single photon with a single electron magnetic moment. $\hat{\sigma}_x$ can be written in terms of the spin raising and lowering operator (which creates or destroys an excitation of a TLS, cf. [46]) as $\hat{\sigma}_x = \hat{\sigma}_+ + \hat{\sigma}_-$. This gives an interaction Hamiltonian of the form

$$\hat{H}_{\text{int}} = i\hbar g (\hat{\sigma}_+ + \hat{\sigma}_-)(\hat{a}^\dagger - \hat{a}) = i\hbar g (\hat{\sigma}_+ \hat{a}^\dagger + \hat{\sigma}_- \hat{a}^\dagger - \hat{\sigma}_+ \hat{a} - \hat{\sigma}_- \hat{a}). \tag{2.19}$$

Both $\hat{\sigma}_+ \hat{a}^\dagger$ and $\hat{\sigma}_- \hat{a}$ are two photon processes where two quanta of energy are either destroyed or created, which makes them non energy conserving. For a coupling strength $g \ll \omega$ (ω being the Larmor frequency of the TLS) we therefore make the well-known rotating wave approximation (RWA) and neglect both of these terms [40].

This finally leaves us with an interaction Hamiltonian of the form

$$\hat{H}_{\text{int}} = i\hbar g (\hat{\sigma}_- \hat{a}^\dagger - \hat{\sigma}_+ \hat{a}), \tag{2.20}$$

where the first term creates a photon in the cavity mode and destroys an excitation in the spin system, while the second term does the reverse - destroying a photon in the cavity mode and putting an excitation into the TLS.

2.2.2 The Jaynes-Cummings Model

After deriving both the quantization of the cavity field and the interaction of that cavity field with a single TLS, it is rather straightforward to write down the full Hamiltonian that describes the combined cavity spin system. Taking into account both the energy of the cavity mode and the TLS plus the interaction of the two, the Hamiltonian to

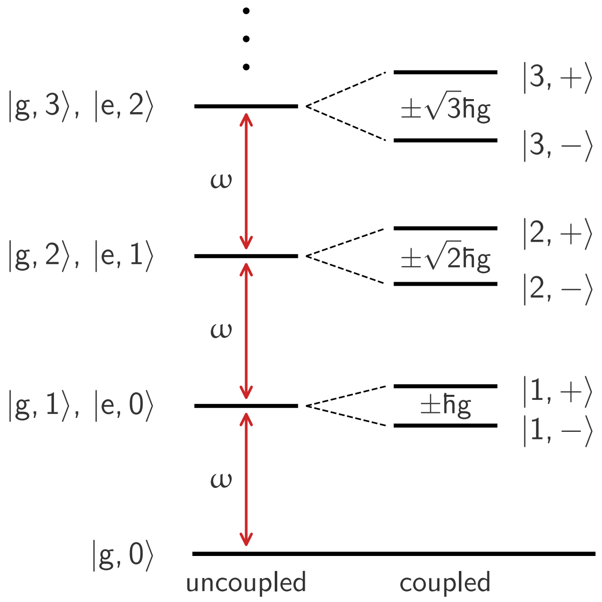
$|g,3\rangle,\ |e,2\rangle$
$|g,2\rangle,\ |e,1\rangle$
$|g,1\rangle,\ |e,0\rangle$
$|g,0\rangle$
ω
ω
ω
$\pm\sqrt{3}\hbar g$
$\pm\sqrt{2}\hbar g$
$\pm\hbar g$
$|3,+\rangle$
$|3,-\rangle$
$|2,+\rangle$
$|2,-\rangle$
$|1,+\rangle$
$|1,-\rangle$
uncoupled
coupled

Figure 2.2: Jaynes-Cummings ladder for cavity and spin in resonance ($\omega_c = \omega_s = \omega$). In the n-excitation regime the coupled eigenstates are shifted by a factor $\propto \pm\sqrt{n}$ compared to the uncoupled eigenstates.

describe the interaction of a single TLS with the quantized mode of the cavity is

$$\hat{H} = \hat{H}_{\text{cav}} + \hat{H}_{\text{spins}} + \hat{H}_{\text{int}} = \hbar\omega_c \hat{a}^\dagger \hat{a} + \frac{\hbar\omega_s\hat{\sigma}_z}{2} + i\hbar g(\hat{\sigma}_-\hat{a}^\dagger - \hat{\sigma}_+\hat{a}). \tag{2.21}$$

Here we removed the vacuum energy of the cavity mode since it is just an energy offset and makes computations more tedious. Contrary to most problems in modern physics, this Hamiltonian can be diagonalized and the exact eigenenergies calculated [47].

For a given number of photons in the cavity mode the exact eigenenergies are (see Fig. 2.2)

$$E_n^{\pm} = \hbar\omega_c\left(n + \frac{1}{2}\right) \pm \frac{1}{2}\hbar\sqrt{(\omega_s - \omega_c)^2 + 4g^2 n} \tag{2.22}$$

with the eigenstates

$$\begin{aligned} |n,-\rangle &= \cos(\theta/2)\,|g,n+1\rangle - \sin(\theta/2)\,|e,n\rangle \\ |n,+\rangle &= \sin(\theta/2)\,|g,n+1\rangle + \cos(\theta/2)\,|e,n\rangle\,, \end{aligned} \tag{2.23}$$

where the angle θ is defined by

$$\theta = \tan^{-1}\left(\frac{2g\sqrt{n+1}}{\omega_s - \omega_c}\right). \tag{2.24}$$

Here $|g\rangle$ and $|e\rangle$ denote the spin to be in the ground or excited state, respectively. The effective coupling strength of the TLS to the cavity, thus, scales with $g \propto \sqrt{n+1}$, that is with the square root of the number of photons in the mode.

Now, for zero detuning we have the simple eigenstates

$$\begin{aligned} |-\rangle_n &= \frac{1}{\sqrt{2}}\left(|g, n+1\rangle - |e, n\rangle\right) \\ |+\rangle_n &= \frac{1}{\sqrt{2}}\left(|g, n+1\rangle + |e, n\rangle\right), \end{aligned} \tag{2.25}$$

with the system being in a superposition of having the excitation in the spin system ($|e\rangle$) or in the cavity mode ($|n+1\rangle$).

Energy put into the system will oscillate between excitations in the cavity and excitations in the spins with an oscillation frequency defined by the coupling strength and the number of photons in the cavity mode.

2.2.3 From One to Many – Tavis Cummings Hamiltonian

Only very few experiments deal with single emitters in a single mode cavity [48] since the interaction of a single atom or spin with a cavity is usually very small. Especially for spins, up to date no experiment exists that is able to couple a single spin strong enough, such that the coupling surpasses the losses in the system (also known as strong coupling regime). To overcome this limitations, one can couple many spins to the cavity simultaneously and increase the collective coupling strength by that. This leads to the generalized Jaynes-Cummings Hamiltonian for N-spins, better known as Tavis-Cummings Hamiltonian [49]. The derivation of the Tavis Cummings Hamiltonian for many spins is equivalent to the Jaynes-Cummings Hamiltonian and gives a very similar looking Hamiltonian

$$\hat{H} = \hbar\omega_c \hat{a}^\dagger \hat{a} + \sum_{i=1}^{N} \frac{\hbar\omega_s^i \hat{\sigma}_z^i}{2} + i\hbar \sum_{i=1}^{N} g_i(\hat{\sigma}_-^i \hat{a}^\dagger - \hat{\sigma}_+^i \hat{a}). \tag{2.26}$$

Note that we have taken into account not only the fact that each spin not necessarily has to have the same frequency (known as in-homogeneous broadening), but also that each spin can have a different coupling strength, thus, the summation over ω_s^i and g_i.

Without in-homogeneous broadening and with homogeneous coupling strength ($\omega_s^i = \omega_s,\ g_i = g$), we can introduce the collective spin operators,

$$\begin{aligned} \hat{S}_z &= \sum_{i=1}^{N} \hat{\sigma}_z^i \\ \hat{S}_\pm &= \sum_{i=1}^{N} \hat{\sigma}_\pm^i, \end{aligned} \tag{2.27}$$

and the Hamiltonian simplifies to

$$\hat{H} = \hbar\omega_c \hat{a}^\dagger \hat{a} + \frac{\hbar N \omega_s \hat{S}_z}{2} + i\hbar g(\hat{S}_- \hat{a}^\dagger - \hat{S}_+ \hat{a}). \tag{2.28}$$

This Hamiltonian is almost equivalent to the Hamiltonian presented in Eq. (2.21) and shows very similar solutions including eigenenergies and eigenstates. For the single excitation regime we get

$$|\pm\rangle = \frac{1}{\sqrt{2}} \left(|1, G\rangle \pm |0, D_1\rangle \right), \tag{2.29}$$

as the symmetric and anti-symmetric eigenmode. These are not all eigenmodes for the single excitation regime (as the Hilbert space is larger for multiple spins) but the only ones that contain photons in the cavity and are therefore visible when probing the cavity. All the other eigenstates (commonly referred to as dark states) are not visible in transmission spectroscopy.

$|D_1\rangle$ is the so called Dicke-state (see Section 2.2.4) (in the single excitation regime also called W-state) and is represented as a superposition of the excitation(s) shared between all spins. Each spin contributes to the coupling to the cavity mode (because of the sum in the definition of the ladder operators) such that

$$g_{\text{coll}} = \sqrt{g_1^2 + g_2^2 + g_3^2 + \dots} = g\sqrt{N}, \tag{2.30}$$

for homogeneous coupling strengths. This allows to enter the strong coupling regime by coupling to many spins instead of one spin.

For the higher excitation regime the eigenstates quickly become complicated, but in principle analytic solutions exist [49]. The eigenenergies for the single excitation regime now not only scale with the square root of the number of photons in the cavity mode (as derived for the Jaynes-Cummings model), but also with the number of spins coupled. For a single excitation the eigenenergies for the symmetric and anti-symmetric eigenmodes are then given by, and scale with the number of spins coupled to the cavity mode as

$$E_{\pm} = \hbar\omega_c \pm \sqrt{N}\hbar g. \tag{2.31}$$

2.2.4 Dicke Model

Mentioned in the previous section, let us now consider the Dicke model as introduced in the early 1950s [50, 51]. It describes how atoms in a dense ensemble get excited and de-excited and which states they can occupy. This is an important concept in cavity QED since the interaction of the spins with light is always mediated by the cavity, which exhibits two operators that can excited or de-excite a spin, allowing only the simplest transition in the spin system. Note that the notion of Dicke states, however, does not require a cavity mode but was originally conceived with a cloud of atoms in vacuum, but given the nature of the interaction term, is a necessary concept to understand cQED systems.

According to the rules of quantum mechanics the individual spins of an N-spin system arrange such that the total spin ranges from $\mathbf{S} = N/2, N/2-1, \dots 1$. The magnetic quantum number then spans from $m_s = -|\mathbf{S}|, \dots, |\mathbf{S}|$.

The ground state is given by $|D_0\rangle = |G\rangle = |\downarrow\downarrow \dots \downarrow\rangle$. This is the first Dicke state and is by construction a symmetric state (that is the state does not change under spin exchange).

By continuously applying the ladder operators for spins (which is the only operator present in the interaction term in the Hamiltonian of Eq. (2.21)) on the ground state

$$\hat{S}_{\pm}\left|S, m_S\right\rangle = \hbar\sqrt{S(S+1) - m_S\left(m_S \pm 1\right)}\left|S, m_S \pm 1\right\rangle, \tag{2.32}$$

we can reach all the symmetric spin states, which are then known as Dicke states:

$$\left|D_i\right\rangle = \sqrt{\frac{i!(N-i)!}{N!}}\left(\hat{S}_+\right)^i\left|D_0\right\rangle. \tag{2.33}$$

The transition matrix element from the first to the second Dicke state can be computed as

$$M_{D_1 \leftarrow D_0} = \left\langle D_1\right|\hat{S}_+\left|D_0\right\rangle = \sqrt{N}, \tag{2.34}$$

which shows the $\sqrt{N}$ enhancement due to the coupling of N spins.

In an ideal spin system and starting with a spin ensemble in the ground state, this would be the only possible states the spins can occupy. In a real system however, also non fully symmetric states are reached. Due to in-homogeneous broadening each spin can have a small detuning from the central spin frequency.

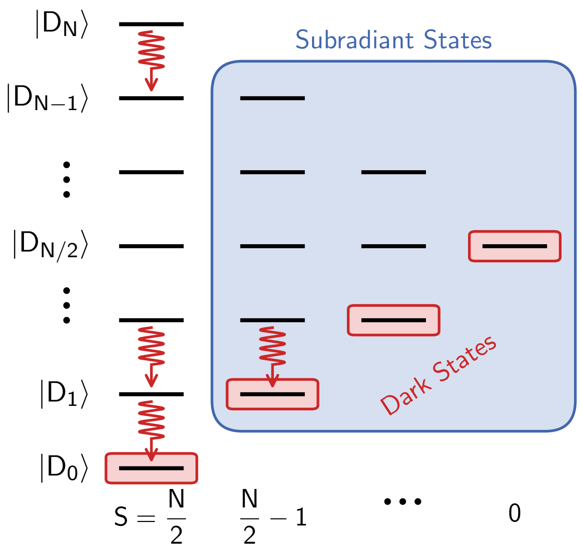

Figure 2.3: Dicke ladder for an ensemble of N spins. The leftmost states are the Dicke states, generated by applying the spin raising operator with N excitations and a total spin of $S = N/2$. Transitions between two Dicke states exist, as indicated by the red arrows. Dephasing leads to an evolution into the subradiant states that still decay within their subspace but with a smaller coupling to the electromagnetic field (blue shaded area) and a smaller total spin quantum number. Going up and down in this manifold is again possible with spin raising and lowering operators. The dark states are the ground states of their respective manifolds and cannot decay (red shaded area) since their transition matrix element to the real ground state is zero.

Without loss of generality we look at the case of three spins to exemplify this. The first Dicke state for three spins is given by:

$$|D_1\rangle = \frac{1}{\sqrt{3}}\left(|\uparrow\downarrow\downarrow\rangle + |\downarrow\uparrow\downarrow\rangle + |\downarrow\downarrow\uparrow\rangle\right) \tag{2.35}$$

For a Hamiltonian including the detunings for each spin ($\delta\omega_i$), like:

$$\hat{H} = \frac{\hbar}{2}\sum_{i=1}^{3}(\omega_s - \delta\omega_i)\sigma_z^i, \tag{2.36}$$

this state evolves, depending on the individual detunings, as

$$|D_1\rangle = \frac{1}{\sqrt{3}} \left(e^{i(\delta\omega_2+\delta\omega_3)t} |{\uparrow\downarrow\downarrow}\rangle + e^{i(\delta\omega_1+\delta\omega_3)t} |{\downarrow\uparrow\downarrow}\rangle + e^{i(\delta\omega_1+\delta\omega_2)t} |{\downarrow\downarrow\uparrow}\rangle \right) . \tag{2.37}$$

We can already see, that depending on the time passed, the fully symmetric subspace is left and other states are reached. These states also couple to the cavity mode, but the transition matrix elements for these states become smaller, which means that their coupling to the electromagnetic field is weaker. These states are often called sub-radiant states (one should be aware that everyone uses different notions here) since their smaller coupling to the electromagnetic field has the effect of a smaller decay rate (cf. Section 4.2).

The rightmost state in the Dicke ladder – which would be the fully anti-symmetric state – does not couple to the electromagnetic field anymore at all. These states for which the matrix transition element is zero and cannot decay (except for spontaneous emission processes), are often referred to as dark states.

2.2.5 The Driven Tavis-Cummings

Having derived the unitary system, where Fock states in the cavity mode drive the transitions in the spin system and prepare the system in eigenstates of the hybrid system, let us now consider the more experimentally relevant case of driving the cavity with an external coherent drive (e.g. a laser).

The interaction Hamiltonian of a quantized magnetic field with a classical drive field (with a drive frequency ω_p and possibly time-dependent drive amplitude A_0) can be written as (with the time dependence of the operators explicitly, see Section 2.1.1)

$$\hat{H}_{\mathrm{dr}} = -i\hbar\mathcal{B}_0(\hat{a}e^{-i\omega t} - \hat{a}^\dagger e^{i\omega t})A_0 \cos(kz)\cos(\omega_p t) . \tag{2.38}$$

This is equivalent to

$$\hat{H}_{\mathrm{dr}} = -i\hbar\frac{\mathcal{B}_0}{2}(\hat{a}e^{-i\omega t} - \hat{a}^\dagger e^{i\omega t})\cos(kz)A_0 \left(e^{i\omega_p t} + e^{-i\omega_p t}\right) . \tag{2.39}$$

Again making a rotating wave approximation and neglecting terms of the form $\pm(\omega+\omega_p)$ we end up with a drive term (note that the operators are again time-dependent here)

$$H_{\mathrm{dr}} = i\hbar\eta(\hat{a}^\dagger e^{-i\omega_p t} - \hat{a}e^{i\omega_p t}). \tag{2.40}$$

η is here the drive amplitude of the external field (which can be time-dependent, and is averaged over the whole half period of the cosine).

Putting all parts together we get the full driven Tavis-Cummings Hamiltonian as

$$\hat{H} = \hbar\omega_c \hat{a}^\dagger \hat{a} + \sum_{i=1}^{N} \frac{\hbar\omega_s^i \hat{\sigma}_z^i}{2} + i\hbar \sum_{i=1}^{N} g^i (\hat{\sigma}_-^i \hat{a}^\dagger - \hat{\sigma}_+^i \hat{a}) + i\hbar\eta(\hat{a}^\dagger e^{-i\omega_p t} - \hat{a} e^{i\omega_p t}) \tag{2.41}$$

We can get rid of the time-dependence of the driving term, by performing the unitary transformation

$$\begin{aligned} \hat{U} &= e^{-i\omega_p t\left(\hat{a}^\dagger \hat{a} + \sum_{i=1}^{N} \frac{\hbar\omega_s^i \hat{\sigma}_z^i}{2}\right)}, \\ \hat{H}_\mathrm{u} &= \hat{U}^\dagger \hat{H} \hat{U} - i\hbar \hat{U} \frac{\partial \hat{U}}{\partial t}. \end{aligned} \tag{2.42}$$

This leaves us with a final Hamiltonian of the form

$$\hat{H}_\mathrm{u} = \hbar\Delta_c \hat{a}^\dagger \hat{a} + \sum_{i=1}^{N} \frac{\hbar\Delta_s^i \sigma_z^i}{2} + i\hbar \sum_{i=1}^{N} g^i (\hat{\sigma}_-^i \hat{a}^\dagger - \hat{\sigma}_+^i \hat{a}) + i\hbar\eta(\hat{a}^\dagger - \hat{a}), \tag{2.43}$$

describing N spins coupled to a single mode cavity with the detunings of the form $\Delta_j^{(i)} = \omega_j^{(i)} - \omega_p$. This Hamiltonian includes both the in-homogeneous broadening of the spins as well as a possible in-homogeneous coupling strength of the individual spins.

2.2.6 Maxwell-Bloch Equations

The Hamiltonian in Eq. (2.43) describes (except for the drive term) a closed and unitary system, which means that dissipation or loss of coherence cannot happen. Since, however, the presented experiments are carried out in a solid state spin system, which offers a noisy environment loss of coherence and dissipation of energy are unavoidable companions. Moreover, losing energy through the cavity is not only unavoidable but also necessary since it allows to measure the transmission through the cavity which is our observable in all the following experiments.

Describing a system that is coupled to its environment can be done in the framework of open quantum systems and the Lindblad Master equation. In the following we will only show the shortest treatment of open quantum systems, for more in depth explanations the reader is referred to the excellent explanation in [52]

The standard way to derive the equation of motions for an open quantum system is to include the interacting environment into the system Hamiltonian. The whole temporal evolution of the density matrix is then governed by the van Neumann equation

$$\frac{d\hat{\rho}_\mathrm{tot}(t)}{dt} = -\frac{i}{\hbar}\left[\hat{H}_\mathrm{tot}, \hat{\rho}_\mathrm{tot}(t)\right] \tag{2.44}$$

with the full system Hamiltonian $\hat{H}_{\text{tot}}$

$$\hat{H}_{\text{tot}} = \hat{H}_{\text{sys}} + \hat{H}_{\text{env}} + \hat{H}_{\text{int}}. \tag{2.45}$$

The environment Hamiltonian $\hat{H}_{\text{env}}$ and an interaction Hamiltonian $\hat{H}_{\text{int}}$ describe the interaction of the system with the environment. By tracing over the environmental degree of freedom in Eq. (2.44) we then obtain an equation of motion for the original system density matrix:

$$\frac{d\hat{\rho}_{\text{tot}}(t)}{dt} = -\frac{i}{\hbar}[\hat{H}(t), \hat{\rho}(t)] + \frac{1}{2}\sum_n \left[2\hat{L}_n\hat{\rho}(t)\hat{L}_n^+ - \hat{\rho}(t)\hat{L}_n^+\hat{L}_n - \hat{L}_n^+\hat{L}_n\hat{\rho}(t)\right]. \tag{2.46}$$

Here $\hat{L}_n = \sqrt{\gamma_n}\hat{A}_n$ are the collapse operators, with $\hat{A}_n$ the operator with which the system couples to the environment with a rate γ_n. The second part is also known as the Liouvillian ($\hat{\mathcal{L}}$) of the system.

For the case of our cavity QED system there are three operators that couple the system to its environment (we assume zero temperature since temperature effects can be neglected).

1. Loss of energy through photon loss ($\hat{a}$) with the cavity dissipation rate κ
2. Decoherence of the spins with a rate $\gamma_\perp$ (commonly also referred to as T_2 time as $\gamma_\perp = 1/T_2$) through the operator $\hat{\sigma}_z$
3. Decay of spin excitations, either through phonon mediated processes [53], or spontaneous emission, with a rate $\gamma_\parallel = 1/T_1$ and the operator $\hat{\sigma}_-$

Putting that all together leaves us with a Liouvillian of the form (for simplicity we omit the operator sign from now on)

$$\begin{aligned} \mathcal{L} &= \kappa\left(2a\rho a^\dagger - a^\dagger a\rho - \rho a^\dagger a\right) \\ &+ \frac{\gamma_\parallel}{2}\sum_j^N \left(2\sigma_-^j\rho\sigma_+^j - \sigma_+^j\sigma_-^j\rho - \rho\sigma_+^j\sigma_-^j\right) + \frac{\gamma_\perp}{4}\sum_j^N\left(2\sigma_z^j\rho\sigma_z^j - 2\rho\right). \end{aligned} \tag{2.47}$$

Using $\langle o\rangle = \text{Tr}(\rho o)$ and Eq. (2.46) we end up with a set of coupled differential equations describing the dynamics of our system:

$$\begin{aligned}
\dot{\langle a \rangle} &= -\kappa \langle a \rangle - i\Delta_c \langle a \rangle + \sum_j g_j \langle \sigma_-^j \rangle + \eta \\
\dot{\langle \sigma_-^j \rangle} &= -i\Delta_s^j \langle \sigma_-^j \rangle + g_j \langle a\sigma_z^j \rangle - \left(\gamma_\perp + \frac{\gamma_\parallel}{2}\right) \langle \sigma_-^j \rangle \\
\dot{\langle \sigma_z^j \rangle} &= -\gamma_\parallel \left(1 + \langle \sigma_z^j \rangle\right) - 2g_j \left(\langle \sigma_-^j a^\dagger \rangle + \langle \sigma_+^j a \rangle\right) .
\end{aligned} \tag{2.48}$$

This is not a closed set of differential equations since it contains also all the expectation values like $\langle a\sigma_z^j \rangle$ for which one needs to write down new differential equations. However, when dealing with large number of emitters (as it is the case in the following experiments) and a relatively small coupling between the cavity mode and the spins, quantum effects that are encoded in this correlators are negligibly small and one can make the ansatz $\langle a\sigma_z^j \rangle = \langle a \rangle \langle \sigma_z^j \rangle$. This leads to the famous Maxwell-Bloch equations for N-emitters coupled to a single mode cavity:

$$\begin{aligned}
\dot{\langle a \rangle} &= -\kappa \langle a \rangle - i\Delta_c \langle a \rangle + \sum_j g_j \langle \sigma_-^j \rangle + \eta \\
\dot{\langle \sigma_-^j \rangle} &= -i\Delta_s^j \langle \sigma_-^j \rangle + g_j \langle a \rangle \langle \sigma_z^j \rangle - \left(\gamma_\perp + \frac{\gamma_\parallel}{2}\right) \langle \sigma_-^j \rangle \\
\dot{\langle \sigma_z^j \rangle} &= -\gamma_\parallel \left(1 + \langle \sigma_z^j \rangle\right) - 2g_j \left(\langle \sigma_-^j \rangle \langle a^\dagger \rangle + \langle \sigma_+^j \rangle \langle a \rangle\right) .
\end{aligned} \tag{2.49}$$

2.3 Holstein-Primakoff Approximation - Two Coupled Harmonic Oscillators

Our experimental realization of a cavity QED system features a large number of spins coupled to the cavity mode. In the small excitation limit (much less excitations in the cavity mode than spins coupled to the cavity) this allows to treat the entire spin system as an effective harmonic oscillator. This approximation is based on the Holstein-Primakoff transformation.

For the spin operators it is possible to write down the transformation

$$\begin{aligned}
S_+ &= b^\dagger \sqrt{2S - b^\dagger b} \\
S_- &= \sqrt{2S - b^\dagger b}\, b \\
S_z &= \left(b^\dagger b - S\right) ,
\end{aligned} \tag{2.50}$$

with $b, b^\dagger$ being standard bosonic creation and annihilation operators obeying the bosonic commutation rules. This transformation is exact and the operators still obey the spin-commutation relations.

If the number of spins coupled becomes large and the mode occupation number $b^\dagger b$ is small compared to the number of spins (i.e. $S \gg b^\dagger b$) we can Taylor expand these operators and perform the Holstein-Primakoff approximation

$$\begin{aligned} S_+ &\approx b^\dagger \sqrt{2S} \approx \sqrt{N} b^\dagger \\ S_- &\approx \sqrt{2S} b \approx \sqrt{N} b. \end{aligned} \tag{2.51}$$

The collective Tavis-Cummings Hamiltonian from Eq. (2.28) becomes (note that the same derivation can also be done for the Tavis-Cummings Hamiltonian without collective spin operators)

$$H = \hbar\omega_c a^\dagger a + \hbar\omega_s (b^\dagger b - S) + \hbar g \sqrt{N} \left(a b^\dagger + a^\dagger b \right), \tag{2.52}$$

that is two coupled harmonic oscillators with a coupling strength of $g\sqrt{N}$.

This makes sense intuitively since the defining properties of an *harmonic* oscillator is the fact, that the eigenenergies are harmonic (i.e. equidistant). This is also true for a very large spin ensemble, since one excitation is shared between many spins and the total energy to put another excitation into the system hardly changes ($S_z = -N/2$ is valid for all times in this approximation). The spin system accepts another photon and the probability to excite an already excited spin is negligible. This approximation is valid as long as the number of spins is much larger than the number of excitations in the system $N \gg a^\dagger a$. In this limit the system behaves as two coupled harmonic oscillators and shows the same eigenmodes and eigenenergies.

This approximation breaks down as soon as the number of photons in the cavity mode becomes comparable to $\sqrt{N}$ and the aforementioned neglection of higher order terms is not applicable any more. The scope of this thesis is to show experiments where these approximations break down, and the non-linear regime (i.e. beyond the Holstein-Primakoff approximation) of cavity QED is reached.

3 Experimental Setup

Having derived the theoretical background of cavity QED, let me now turn the attention to the experimental setup. In this chapter I will first introduce the types of cavities that we are using to implement our experiments, namely transmission line resonators that gives us strong coupling to the spin system and are easy to handle, and newly developed 3D Lumped element resonators which allow us to perform experiments not possible with 2D resonators, due to their specific geometry.

After that I will introduce the spin system used, in order to build a Hybrid Quantum System. The theoretical background introduced in the last chapter does not specify which kind of two-level-system to use for a cavity QED experiment, as it describes not only spins in solids coupled to resonators, but also cold atoms coupled to optical cavities or even optomechanical setups. In our case we are using nitrogen-vacancy centers in diamond, a versatile and very robust spin system in a very beneficial host material.

Finally I will show the experimental setup used to perform our measurements at low temperatures (30 mK) to obtain thermal polarization of our spin system and a home-build microwave setup to perform fast and coherent manipulation of our spin system.

3.1 Cavities

This chapter is based on the following research paper and uses parts of it:

- **“Collective strong coupling with homogeneous Rabi frequencies using a 3D lumped element microwave resonator”**
  Andreas Angerer, Thomas Astner, Daniel Wirtitsch, Hitoshi Sumiya, Shinobu Onoda, Junichi Isoya, Stefan Putz, and Johannes Majer
  Applied Physics Letters 109, 089901 (2016)

The first building block for a cavity QED system is arguably the cavity, that provides the quantized mode of radiation to couple the spins to.

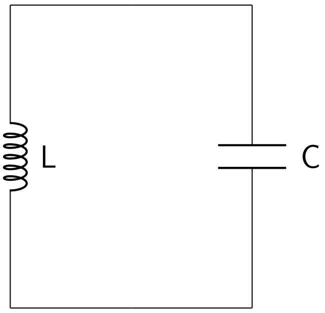

Figure 3.1: Simple schematic of a LC-circuit with inductance and capacitance in series. By putting charges into the circuit, they will oscillate with an eigenfrequency of $\omega = (LC)^{-1/2}$ between the capacitance and the inductance.

In general there are two × two different ways to build a resonator in the microwave regime. Resonators can be either distributed element resonators, where the resonating parts are distributed in coaxial lines, waveguides and/or stubs, or lumped element resonators, where the resonating parts are discrete capacitors and inductors. The second distinctive feature of resonators is that they can have either a 2 or a 3 dimensional design (this distinction is a bit superficial since also one-dimensional resonators exist, but the statement still makes sense in this context). In this section I will introduce Transmission Line Resonators (used in one of the presented experiments) as a specimen of a Distributed Element Resonator in a 2 dimensional design, and newly developed 3D lumped element resonators which give us features not accessible with a planar geometry and used for the last experiment presented in Section 4.

3.1.1 The Quantized LC-Oscillator

As stated before every cavity (or resonator) in the microwave regime can be understood in terms of a resonating LC-circuit, no matter if they are distributed or discrete. That means that somewhere there has to be a capacitance and an inductance, and charges will oscillate with a given eigenfrequency. To understand, however, why an LC circuit resonates, and why it can be understood as a harmonic oscillator, let us consider a simple circuit as displayed in Fig. 3.1.

If we start by putting a charge on one of the capacitor plates, the whole energy of the circuit is initially stored in the capacitor. This energy is

$$E_C = \frac{1}{2}\frac{q_0^2}{C} \tag{3.1}$$

The capacitor will try to discharge itself via the inductance, which will result in a current through the inductance. At some point in time the capacitor will be discharged and the whole energy is stored in the inductor as

$$E_I = \frac{1}{2} L i_0^2 = \frac{1}{2} \frac{\Phi_0^2}{L}, \tag{3.2}$$

with the magnetic flux defined as $\Phi_0 = i/L$. Since there is no dissipation in the system these two energies have to be equivalent, and we get for the total electromagnetic energy for an arbitrary time t

$$E = \frac{1}{2} \frac{\Phi(t)^2}{L} + \frac{1}{2} \frac{q(t)^2}{C}. \tag{3.3}$$

Φ and q can now be understood as two conjugated variables with commutation relation $[\Phi, q] = -i\hbar$. This allows to define the creation and annihilation operator by

$$q = \sqrt{\frac{\hbar C}{2L}} \left(a + a^\dagger\right) \text{ and } \Phi = -i \sqrt{\frac{\hbar L}{2C}} \left(a - a^\dagger\right), \tag{3.4}$$

and we finally recover the quantized harmonic oscillator exactly as derived in Section 2.1.1, as

$$H = \hbar\omega \left(a^\dagger a + \frac{1}{2}\right), \tag{3.5}$$

with an oscillation frequency $\omega = 1/\sqrt{LC}$.

3.1.2 Transmission Line Resonators

A transmission line resonator is arguably the most straightforward way to build a 2 dimensional resonator. It consists of a transmission line of length L, that is intercepted at two points. These interception points act as mirrors for the electromagnetic radiation and a standing wave between the two mirrors is created (cf. Fig. 3.2). As shown in Section 2.1.1, this can be interpreted as a quantized magnetic field as

$$\hat{B}_x(z,t) = \mathcal{B}_0(\hat{a} + \hat{a}^\dagger) \sin(kz), \tag{3.6}$$

with $k = n\pi/L$. It is important to mention here that the electric and magnetic field change role here (i.e. the magnetic field is maximum in the middle and zero at the interceptions), since contrary to before the boundary conditions are not perfect electrical conductors anymore, but the interceptions are capacitors. This means that the magnetic field has to vanish, and the electric field has to become maximum at the boundaries. However, the derivation is completely analogous.

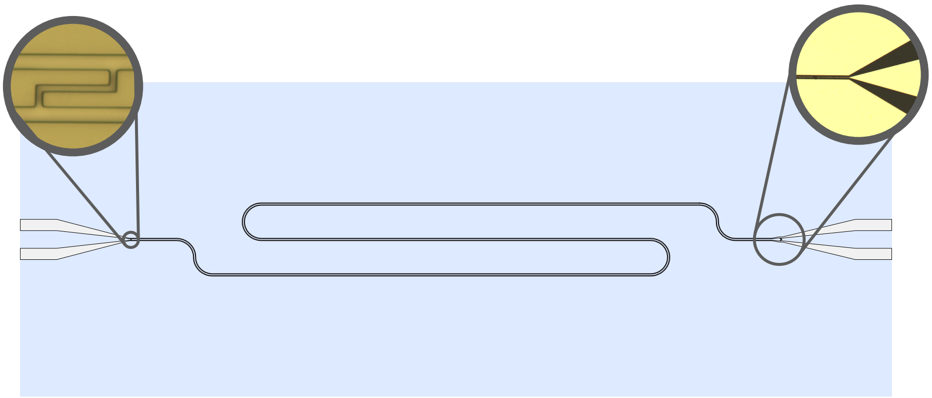

Figure 3.2: Rendering of a transmission line resonator as it is used in the experiment. On the left side the capacitance is shown that couples the resonator to its environment. The quantized mode is generated between two capacitors on both sides of the resonator. The center conductor is meandering in order to increase the overlap of the oscillating magnetic field with the sample which is placed on top of the resonator. On the right side the taper down to the central line is shown with the bonding to a copper PCB on the far right.

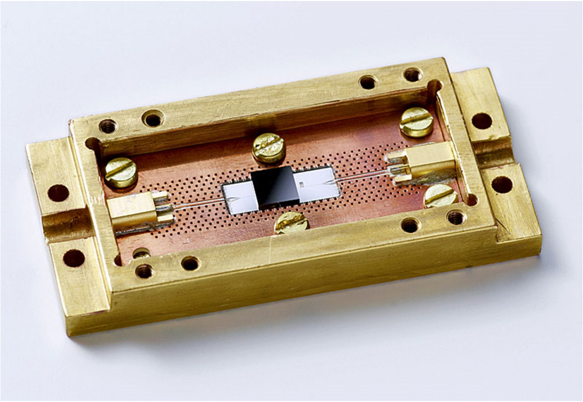

Figure 3.3: Picture of a transmission line resonator loaded with a diamond sample. The superconducting resonator is bonded in a printed circuit board, which is put in a closed copper box to avoid unwanted box resonances. The diamond sample is the black object in the center of the device.

The fundamental resonance given by $n = 1$ (also known as $\lambda/2$ since half a wavelength of radiation is contained in the cavity) is the one used in the experiments and all modes $n > 1$ are higher harmonics, disregarded in the following. The quality factor of a cavity is given by $Q = \omega/\kappa$ (ω is the frequency of the fundamental resonance and κ the rate

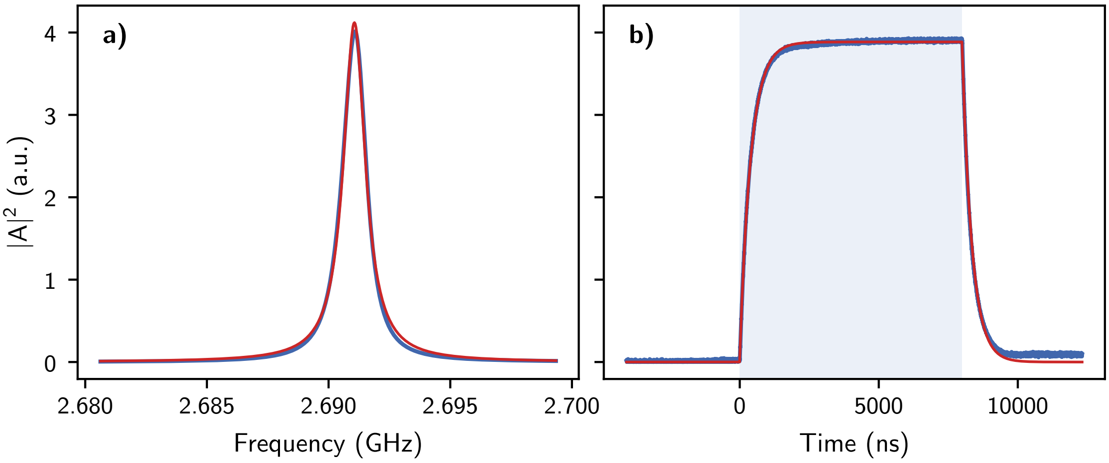

Figure 3.4: a) Measured cavity response spectrum fitted with a Lorentzian line-shape according to Eq. (3.16). From the transmission spectrum we can easily deduce the line-width (i.e. κ) and the resonance frequency of of the cavity. **b)** Time response of the cavity under a 8 µs pulse on resonance. The time for which the MW drive is turned on is depicted as blue shaded area. The cavity field builds up and decays with a characteristic time constant given by the cavity line-width κ. The time response is equivalent to a Fourier transform of the spectrum as shown in a) and vice versa.

with which the cavity loses energy) and describes how under-damped or over-damped a resonator is, or in other words how much energy is stored compared to the energy dissipated per cycle (see Section 3.1.4 for more details). The quality factor for a 2 dimensional design is mainly limited by radiation loss due to its design and losses in the interface between conductor and substrate.

The resonators used to carry out the following experiments are made out of a 200 nm thick Niobium layer sputtered on a 300 µm thick Sapphire substrate. Niobium as a type II superconductor has the advantage of becoming superconducting at low temperatures ($T_c \approx 8.5\,\mathrm{K}$ for a thin layer) which removes ohmic losses in the conducting material. The thin layer of Niobium is further structured by optical lithography which allows to create structures with micron resolution, good enough for creating the transmission line intercepted at two points.

Measuring the transmission through such a cavity is shown in Fig. 3.4a) and gives a Lorentzian line-shape (see Section 3.1.4), from which we can deduce the resonance frequency and the cavity line-width and, thus, the quality factor. We can also measure the time response of the cavity shown in Fig. 3.4b), by driving it with a microwave pulse of short duration and measuring the temporal response instead of the frequency response. The field inside the cavity builds up and decays again with a time constant

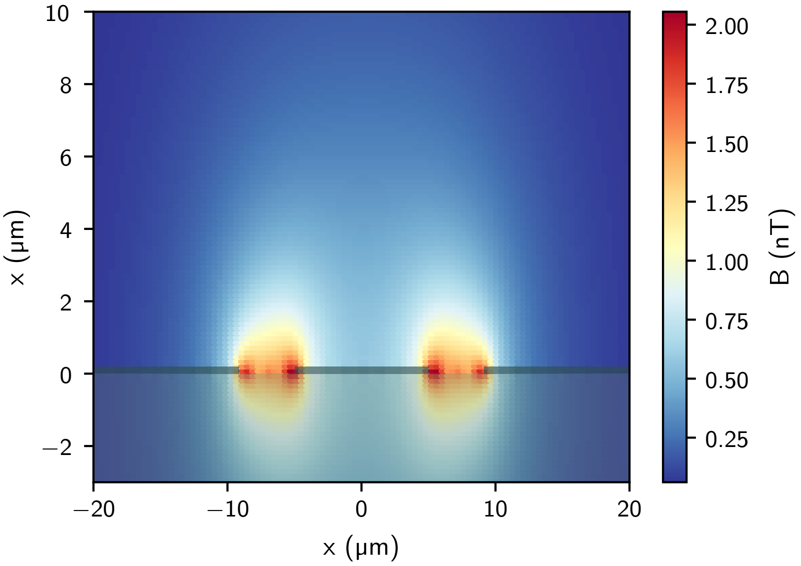

Figure 3.5: Transverse magnetic field distribution of a 2D resonator design showing the magnetic field generated by a single photon in the cavity mode. The black shaded area shows the niobium thin film with the center conductor in the middle and the ground plane on the outside. As can be seen from the plot, the magnetic field distribution is such that the magnetic field is almost exclusively focused to a region close to the surface of the thin film. Only spins close to the surface experience a strong effect of the magnetic field, whereas spins further away are almost not influenced. This produces a huge gradient in the individual coupling strengths and makes it impossible to coherently manipulate all spins at the same time.

$\tau = 1/2\kappa$.

3.1.3 3D Lumped Element Resonators

One big issue with 2D resonator designs is its dependence of the coupling strength on the transversal, longitudinal position and even worse its dependence on the distance from the resonator [54] as it is demonstrated in Fig. 3.5. This leads to in-homogeneous coupling strength depending on where the spin is located relative to the resonator. However, the strong confinement of the (electro)magnetic field allows to couple very strongly to the cavity mode which is advantageous since it allows to enter the strong coupling regime without coupling to too many emitters at the same time.

While two dimensional lumped element resonators have been successfully demon-

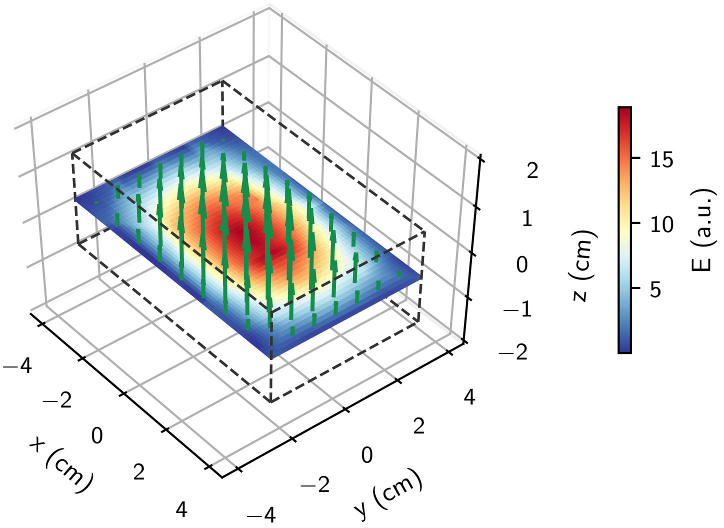

Figure 3.6: Simulated field distribution inside a 3D box resonator. As visible from the arrows, the electric field (note that this analogous for the magnetic field) is uniformly pointing in one direction. Also the magnitude is very homogeneous in a wide area in the center of the cavity. However, the plot also shows that the resonator becomes bulky (see the black dashed lines denoting the dimensions of the cavity) for a resonance frequency of 3 GHz, and, due to its huge mode volume, also the coupling to a single spin is very small.

strated and show even higher coupling strengths [55] to a single spin compared to transmission line resonators, their disadvantage lies in the fact that the spatial dependence on the coupling strength is even worse than for transmission line resonators. As such they are not useful to solve the aforementioned problem of in-homogeneous coupling strength.

One way to solve the in-homogeneous coupling strength to the spin ensemble is to use box-cavities [56] as a specimen of distributed element resonators in three dimensions, since the magnetic field distribution in such a box cavity is very homogeneous as shown in Fig. 3.6. It also provides very high quality factors (especially when using superconducting material) since its closed structure reduces radiation losses to a minimum [57, 58]. Nevertheless, this types of cavities are not suitable for our experiments because of two reasons: First, the required frequency of $\approx 3\,\mathrm{GHz}$ makes very large and bulky cavities necessary, as the resonance frequency is defined by the dimensions of the box

[59]:

$$\omega_{mnl} = ck_{mnl} = c\sqrt{\left(\frac{m\pi}{a}\right)^2 + \left(\frac{n\pi}{b}\right)^2 + \left(\frac{l\pi}{d}\right)^2}. \tag{3.7}$$

Here, a, b, d are length, width and depth of the box. For a frequency of 3 GHz this requires dimensions of the box of $\approx$ 10 cm, which makes it hard to handle in an experimental setup. The second issue with these type of resonators is also linked to their size. The coupling of the spin system to a single photon (i.e. the vacuum Rabi splitting) is inversely proportional to the square root of the mode volume (see Section 2.1.1). Since the mode volume in these types of resonators is huge, the coupling to a single spin becomes very small < 1 mHz. In order to enter the strong coupling regime (for our specific spin system and cavities approximately 10 MHz), one needs to couple to a huge amount of spins $> 10^{18}$, something hard (or close to impossible) to synthesize for material scientists.

In order to solve the problem of small and in-homogeneous coupling strength, while keeping the size of the resonator relatively small, we came up with a combination of these two designs, namely a 3 dimensional lumped element resonator. In a lumped resonator, instead of distributed capacitance and inductance, the resonating parts are discrete parts, where the resonance frequency is not defined by the dimensions of the enclosing box, but by the value of this discrete components by

$$\omega_c = \frac{1}{\sqrt{LC}}. \tag{3.8}$$

As a consequence of that, there are also no higher harmonics since these discrete components can be much smaller than the wavelength of the radiation [1].

Our implementation consists of metallic structures enclosed in a surrounding conducting box, as shown in Fig. 3.7a). These two bow-tie shaped structures create two capacitors with the enclosing box, which together with the inductance (which is unavoidably there because the current has to close the circuit) creates a resonating LC-circuit (see Fig. 3.8). This resonator actually exhibits two resonances (see Fig. 3.10), one where the current goes the short path through the metallic structures, and one where the current closes the LC-circuit through the walls (see Fig. 3.7b)). Since the inductance is larger for the second mode, its frequency is lower than the frequency of the mode closing the circuit the short path. The nice feature of the higher frequency mode is the fact that since the current goes as indicated in Fig. 3.7b), according to

---

[1] That's also how radios work: The wavelength of the radiation is much larger than a real device, and the resonating part are discrete capacitors and inductors allowing to build them much smaller

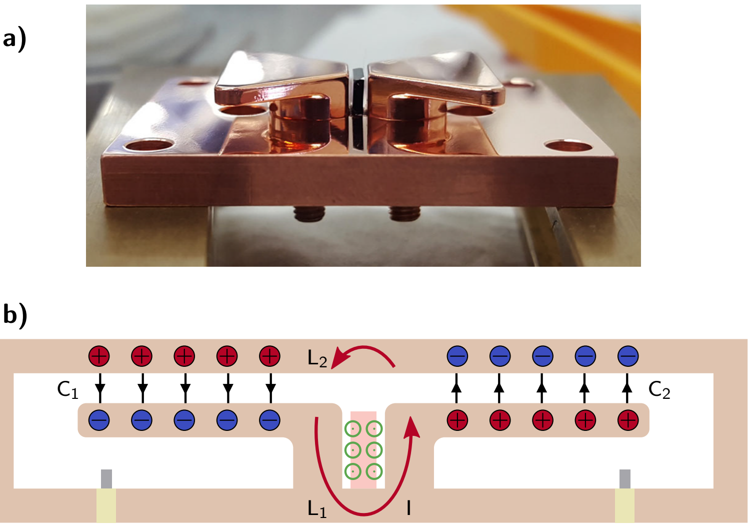

Figure 3.7: a) Photo of the 3D lumped element resonator design. Shown is a polished copper cavity with the top lid and the side walls removed for illustrative purposes. The diamond is placed in between the two metallic “bow-ties” as can be seen in the photo. **b)** A cut through the cavity, perpendicular to the direction of the mode. The two capacitors together with the inductance create an oscillating magnetic field focused in between the two metallic structures that is pointing out of the plane. The field is coupled into the mode with two pins, one for coupling into the mode, and the other one for measuring the transmission (Source [60]).

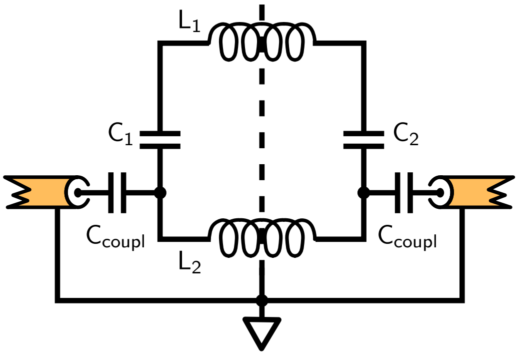

Figure 3.8: Equivalent circuit for the lumped element resonator. 50 Ω terminated input and output ports are coupled via two coupling capacitors (C_{coupl}) to the LC circuit. Inductors and capacitors are labeled according to Fig. 3.7b) (Source [60]).

Lenz’s law this current creates a magnetic field that is focused to in-between these two metallic structures and cancels everywhere else (contrary to that the other mode focuses the magnetic field outside and cancels it in between the two structures).

This feature enhances the coupling strength in a way that allows to enter the strong coupling regime (see Section 4.1.1) with a moderate amount of spins coupled (10^{16}) and a similar collective coupling strength we achieve with transmission line or 2D lumped

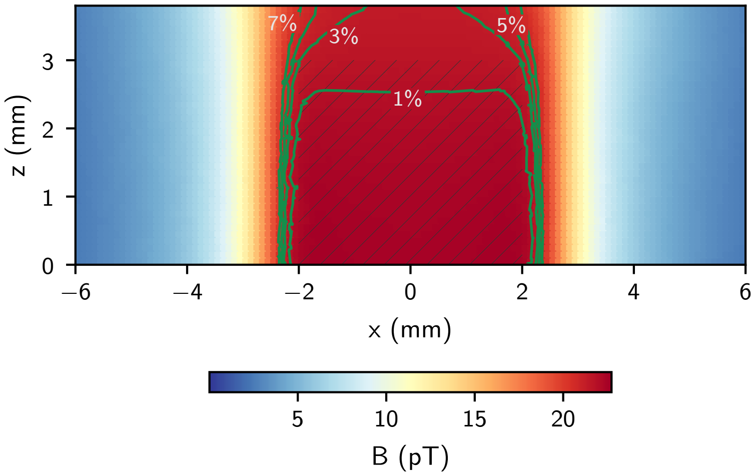

Figure 3.9: Field distribution within the 3D lumped element resonator generated by a single photon in the cavity mode. The hatched area is where the diamond is located, and the contourlines show the RMS deviation of the coupling strength for 1%, 3%, 5% and 7%.

element resonators.

Due to its special geometry the magnetic field distribution is on top of that very homogeneous, with a root-mean-square (RMS) deviation of maximally 7% (see Fig. 3.9). That allows to homogeneously couple to all spins that are placed within a 4 mm × 3 mm × 0.5 mm volume.

Since the resonance frequency is defined by the inductance and the capacitance of the circuit, the design allows us to intrinsically change the resonance frequency by changing the distance of the two bow-ties which changes the inductance.

We can calculate the total capacitance as two capacitors in series configuration as

$$C_{tot}^{-1} = C_1^{-1} + C_2^{-1} = 2C^{-1} = \frac{2}{\epsilon_0}\frac{d}{A}, \tag{3.9}$$

with d the distance between the top lid and the bow-tie, and A the total area of the bow-tie that forms the capacitance, which for our typical parameters gives us a total capacitance of 2.9 pF. The inductance can be approximated by the inductance of a flat wire [61] with

$$L_{tot} = 2\times 10^{-10} l \left(\ln\left(\frac{l}{w+t}\right) + 0.5 + 0.2235\left(\frac{w+t}{l}\right)\right). \tag{3.10}$$

Here w is the width of the wire, which we can approximate by the width of our bow-tie structures, l the length of the path the current has to take, and t approximated as the

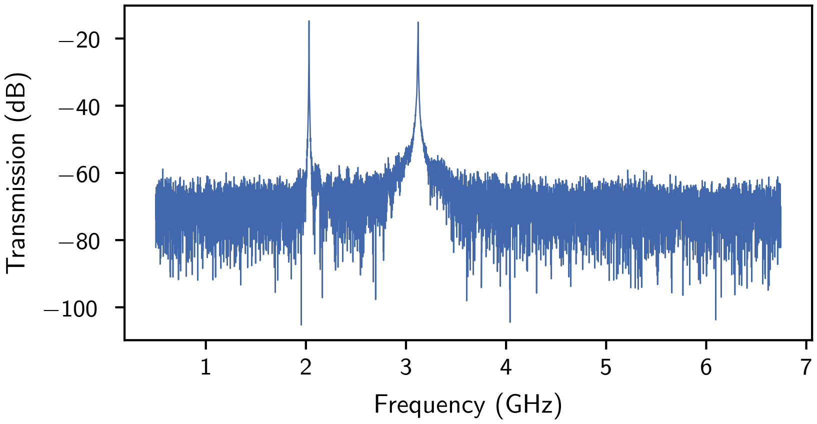

Figure 3.10: Transmission spectroscopy of the 3D lumped element resonator. Visible are two resonances with the lower one generally having slightly higher Q values (narrower line-width), but no magnetic field in the region of interest, and the higher one used in our experiments to couple the spins to. Apart from the two resonances no higher harmonics are present, with the box-modes at a much higher frequency.

skin depth of the oscillating current. This gives a total inductance of $\approx 0.95\,\mathrm{nH}$ which estimates a resonance frequency of

$$\omega_c = \frac{1}{\sqrt{LC}} = 2\pi \cdot 3.03\,\mathrm{GHz}. \tag{3.11}$$

Transmission spectroscopy reveals that the true fundamental frequency is at $\omega_c = 2\pi \cdot 3.121\,\mathrm{GHz}$ (see Fig. 3.10) which, considering the relatively crude approximation of the inductance, shows that the assumption of discrete circuit elements is valid.

From the transmission spectrum we also obtain the quality factor of $Q = 1637$ and the cavity line-width as $\kappa/2\pi = 1.91\,\mathrm{MHz}$. Finally, finite element studies show that the achieved single spin coupling strength is given by $\approx 70\,\mathrm{mHz}$ which is orders of magnitude larger than a simple 3D box cavity and good enough to enter the strong coupling regime.

The quality factor is mainly limited by ohmic losses in the conducting material, since the need for magnetic fields to tune the spin system limits us to copper as the conducting material, as the best conductor at low temperatures that does not become superconducting. Superconducting 3D lumped element resonators with much higher Q-values of $Q \approx 10^6$ are also easy to fabricate, but their superconducting enclosure makes it impossible to use magnetic fields to Zeeman tune the spin system (see Section 3.2.1), but is useful nonetheless for certain types of experiments.

3.1.4 Cavity Input-Output theory

To understand the presented transmission spectra shown in Section 3.1.2 and Section 3.1.3 let us now turn to a description of the cavity, using so called input-output theory [62]. We consider a simple two sided cavity as presented in Fig. 3.11 with input coupling rate κ_1 and output-coupling rate κ_2 and an internal line-width κ_{int}. These individual line-widths all describe a loss of energy, be it through the coupling to the environment (κ_1, κ_2) or internal losses (κ_{int}). The total line-width of the cavity is then $\kappa_{\text{tot}} = \kappa_1 + \kappa_2 + \kappa_{\text{int}}$.

Before deriving the equations of motions for the cavity system let us consider three different scenarios for the losses

1. $\kappa_{\text{int}} \gg \kappa_1, \kappa_2$; $\kappa_{\text{tot}} \approx \kappa_{\text{int}}$: This is known as under-coupled cavity, where the losses of a cavity are mainly given by the internal losses of the cavity (this is generally the “unwanted” case, even if there are scenarios where this is desired).
2. $\kappa_{\text{int}} \ll \kappa_1, \kappa_2$, $\kappa_{\text{tot}} \approx \kappa_1 + \kappa_2$: This is known as over-coupled scenario and can be used to maximize the number of photons in the cavity. Here the dissipation of energy is due to a strong coupling to the environment. Note that also the ratio of κ_1 to κ_2 can be changed to achieve different effects.
3. $\kappa_{\text{int}} = \kappa_1 + \kappa_2 = \kappa$, $\kappa_{\text{tot}} = 2\kappa$: The resonator is critically coupled (or impedance matched). In this limit the number of photons in the steady becomes maximum.

Analogous to the derivation of the Maxwell-Bloch equations in Section 2.2.6, we get a Langevin equation for the Hamiltonian as derived in Eq. (2.6) for the intra-cavity amplitude as [46, 63]

$$\dot{a} = -\frac{i}{\hbar}[H, a] - (\kappa_1 + \kappa_2 + \kappa_{int})\, a + \sqrt{2\kappa_1}\, a_{\text{in}} + \sqrt{2\kappa_2}\, b_{\text{in}}. \tag{3.12}$$

Here a_{in} and b_{in} are operators that describe an input on both sides of the cavity, and are coupled to the cavity with the external coupling rates κ_1, κ_2 (note that here the first Markov approximation is made, which explains the square roots, please cf. [63] for a derivation).

In a frame rotating with the drive frequency we get

$$\dot{a} = -\left(i\Delta_c + \kappa_{tot}\right) a + \sqrt{2\kappa_1}\, a_{\text{in}} + \sqrt{2\kappa_2}\, b_{\text{in}}, \tag{3.13}$$

with $\Delta_c = \omega_c - \omega_p$, ω_p the drive frequency and ω_c the resonance frequency of the cavity. If we now assume the input from the second mirror to be equal to zero (i.e. $b_{\text{in}} \equiv 0$) we get

$$\dot{a} = -\left(i\Delta_c + \kappa_{tot}\right) a + \sqrt{2\kappa_1}\, a_{\text{in}}, \tag{3.14}$$

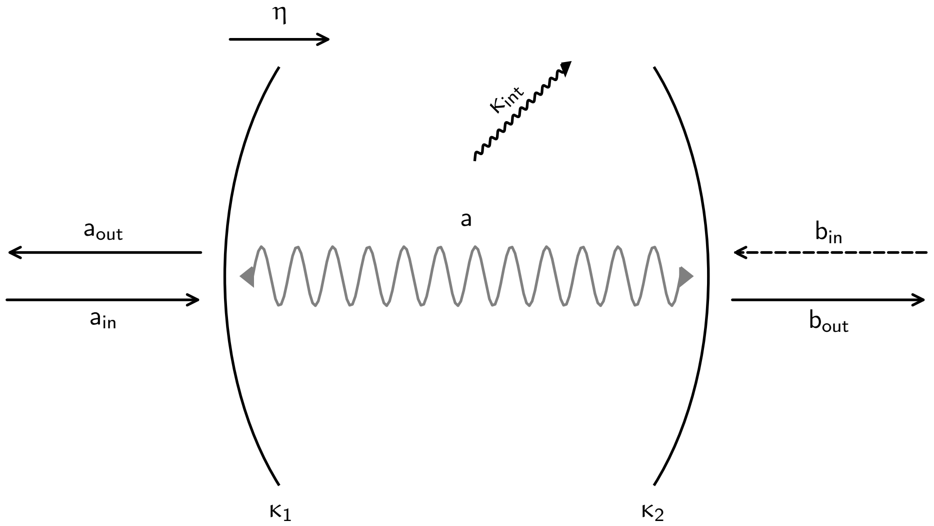

Figure 3.11: Schematic representation of a cavity with input and output fields and losses as described in the main text. Since we drive the cavity only from the left side we omit b_{in}.

which describes the evolution of a cavity that is driven from one side. The boundary conditions, relating each of the far field amplitudes on the outside of the cavity to the internal cavity field [46], are given by

$$\begin{aligned} a_{\text{in}} + a_{\text{out}} &= \sqrt{2\kappa_1}\,a \\ b_{\text{in}} + b_{\text{out}} &= \sqrt{2\kappa_2}\,a \quad \Rightarrow \quad b_{\text{out}} = \sqrt{2\kappa_2}\,a. \end{aligned} \tag{3.15}$$

For transmission spectroscopy we are only interested in the steady state of the system ($\dot{a} = 0$) which then for the transmission amplitude gives (as the ratio of the transmitted field amplitude to the input field amplitude)

$$T = \frac{b_{\text{out}}}{a_{\text{in}}} = \frac{2\sqrt{\kappa_1\kappa_2}}{i\Delta_c + \kappa_{\text{tot}}}, \tag{3.16}$$

which is a Lorentzian with amplitude $2\sqrt{\kappa_1\kappa_2}$ and line-width κ_{tot}. Often it is useful to consider the squared transmission amplitude (as it is what is usually measured) and the case of a symmetric cavity (i.e. $\kappa_1 = \kappa_2 = \frac{\kappa_{\text{ext}}}{2}$). This then further simplifies to

$$|T|^2 = \frac{\kappa_{\text{ext}}^2}{\Delta_c^2 + \kappa_{\text{tot}}^2}. \tag{3.17}$$

Depending if the resonator is over-, under- or critically coupled, the transmission either approaches $T \rightarrow 1, 0, 1/2$ (for the resonant case)

By comparing the equation of motion we derived for the input-output theory as in Eq. (3.14) to the equations of motions derived for the Maxwell-Bloch equations in Eq. (2.49), we can immediately make a connection between the input field a_{in} and the coherent drive amplitude η as

$$\eta = \sqrt{2\kappa_1}\, a_{\text{in}}. \tag{3.18}$$

If we set $P_{\text{in}} = \hbar\omega_p |a_{\text{in}}|^2$, (i.e. the input power is given by the energy of a single photon times the field amplitude squared), we get (we assume real values here)

$$|a|^2 \left|(i\Delta_c + \kappa_{\text{tot}})\right|^2 = \frac{2\kappa_1 P_{\text{in}}}{\hbar\omega_p}. \tag{3.19}$$

Since $|a|^2 = N$ is the number of photons (assuming real valued operators), we get the number of photons in the cavity in the steady state to be

$$N = \frac{2\kappa_1 P_{\text{in}}}{\hbar\omega_p \left(\Delta_c^2 + \kappa_{\text{tot}}^2\right)} \tag{3.20}$$

or for a symmetric cavity driven on resonance

$$N = \frac{\kappa_{\text{ext}} P_{\text{in}}}{\hbar\omega_p \kappa_{\text{tot}}^2}. \tag{3.21}$$

On resonance, the transmission in Eq. (3.17) can be used to further simplify this equation to

$$N = \frac{|T| P_{\text{in}}}{\hbar\omega_p \kappa_{\text{tot}}}, \tag{3.22}$$

an expression that relates the number of photons in the steady state to easily measurable quantities.

3.2 Spin System

An empty cavity is fundamentally something trivial, as the harmonic oscillator is arguably the most studied physical system in existence, due to the fact that most problems in physics can be approximated by it. To do interesting physics we need an an-harmonic system that couples to this harmonic oscillator. A two-level-system (or more specifically a spin) is the natural choice, since by definition it is, contrary to the harmonic oscillator, natures most an-harmonic system. Quite naturally this leads to new and interesting physics beyond the two coupled harmonic oscillators approximation.

In this section I will introduce our spin system of choice, namely the negatively charged nitrogen-vacancy center and its properties. I will also explain how a large ensemble of these spins can be used to build a Hybrid Quantum System at low temperatures and how to use the optical transition to read out the spin state separately without the detour via the cavity.

3.2.1 The Nitrogen-Vacancy Center

The nitrogen-vacancy center (NV-center) has attracted a lot of interest in the last couple of decades. Once a very promising candidate for quantum computing, nowadays the interest has shifted from quantum information physics, to quantum technologies, like sensing [64–68] or other quantum technologies such as masers [69].

Several properties of the NV center make it very suitable to use it to couple it to our resonators as building block to create a Hybrid Quantum system. The NV center is extremely stable (unless the diamond is burned, once an NV center is formed it will stay), due to its host material [70]. NV centers can be implanted using nitrogen enriched diamonds and neutron- [71] or even better electron irradiation [72] which is necessary to create dense ensembles (see Section 2.2.3) and even though it is a solid state system, a single NV center is (or can be) extremely coherent [73].

The NV center consists of a nitrogen atom replacing an carbon atom in a diamond lattice with an adjacent vacancy. This gives three dangling bonds from the carbon atoms and two electrons from the nitrogen. The two electrons from the nitrogen covalently bind with two electrons from the carbon which leaves one unpaired electron. All the presented work here is carried out with the negatively charged NV center where one additional electron from the lattice (probably from another nitrogen atom), together with the unpaired electron then forms a spin $S = 1$ system [74, 75].

Due to dipole-dipole interaction of the two electrons we obtain a zero-field splitting of $D = 2\pi \cdot 2.88\,\text{GHz}$ with the ground state being the $m_s = 0$ state (i.e. two spins in opposite direction is energetically favorable) and the $m_s = \pm 1$ state the excited states (note that it is more complicated as there are also non-axial terms, but the reader is referred to [76] for more information on the exact formalism of dipole-dipole interaction).

The ground state Hamiltonian of the NV center can be written down as

$$H_{\text{NV}} = \hbar D \left(S_z^2 - \frac{1}{3} S\left(S+1\right) \right) + \hbar E \left(S_x^2 + S_y^2\right)) + \hbar \mu_{\text{NV}} \mathbf{B}_{\text{ext}} \cdot \mathbf{S}, \tag{3.23}$$

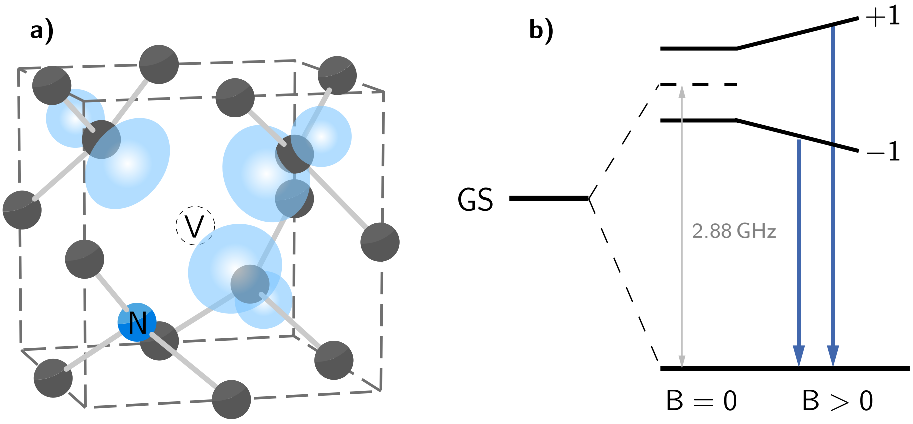

Figure 3.12: The structure of the NV center in the diamond lattice with its ground state term-scheme. **a)** The NV center consists of a nitrogen atom that replaces a carbon atom in the diamond lattice which then forms the NV center together with an adjacent vacancy. Plotted is the computed spin density, which shows that the electron of the NV center is mainly located close to the adjacent carbon atoms. **b)** The ground state level scheme of the NV center. The NV center exhibits a zero-field splitting (ZFS) of $\approx 2.88\,\text{GHz}$ at low temperatures. A magnetic field allows to tune the $m_s = \pm 1$ states in order to change the transition energy and bringing them in resonance with the cavity mode (Picture taken from [53]).

with a zero-field splitting of $D \approx 2\pi \cdot 2.88\,\text{GHz}$ [77], axial strain $E \approx 10\,\text{MHz}$ (this is very sample dependent and can range from 1 MHz to ≈10 MHz) the spin magnetic moment $\mu_{\text{NV}} = 28\,\text{MHzmT}^{-1}$ and an external magnetic field $\mathbf{B}_{\text{ext}}$. Due to its host material the NV center has four different possible orientations pointing in the four corners of a tetraeder in the $\langle 1,1,1 \rangle$ directions. For a standard sample generated by electron or neutron irradiation all four possible orientations do have the same abundance of NV centers.

All the presented experiments were carried out on resonance (i.e. $\omega_c = \omega_s$; the central spin frequency is in resonance with the cavity mode), which makes it necessary to tune the spins into resonance with the cavity. Since the resonance of the cavity as introduced in Section 2.1 is fixed and defined by its intrinsic geometry, a magnetic field makes it necessary to tune the spins into resonance instead.

Under relatively weak field conditions ($|\mathbf{B}| \ll D/\mu_{\text{NV}}$, which is the case for magnetic fields $\lesssim 10\,\text{mT}$) the new resonance frequencies for the $m_s = 0$ to the excited state transitions under the action of an applied magnetic field are given by (we drop the E term and the energy offset of the D term)[78]

$$\omega_{\pm} \approx D \pm \mu_{\text{NV}} |B_z| + \frac{1}{2} \mu_{\text{NV}}^2 B_{\perp}^2 \frac{3D \mp \mu_{\text{NV}} |B_z|}{D^2 - \mu_{\text{NV}}^2 |B_z|^2}, \tag{3.24}$$

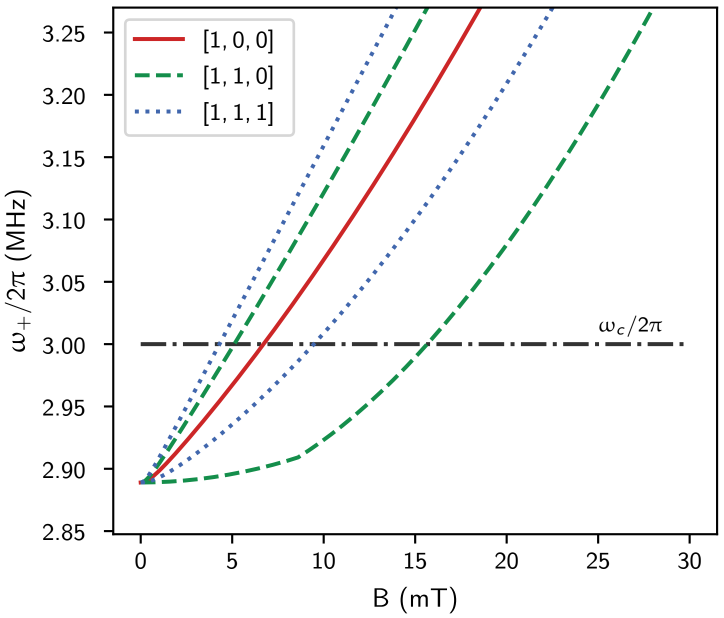

Figure 3.13: Dependence of the NV resonance frequency depending on the direction and strength of an external bias field. Shown is the response of $m_s = 0$ to the higher energy excited state transition of the different sub-ensembles for three different magnetic field directions (see legend). For the $[1, 0, 0]$ direction all four sub-ensembles experience the same shift in the resonance frequency. For the $[1, 1, 1]$ direction 3+1 and for the $[1, 1, 0]$ direction 2+2 NV-sub-ensembles experience the same projection of the magnetic field on their quantization axis, respectively.

with $B_\perp = \sqrt{B_x^2 + B_y^2}$. Here B_z is the axial magnetic field, with the z-direction the natural quantization axis pointing from the nitrogen to the vacancy.

Due to its special lattice symmetries we can tune one, two three or even four sub-ensembles into resonance with the cavity allowing us to change the number of spins coupled very precisely. For illustrative purposes let's consider a cavity with a resonance frequency of 3 GHz and a magnetic field in the

- $[1, 1, 1]$ direction: The projection of the magnetic field on the NV center in the $[1, 1, 1]$ direction is maximal and the perpendicular field for this sub-ensemble is zero, which simplifies Eq. (3.24) to

$$\omega_\pm \approx D \pm \mu_{\mathrm{NV}} \left| B_{\mathrm{tot}} \right| . \tag{3.25}$$

For a magnetic field of $B_{\mathrm{tot}} = 4.28\,\mathrm{mT}$ the $m_s = 0 \rightarrow +1$ transition of the sub-ensemble in the $[1, 1, 1]$ direction is in resonance with the cavity mode. The other three sub-ensembles all exhibit an angle between the magnetic field and their spin principle axis of $\cos(\theta) = 1/3$ which puts them at a frequency of

$$\omega_+ \approx D + \frac{\mu_{\mathrm{NV}}}{3} |B_{\mathrm{tot}}| + \frac{4}{3}\mu_{\mathrm{NV}}^2 B_{\mathrm{tot}}^2 \frac{9D - \mu_{\mathrm{NV}} |B_{\mathrm{tot}}|}{9D^2 - \mu_{\mathrm{NV}}^2 |B_{\mathrm{tot}}|^2} = 2\pi \cdot 2.926\,\mathrm{GHz}, \quad (3.26)$$

and far away from the resonance frequency of the cavity.

If we increase the total magnetic field to $B_{\mathrm{tot}} = 9.43\,\mathrm{mT}$ these three sub-ensembles are at a frequency of 3 GHz and in resonance with the cavity. The sub-ensemble parallel to the magnetic field has its resonance frequency at 3.144 GHz

- $[1, 1, 0]$ direction: Two and two sub-ensembles experience the same magnetic field, since the angle between the NVs in the $[1, 1, 1]$ and $[-1, -1, 1]$ direction and the magnetic field is $\cos(\theta_1) = \sqrt{2/3}$, and the angle between the sub-ensembles in the $[1, -1, -1]$ and $[-1, 1, -1]$ and the magnetic field is $\theta_2 = \pi/2$.

  For the first two sub-ensembles this gives

  $$\omega_+ \approx D + \sqrt{\frac{2}{3}}\mu_{\mathrm{NV}} |B_{\mathrm{tot}}| + \frac{1}{6}\mu_{\mathrm{NV}}^2 B_{\mathrm{tot}}^2 \frac{9D - \sqrt{6}\mu_{\mathrm{NV}} |B_{\mathrm{tot}}|}{3D^2 - 2\mu_{\mathrm{NV}}^2 |B_{\mathrm{tot}}|^2}, \quad (3.27)$$

  which for a total magnetic field of $B_{\mathrm{tot}} = 5.09\,\mathrm{mT}$ brings these two sub-ensembles into resonance with the cavity. Since for the other two sub-ensembles only non-axial fields exist, they are getting tuned negligibly only.

- $[1, 0, 0]$ direction: For such a magnetic field all four sub-ensembles have the same angle between their spin principle axis and the magnetic field of $\cos(\theta) = \sqrt{1/3}$ and experience the same shift of frequency. Therefore, we get for the shift

  $$\omega_+ \approx D + \sqrt{\frac{1}{3}}\mu_{\mathrm{NV}} |B_{\mathrm{tot}}| + \mu_{\mathrm{NV}}^2 B_{\mathrm{tot}}^2 \frac{9D - \sqrt{3}\mu_{\mathrm{NV}} |B_{\mathrm{tot}}|}{9D^2 - 3\mu_{\mathrm{NV}}^2 |B_{\mathrm{tot}}|^2}, \quad (3.28)$$

  for all four sub-ensembles, which for a total magnetic field of $B_{\mathrm{tot}} = 6.68\,\mathrm{mT}$ brings all four sub-ensembles into resonance simultaneously.

The number of spins in each sub-ensemble is equivalent, as the generation of NV center is an isotropic process [79]. This gives a fast and reliable way to change the number (and consequently the coupling strength) of spins coupled to the cavity mode.

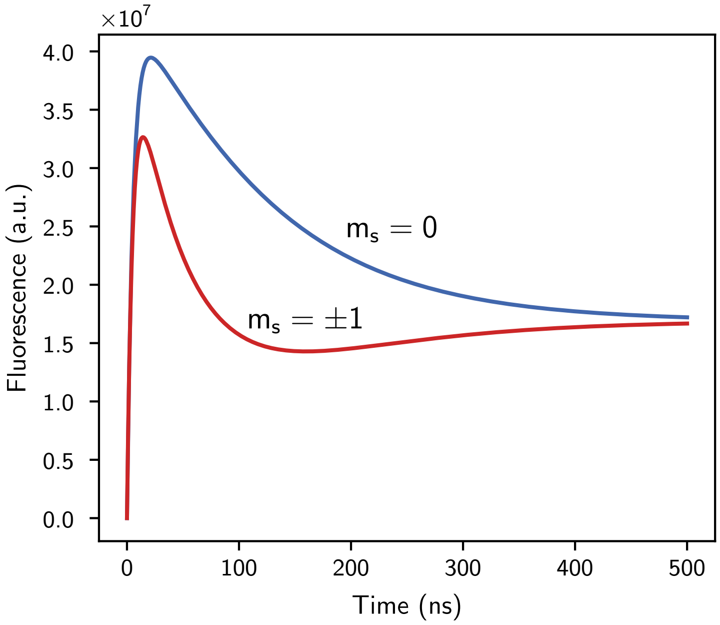

Figure 3.14: Fluorescence time traces for the two different spin projections with strong saturated excitation. The simulation is done using a simple five-level rate equation model with parameters taken from [81]

3.2.2 The Optical Transition and Thermal Polarization

Additional to a microwave spin triplet with a a ZFS of $\approx 2.88\,\mathrm{GHZ}$ which we use to couple to a cavity mode, the NV center has an optically exited state that also exhibits a spin triplet (see Fig. 3.15). The transition between the optical ground state and the exited state are spin conserving with a wavelength of $637\,\mathrm{nm}$ [75]. Symmetry considerations imply that the NV center also features a meta-stable state that is relatively long-lived compared to the excited state ($\approx 300\,\mathrm{ns}$). What makes this excited state transition so useful is the fact that the excited state $m_s = 0$ state has a high probability to decay back to its ground state, emitting a red photon, while the excited $m_s = \pm 1$ states have a high probability to non-radiatively decay to the meta-stable state and from there decay back into the $m_s = 0$ ground state (see Fig. 3.15). This means that the optical transition cannot only be used to polarize the spins into the $m_s = 0$ state after a few optical cycles, with rather high fidelity [80], but the $m_s = \pm 1$ states, due to the non-radiative processes emit fewer red photons when decaying back into the ground state and therefore show lower fluorescence.

Further, due to its solid state character the NV center shows a large phonon sideband in the optically excited state [81] which means that it is not necessary to hit the

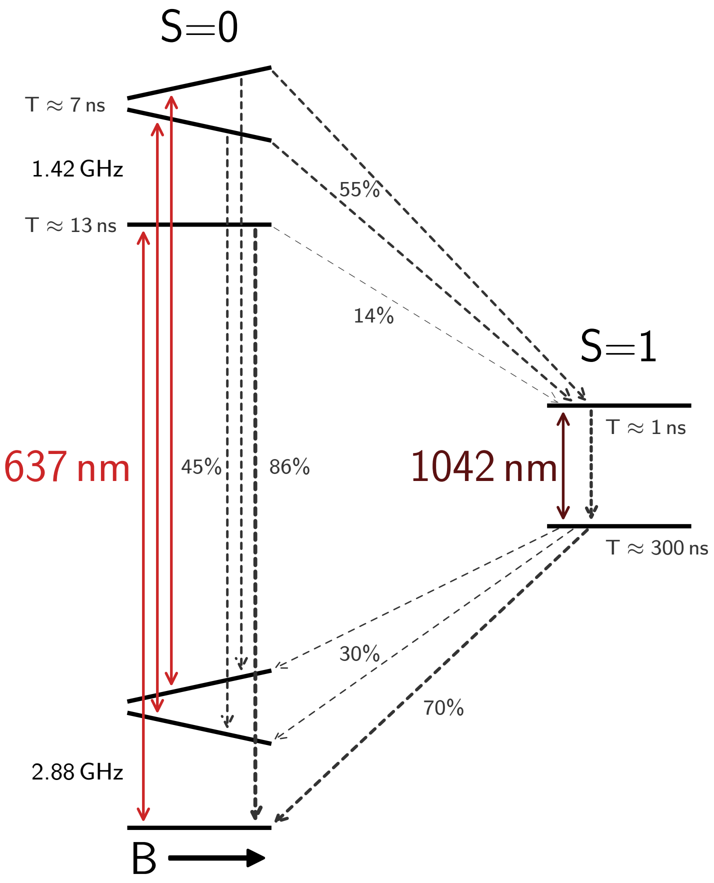

Figure 3.15: Term scheme of the NV center with the optical excited and ground state. Electrical dipole (i.e. optical photon emitting) transitions are indicated as solid (dark) red arrows with the transition rates written next to the dashed lines. The $m_s = 0$ state in the optical excited state almost exclusively decay back in the optical $m_s = 0$ state whereas the $m_s = \pm 1$ states primarily take the detour via a meta-stable state with a comparably long lifetime of ≈ 300 ns. This gives a fluorescence difference (i.e. less directly emitted red photons) that we can use to distinguish the $m_s = 0$ from the $m_s = \pm 1$ states (Numbers taken from [80]).

resonance exactly but we can excite the spins with off-resonant green light. That makes it rather easy to separate the green excitation light from the scattered red fluorescence to read out the spin state and reduces the requirements on the excitation laser. This property of the NV center is used in Section 4.2 where we use the optical transition to read out the spin state via a separate channel without the need of a cavity.

To create a Hybrid Quantum system with an ensemble of NV centers, the spin

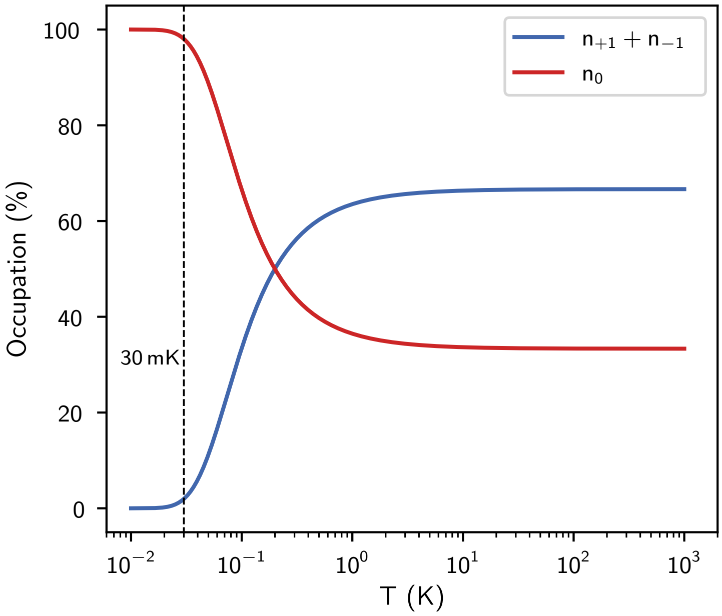

Figure 3.16: Thermal polarization of the NV center over temperature. The thermal mean value of the S_Z^2 operator (blue curve) tells us how many spins are thermally polarized in the ground state. The red curve shows the value of $1 - \langle S_z \rangle$, which is a measure for how many spins are thermally polarized in the ground state. For temperatures $< 50\,\mathrm{mK}$ almost all spins are in the $m_s = 0$ i.e. the ground state, with the $\langle S_Z^2 \rangle$-value close to zero. For temperatures $T \to \infty$ the polarization into the $m_s = \pm 1$ states approaches 2/3 and the spin system is in a completely mixed thermal state with the $m_s = 0$ and the $m_s = \pm 1$ states equally occupied.

temperature needs to be cold, since a thermal state does not couple to the cavity [53]. As derived in Section 2.2.2 the Hamiltonian couples the ground state of the system (all spins in the ground state and the cavity empty) to the first excited state (one excitation in the system shared between cavity and spins). As mentioned before, this could be done by optical pumping at room temperature (there are actual experiments showing strong coupling at room temperature [82, 83]), but considerations like thermal population of the cavity mode [84, 85], superconducting cavities and fidelity of the polarization make it useful to go to low temperatures, instead of relying on optical pumping.

The energy between the $m_s = 0$ and $m_s = \pm 1$ state in the NV center (without a magnetic field) corresponds to a temperature $T = \hbar D / k_\mathrm{B} = 138\,\mathrm{mK}$. By operating the experiments on a temperature much lower than that, we can, instead of optical pumping, use thermal polarization, to polarize the spins in the $m_s = 0$ state.

For an infinite temperature (i.e. room temperature for such a low energy transition), the steady state of the spins is a state equally distributed between the $m_s = 0, \pm 1$ states, with

$$\left\langle S_z^2 \left(T \gg \frac{\hbar\omega_{\mathrm{s}}}{k_{\mathrm{B}}} \right) \right\rangle_{\mathrm{st}} \approx \frac{2}{3}. \tag{3.29}$$

For zero temperature on the other hand all spins would be polarized in the lower energy ground state with

$$\left\langle S_z^2 \left(T = 0 \right) \right\rangle_{\mathrm{st}} = 0. \tag{3.30}$$

The steady state for an arbitrary temperature can be derived by Maxwell-Boltzmann statistics (for the three level term scheme of the NV center), as

$$\frac{\langle n_i \rangle}{\sum n_i} = \frac{1}{Z} g_i e^{-\varepsilon_i / kT}, \tag{3.31}$$

with g_i the degeneracy of the energy level, and Z the partition function as

$$Z = \sum_i g_i e^{-\varepsilon_i / kT}. \tag{3.32}$$

The individual n_i describe the occupation of the respective energy levels. The Maxwell-Boltzmann statistics describe the average occupation of each level, for a given temperature T. For the specific level scheme of the NV center with its two (almost) degenerate excited states, the occupation of the $m_s = \pm 1$ (i.e. $n_{+1} + n_{-1}$) levels can be interpreted as the expectation value of the $\langle S_z^2 \rangle$ operator in the steady state (cf. previous paragraph).

It immediately follows, that

$$n_{+1} + n_{-1} = \frac{2}{e^{\frac{\hbar\omega_{\mathrm{s}}}{k_{\mathrm{B}} T}} + 2}, \tag{3.33}$$

and

$$n_0 = \frac{1}{2 e^{\frac{-\hbar\omega_{\mathrm{s}}}{k_{\mathrm{B}} T}} + 1}. \tag{3.34}$$

The polarization depending on the temperature is shown in Fig. 3.16, and shows that operating below 50 mK achieves polarization in the ground state of above 95%. Since all of the experiments presented are typically carried out at 30 mK, after the spins had enough time to reach their equilibrium state (which can be annoyingly long [53]), we start our experiments with our spin states in an almost perfect ground state.

3.3 The Experimental Setup

Due to the reasons mentioned in the previous section, all the experiments are carried out at temperatures $< 50\,\mathrm{mK}$, which is made possible by using a ^{3}He/^{4}He dilution refrigerator. The cryostat used is an Oxford Instruments Triton 400 fridge with a cooling power of $400\,\mu\mathrm{W}$ at a base temperature of $100\,\mathrm{mK}$.

The operating principle of a dilution refrigerator is, that below a critical temperature of $870\,\mathrm{mK}$ a ^{3}He/^{4}He mixture undergoes a phase separation, forming a ^{3}He rich phase and a ^{3}He dilute phase (with a minimum of 6.5% ^{3}He [86]). Due to their different densities the mixture is arranged in layers with the ^{3}He rich phase on top. By removing ^{3}He from the diluted mixture by pumping on it (with turbo pumps), ^{3}He from the rich phase has to condense into the diluted mixture. This removes energy as condensation energy from the system and cools it down [86].

This guarantees cooling power down to very low temperatures (in principle down to $0\,\mathrm{K}$) since the minimum amount 6.5% of ^{3}He in the mixture is maintained, even at $0\,\mathrm{K}$.

The precooling down to $870\,\mathrm{mK}$ is done with a pulse-tube cooler [87] that can reach temperatures of about $2.7\,\mathrm{K}$. Going below the critical temperature of $870\,\mathrm{mK}$ where the condensation of the mixture is working, is then achieved by evaporative cooling on ^{3}He. With the condensation procedure, temperatures below $30\,\mathrm{mK}$ can be achieved, routinely.

The experimental setup can be seen in Fig. 3.17, where a photograph shows the lowest stage of the experiment and a schematic of the microwave setup. To study our cavity QED system we always measure the transmission of the system as derived in Section 3.1.4. To measure the transmission, we use a VNA (Keysight E5071C ENA Vector Network Analyzer) that allows to measure the scattering parameters directly. This VNA offers high dynamic range and a low noise floor, but it only allows to measure steady states as its temporal resolution is limited.

For time-resolved measurements we use a home-built auto-dyne detection scheme. We modulate a waveform on a carrier frequency using an arbitrary waveform generator and an IQ-mixer (IQ LMP1545 Marki Microwave) (more details on that in the following section). The signal is then fed into the fridge where the Hybrid System is mounted on the coldest stage, and the transmitted signal is demodulated again with an IQ-mixer and referenced to the same carrier frequency.

Next, 3D Helmholtz magnetic coil cages allow to apply magnetic fields in arbitrary directions of up to $100\,\mathrm{mT}$. The resonator (either a superconducting 2D resonator or a Lumped 3D resonator) is placed in this Helmholtz cage, with semi-rigid SMA cables going down from room temperature to $30\,\mathrm{mK}$, properly heatsinked and attenuated

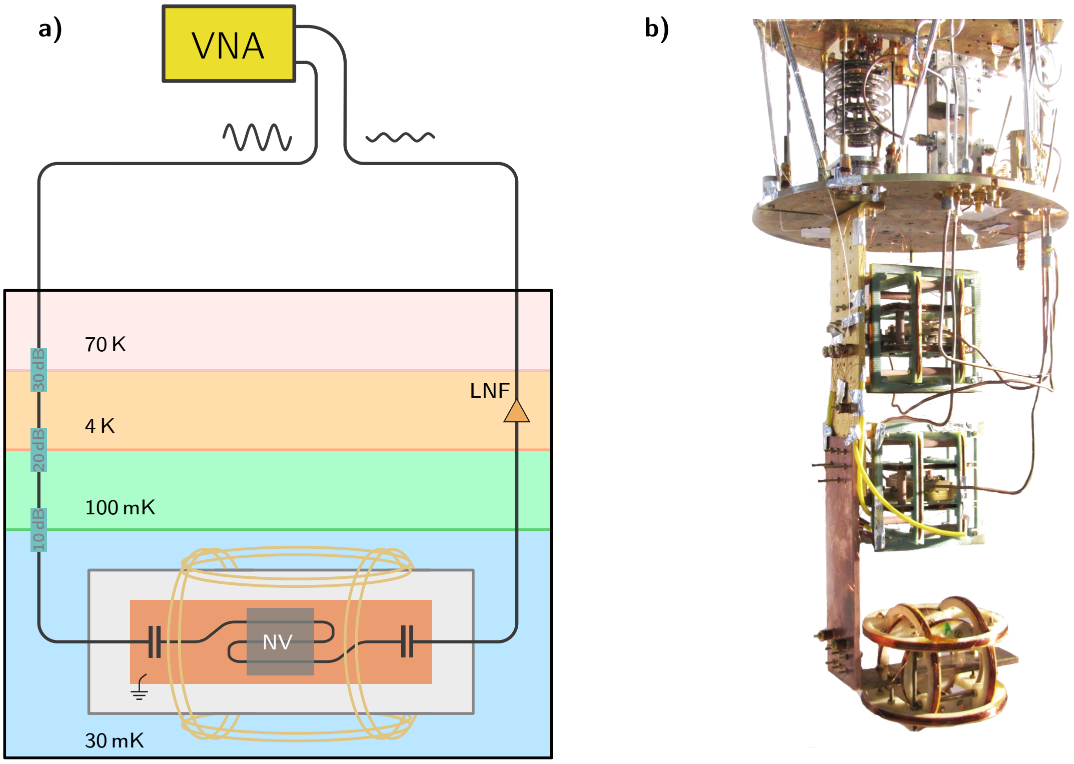

Figure 3.17: **a)** Frequency response measurement scheme using a Vector Network Analyzer (VNA) to perform frequency spectrum measurements. The down-line to the resonator are heat-anchored on every stage to properly cool down the line. A low-noise amplifier (LNF) amplifies the signal coming out of the resonator, which is then fed back into the VNA, which then measures the forward scattering parameter $S21(\omega)$. **b)** Photograph of the lowest stage of the fridge showing three measurement setups, each with their respective 3D Helmholtz magnetic field cage (Source: [88]).

at each stage when working in the low photon regime (as in Section 4.1) or with the attenuators removed when working in the high excitation regime (as in Section 4.2). These attenuators make sure that thermal photons from higher temperatures do not heat up the spin system and/or thermally occupy the cavity mode.

With the 3D lumped element resonator it is possible to open a small hole on one side of the resonator to allow putting a fiber into it (see Fig. 3.18). This allows to make use of the optical transition of the NV center and read out the spin state. For that we glue the fiber on one side of the diamond sample (with super glue) such that we illuminate a small part of the sample. Since this resonator manipulates all spins equally due to its homogeneous coupling strength, reading out only a small part of the spin ensemble makes it possible to extrapolate to the whole ensemble. We use a multimode fiber coupled into the fridge to illuminate with green 532 nm light from a fast bandwidth laser-diode, and use an avalanche photo-diode to measure the scattered

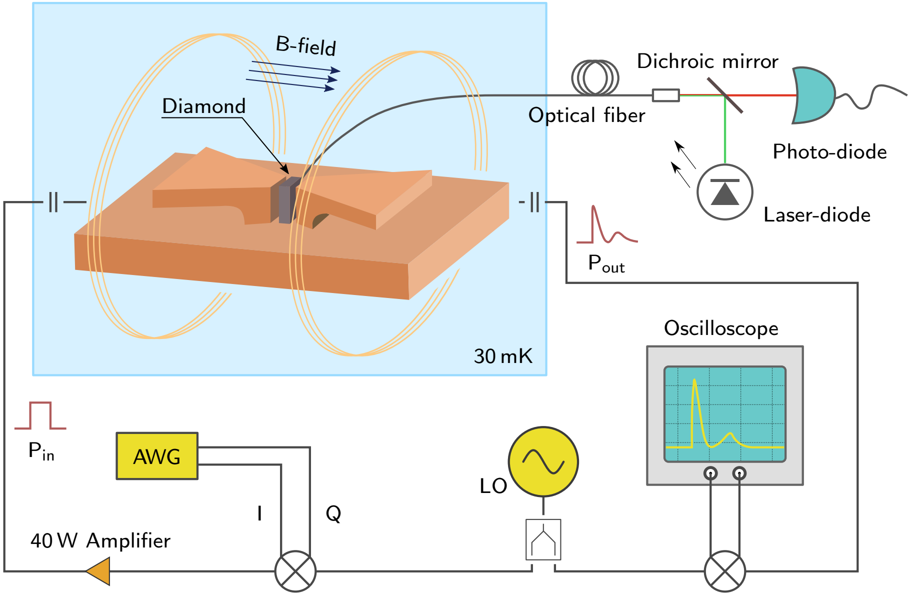

Figure 3.18: Experimental setup for time resolved measurements showing our homo-dyne detection setup. A local oscillator (LO) frequency source sends in the probe tone which is split up with one arm going into the fridge and the other one used for reference. An IQ mixer modulates a signal from a fast AWG onto the carrier signal which is then amplified and sent into the fridge. The signal going through the fridge is down-modulated using the reference signal and recorded by a fast oscilloscope. Shown is also the optical detection scheme where a fast laser-diode provides short green laser pulses which are sent to the NV center using a multimode fiber. The scattered fluorescence is then collected by the same fiber and measured by an avalanche photo-diode (Source: [89])

red fluorescence. The red light is collected through the same fiber with a dichroic mirror separating the in-going green laser light and the scattered red light.

Only a read-out of the spins using very short (i.e. 50 ns) optical pulses is possible. A polarization in the ground state, which is usually done at room temperature experiments, would not only deposit way too much power, which would heat up the fridge very quickly, but dense NV ensembles are usually also pitch black which does not allow to illuminate the whole ensemble; something necessary when trying to polarize the whole ensemble [1].

---

[1] Optical polarization of a whole ensemble can be achieved using total internal reflection [90], but the requirements on the sample and the necessary laser power of several Watts are very hard to meet in a fridge

3.3.1 Homo-dyne Measurement and IQ-modulation

Working in the microwave regime offers several advantages over optical photons (also certain disadvantages), be it availability of affordable devices due to its use in telecommunication industry, the easy to build and use wave-guides and cables, and last but not least the possibility to shape and modify them with relative ease.

Microwave radiation allows us to shape both quadratures of the radiation (or real and imaginary part; phase and magnitude) using relatively simple and affordable devices. We perform these manipulation using two mixers for frequency up and down conversion, both featuring quadrature amplitude manipulation. The first mixer up-converts two quadratures onto a carrier signal which is then sent into the fridge. The signal produced after up-conversion is given by

$$RF(t) = I(t)\cos(\omega_p t) - Q(t)\sin(\omega_p t)\,. \tag{3.35}$$

ω_p is the carrier frequency (usually tuned to the resonance frequency of the cavity), with the two (possibly time dependent) quadratures provided by a moderately fast arbitrary waveform generator (Agilent 33500B). It allows to change the phase of the applied drive by using either the I- or the Q-channel of the mixer.

The total input power of such a signal is given by $P_{\text{in}} = I^2(t) + Q^2(t)$.

The transmitted signal through the cavity is then down-converted using the same frequency source ω_p to measure the effect of the Hybrid System on the input drive and measured in two channels of a fast oscilloscope individually, which is able to measure the amplitude and the phase of the transmitted signal. The down-converted signals read [91]

$$\begin{aligned} I_{\text{meas}}(t) &= RF'(t)\cos(\omega_p t) \\ Q_{\text{meas}}(t) &= -RF'(t)\sin(\omega_p t)\,, \end{aligned} \tag{3.36}$$

with $RF'(t)$ the modified signal send through the fridge.

If one removes the device under test (i.e. $RF'(t) = RF(t)$) the down-converted signal becomes

$$\begin{aligned} I_{\text{meas}}(t) &= RF(t)\cos(\omega_p t) = \frac{1}{2}\left(I(t) + I(t)\cos(2\omega_p t) - Q(t)\sin(2\omega_p t)\right) \\ Q_{\text{meas}}(t) &= -RF(t)\sin(\omega_p t) = \frac{1}{2}\left(Q(t) - I(t)\cos(2\omega_p t) - Q(t)\sin(2\omega_p t)\right)\,, \end{aligned} \tag{3.37}$$

which (after a low pass filter) shows that the original signal is recovered.

Both quadratures can be understood analogous to an E- and B-field of an electromagnetic wave in the cavity (see Section 2.1). This allows to make the same derivation as for the driven Tavis-Cummings Hamiltonian in Eq. (2.40), which gives us an Hamiltonian taking into account both quadratures of the driving field as

$$H = \hbar\Delta_c \hat{a}^\dagger \hat{a} + \sum_{i=1}^{N} \frac{\hbar\Delta_s^i \sigma_z^i}{2} + i\hbar \sum_{i=1}^{N} g^i (\hat{\sigma}_-^i \hat{a}^\dagger - \hat{\sigma}_+^i \hat{a}) + i\hbar I(t)(\hat{a}^\dagger - \hat{a}) + \hbar Q(t)(\hat{a}^\dagger + \hat{a}). \quad (3.38)$$

This gives modified Maxwell-Bloch equations of the form

$$\begin{aligned} \dot{\langle a \rangle} &= -\kappa \langle a \rangle - i\Delta_c \langle a \rangle + \sum_j g_j \langle \sigma_-^j \rangle + I(t) - iQ(t) \\ \dot{\langle \sigma_-^j \rangle} &= -i\Delta_s^j \langle \sigma_-^j \rangle + g_j \langle a \rangle \langle \sigma_z^j \rangle - \left(\gamma_\perp + \frac{\gamma_\parallel}{2}\right) \langle \sigma_-^j \rangle \\ \dot{\langle \sigma_z^j \rangle} &= -\gamma_\parallel \left(1 + \langle \sigma_z^j \rangle\right) - 2g_j \left(\langle \sigma_-^j \rangle \langle a^\dagger \rangle + \langle \sigma_+^j \rangle \langle a \rangle\right). \end{aligned} \quad (3.39)$$

and full control of the spin system using (time-dependent) quadrature amplitudes $I(t)$ and $Q(t)$.

3.3.2 Numerical Modeling

The large system size and the, therefore, small influence of quantum fluctuations in the system makes it possible to very accurately model the experiment, using Eq. (3.39). It is virtually impossible to simulate 10^{16} spins (i.e. solve a set of $2 \times 10^{16} + 1$ coupled differential equations), therefore, some simplifications have to be made. To make the problem tractable we discretize the continuous spectral density as [92]

$$\rho(\omega) = \frac{1}{g_{\text{coll}}^2} \sum_{k=1}^{N} g_k^2 \delta(\omega - \omega_k). \quad (3.40)$$

With $\int \rho(\omega)\, \mathrm{d}\omega = 1$ (i.e. the spectral density is normalized) it is now straightforward to see that $g_{\text{coll}} = \sqrt{\sum_{k=1}^{N} g_k^2}$, which is of course the result we want to obtain and shows that the discretization is valid.

In order to obtain the individual coupling strengths for each k-value, we assume our spin distribution to be approximated by a set of rectangular bars, with width $\Delta\omega$ (see Fig. 3.19), which allows us to write

$$\int_{\omega_k - \Delta\omega/2}^{\omega_k + \Delta\omega/2} \rho(\omega)\, \mathrm{d}\omega \approx \rho(\omega_k)\, \Delta\omega = \frac{1}{g_{\text{coll}}^2} \int_{\omega_k - \Delta\omega/2}^{\omega_k + \Delta\omega/2} \sum_{k=1}^{N} g_k^2 \delta(\omega - \omega_k)\, \mathrm{d}\omega = \frac{g_k^2}{g_{\text{coll}}^2}. \quad (3.41)$$

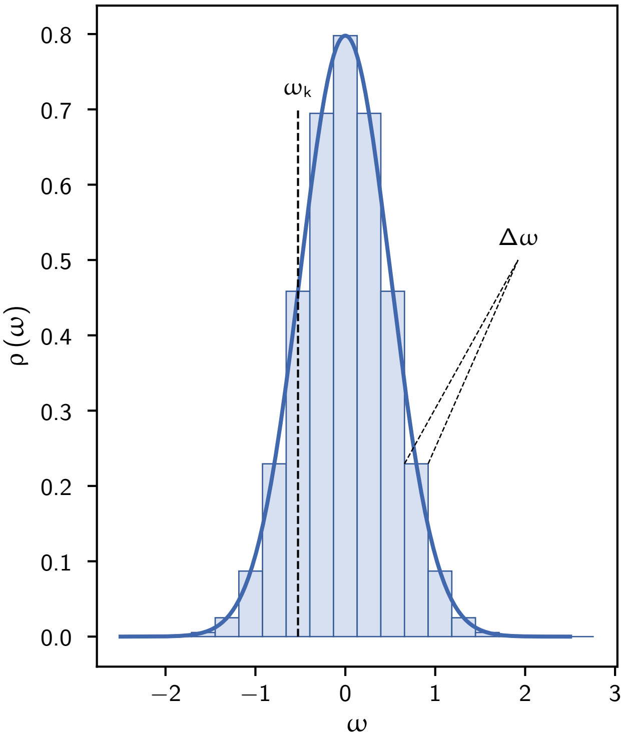

Figure 3.19: Discretization of the spin ensemble. Each frequency step ω_k is approximated by a rectangle with width $\Delta\omega$ for which the spin density is assumed to be constant (not to scale).

Since we know that $g_{\text{coll}}^2 = \sum g_k^2$, we finally get

$$\Delta\omega = \frac{1}{\sum_{k=1}^{N} \rho\left(\omega_k\right)}, \tag{3.42}$$

and

$$g_k = g_{\text{coll}} \sqrt{\frac{\rho\left(\omega_k\right)}{\sum_{k=1}^{N} \rho\left(\omega_k\right)}}. \tag{3.43}$$

If we now use this discretization for our coupling strength and assume a q-gaussian spin distribution $\rho(\omega)$, as it has been shown to be correct for ensembles of NV-center [84, 85, 92, 93], we can very accurately model our experiment by solving only $2N + 1$ differential equations (2 for each spin, and one for the cavity amplitude), a task possible using modern computer hardware, when using moderate values for N (≈ 1000).

To show how well this approach models our experiment, we show a simulation compared with data in Fig. 3.20b). The simulation was carried out with $N = 701$,

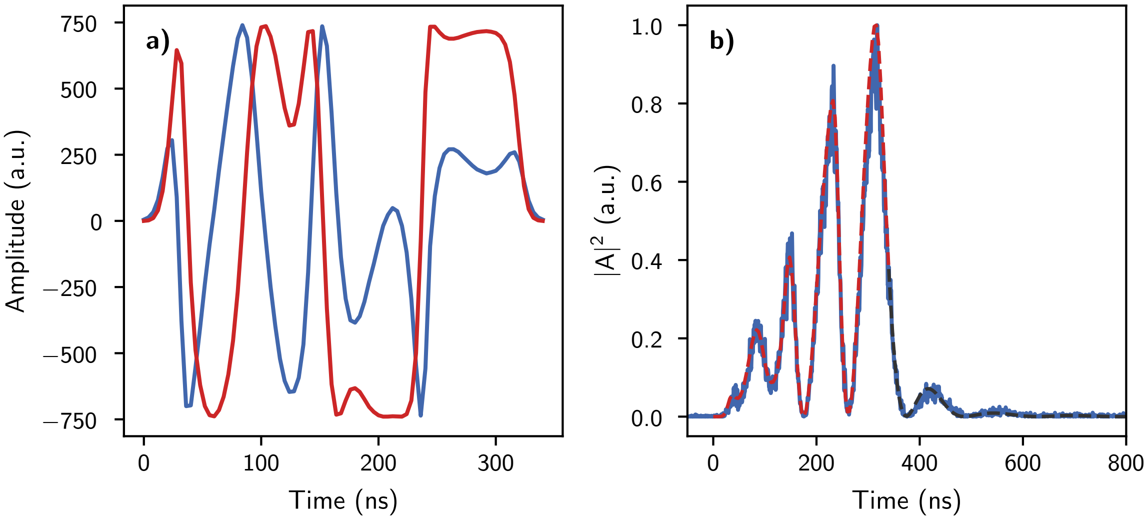

Figure 3.20: Comparison for experiment and theory. In **a)** we see the pulse that is send into the cavity, with non constant amplitude in both quadratures. In **b)** the resulting cavity amplitude is measured and compared to the simulation. Shown in blue is the experimental data, while the red curve shows the simulated cavity amplitude as long as the pulse is turned on, and the black dashed curve the simulated free evolution afterwards. The parameters for the simulation are as stated in the main text.

$g_{\text{coll}}/2\pi = 2.98\,\text{MHz}$, $\kappa/2\pi = 1.8\,\text{MHz}$, $\gamma_q = 2\,\text{MHz}$, $q = 1.98$ and a pulse that is not constant over time but has some oscillatory behavior in both quadratures as introduced in the previous section (see Fig. 3.20a); Section 5.1 explains the motivation for such pulses). Note that we apply the pulse with very little power, which means that we don't leave the linear regime. That makes it easier to compare to numerical results as it is not necessary to know the exact drive power in the experiment to model it numerically.

As it is apparent, the agreement between theory and experiment is almost perfect and allows us to accurately describe the occurring behavior. All subsequent numerical results have been obtained using this method.

4 Experiments

After developing the theoretical framework of cavity QED and presenting the experimental setup to perform these kind of experiments, let us know turn to the main part of this thesis: the presentation of the experimental results. I will present two experiments that both show, when and under which conditions our cavity QED system cannot be described with the Holstein-Primakoff approximation, qualitatively behaving differently than two coupled harmonic oscillators.

Both of the presented experiments are examples for such experiments and have been studied and understood since the early beginnings of quantum optics [50, 94–99]. However, observing them in a solid state system, which makes them much more useful to use in quantum technological applications, has proven to be a difficult problem.

Here we present the implementation in our solid state hybrid system in the microwave regime that allows us to study new regimes of these effects and study properties that are not present in most of the "standard" implementations.

4.1 Amplitude Bistability – Operating between the Linear and Non-linear Regime

Parts of this chapter are based on:

- **"Ultralong relaxation times in bistable hybrid quantum systems"**
  Andreas Angerer, Stefan Putz, Dmitry O. Krimer, Thomas Astner, Matthias Zens, Ralph Glattauer, Kirill Streltsov, William J. Munro, Kae Nemoto, Stefan Rotter, Jörg Schmiedmayer and Johannes Majer
  Science Advances (2017) Vol. 3, no. 12, e1701626

Amplitude bistability is one of the archetypical non-linear (or an-harmonic) effects in cavity QED and has been studied extensively both theoretically [94–96, 100] and experimentally [97, 98]. It is arguably the (experimentally) easiest experiments that leaves the harmonic regime of cavity QED which explains when and how the approximation of two coupled harmonic oscillators breaks down. For that we will first introduce the strong coupling regime of cavity QED where this approximation is still valid and shows eigenmodes one would also expect from a system of two coupled harmonic oscillators. By driving this system harder and harder this explanation, however, starts to break down and the an-harmonicity of the spin system becomes apparent.

Interestingly, these two regimes are connected by a first order phase transition (if the so-called cooperativity parameter is large enough) with a bistable region where depending on the history of the system two stable solutions exist.

We perform this experiments on a two dimensional transmission line resonator (see Section 3.1.2) as it offers easily accessible strong coupling. For this experiment we are also not sensitive to in-homogeneous coupling strengths, which makes a transmission line resonator suitable. The NV ensemble used is a neutron irradiated sample (BS13b in [71], N1 in [53]) with a high density of 40 ppm and a spectral distribution of a q-Gaussian [92, 93] with a q-value of $q = 1.39$ and a line-width of $\gamma_q = 2\pi \cdot 9.4\,\mathrm{MHz}$ (FWHM).

4.1.1 The Strong Coupling Regime of Cavity QED

The starting point to understand amplitude bistability, and why it is an experiment that leaves the linear regime of cavity QED, is to understand the strong coupling regime of cavity QED first.

In general the strong coupling regime of cavity QED is reached as soon as the losses in the system are smaller than the collective coupling strength $g\sqrt{N} \gg \Gamma + \kappa$, between the cavity and the spin system on resonance. Here Γ is an approximation of all spin losses in the system and incorporates $\gamma_\perp, \gamma_\parallel$ and in-homogeneous broadening (we will introduce a more formal definition in Section 4.1.2). A useful figure of merit is the system cooperativity parameter which sets these quantities in relation (again for a more formal definition the reader is referred to Section 4.1.2)

$$C = \frac{Ng^2}{\kappa\Gamma}. \tag{4.1}$$

In general a cooperativity value larger than one describes the case of strong coupling, whereas the case of $C < 1$ is known as the weak coupling regime where the losses in the system are dominating over the coupling strength. Note that this is only true if $\Gamma \approx \kappa$, i.e. by only making the cavity better and better one cannot enter the strong coupling regime, without improving the spin properties at the same time.

In the experiment we tune the magnetic field as described in Section 3.2.1 such that

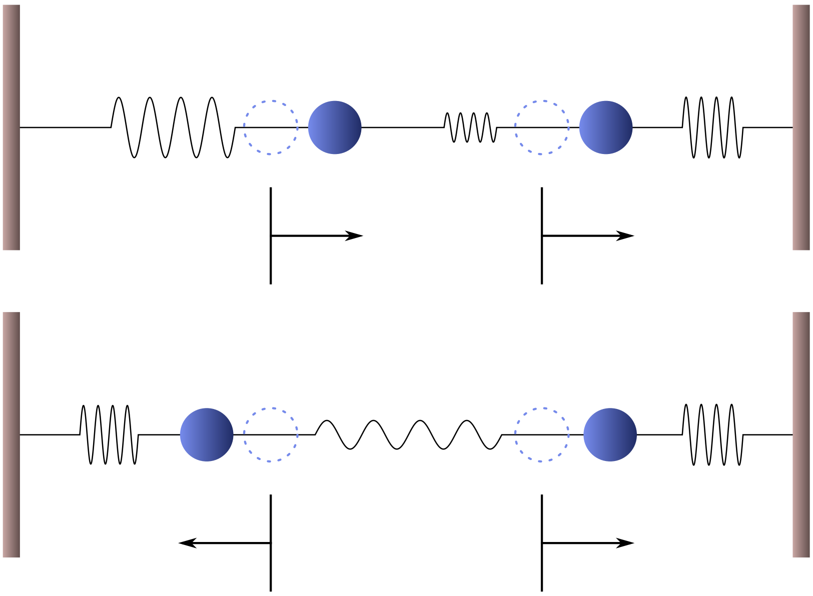

Figure 4.1: The two eigenmodes of a coupled harmonic oscillator system. The oscillators can be either in phase, oscillating in the same direction (upper plot), which corresponds to the symmetric eigenstate in the experiment, or out of phase, oscillating against each other, corresponding to the anti-symmetric eigenstate. In the case of these classical oscillators the anti-symmetric mode has the higher energy (contrary to our cavity-spin system) due to a negative sign in the coupling force.

(e.g. two) sub-ensembles are in resonance with the cavity. From Eq. (2.28) we know that the collective coupling strength scales with $\sqrt{N}$.

If we probe the system with very little power such that the cavity occupation number is much smaller than the number of spins ($a^\dagger a \ll N$) the Holstein-Primakoff approximation is valid and we observe the eigenmodes of a two coupled harmonic oscillator system (see Fig. 4.1), coupled with the coupling strength $g\sqrt{N}$. The two oscillators can either oscillate in phase or out of phase as

$$|\pm\rangle = \frac{1}{\sqrt{2}} \left(|10\rangle \pm |01\rangle \right), \tag{4.2}$$

with eigenenergies

$$E_\pm = \hbar\omega_c \pm \hbar g \sqrt{N}. \tag{4.3}$$

The symmetric state gains energy from the coupling whereas the anti-symmetric one loses energy.

This behavior can be seen in Fig. 4.2a) where we tune the spins in and out of resonance with the cavity using a magnetic field. Far from resonance the cavity behaves

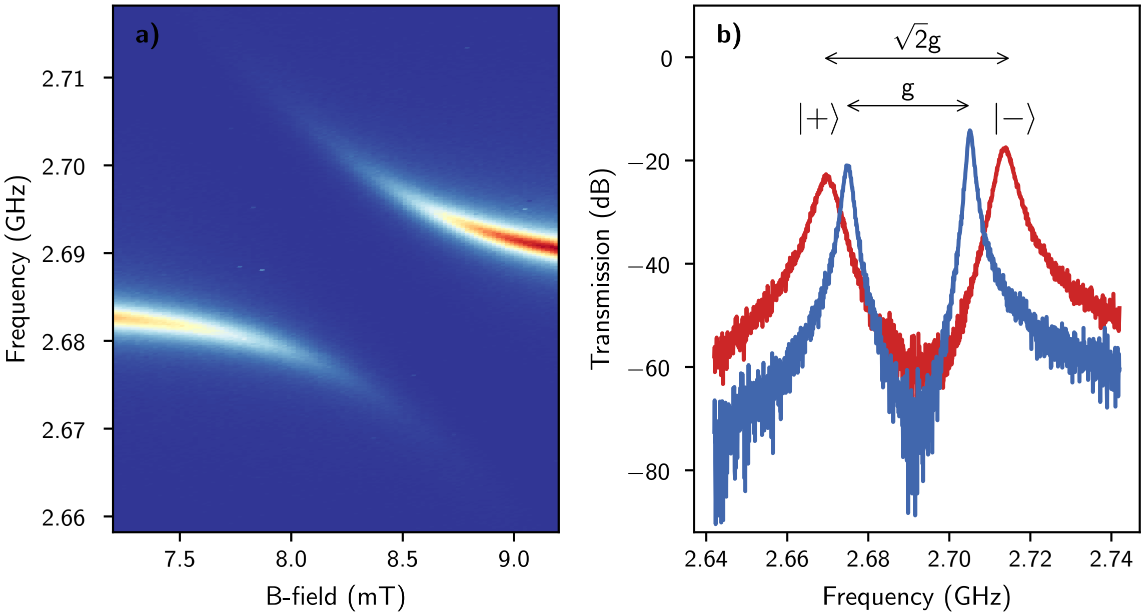

Figure 4.2: **a)** Magnetic field spectroscopy on our hybrid system with two sub-ensembles in resonance with the cavity, showing the transmission through the cavity. By tuning the spins into resonance we see that the eigenstates split up with the maximum separation on resonance, for a magnetic field of 8.4 mT. **b)** Measured strong coupling with two (blue) or four (orange) sub-ensembles in resonance with the cavity. Increasing the number of spins by a factor of two corresponds to an increase in the splitting by a factor of $\sqrt{2}$. The two eigenstates ($|+\rangle$ and $|-\rangle$) are clearly distinguishable in both cases. The slight asymmetry in the peak height stems from a Fano resonance [101].

like a single harmonic oscillator that exhibits a Lorentzian response to a drive. On resonance the eigenmodes of the coupled system become apparent and we observe an avoided crossing with a splitting $\Delta\omega = 2\sqrt{N}g$.

By bringing more spins into resonance with the cavity mode we also observe the typical $\sqrt{N}$ behavior as can be seen in Fig. 4.2b) where we observe that changing the number of spins by a factor of two, changes the splitting by a factor of $\sqrt{2}$.

4.1.2 Steady-state Bistability

Observing strong coupling in our system is the first step towards understanding the behavior of bistability. All the considerations in the previous section have been carried out in the low-excitation regime where the system is driven very weakly in order not to disturb the spin system. Due to this small drive the Holstein-Primakoff approximation with $S_z \equiv -N/2$ is applicable and we observe the eigenmodes of two coupled harmonic oscillators. It should be noted that for such a transmission spectroscopy, only the steady state of the system is of interest, since all the relevant dynamics happen on a timescale much shorter than the probing frequency of the vector network analyzer.

Operating between two Regimes

When driving the system harder, a different approach is necessary to understand the steady state behavior of the system, and the simple approximation $S_z \equiv -N/2$ cannot be applied anymore. We take the Maxwell-Bloch equations as in Eq. (2.49) and, as we are only interested in the steady state of the system set all time derivatives to zero. This gives (for clarity we omit all the symbols for the expectation values)

$$\begin{aligned} 0 &= -\kappa a - i\Delta_c a + \sum_j g_j \sigma_-^j + \eta \\ 0 &= -i\Delta^j \sigma_-^j + g_j a \sigma_z^j - \left(\gamma_\perp + \frac{\gamma_\parallel}{2}\right) \sigma_-^j \\ 0 &= -\gamma_\parallel \left(1 + \sigma_z^j\right) - 2g_j \left(\sigma_-^j a^\dagger + \sigma_+^j a\right). \end{aligned} \tag{4.4}$$

Expressing σ_-^j from the second equation gives

$$\sigma_-^j = \frac{2g_j a \sigma_z^j}{\gamma_\parallel + 2\gamma_\perp + 2i\left(\Delta_c + \Delta^j\right)}, \tag{4.5}$$

with $\Delta^j = \omega_s^j - \omega_c$ the detuning from the respective spin to the cavity resonance frequency. Putting that in the first and the third equation then gives

$$\begin{aligned} \sigma_z^j &= -\frac{\gamma_\parallel}{\gamma_\parallel + \frac{8\left(\gamma_\parallel + 2\gamma_\perp\right)|a|^2 g_j^2}{\gamma_\parallel^2 + 4\gamma_\parallel\gamma_\perp + 4\left(\gamma_\perp^2 + \Delta_c^2\right) + 8\Delta_c\Delta^j + 4\Delta_j^2}}, \\ |a|^2 &= \frac{\eta^2}{\kappa^2\left(1 - \sum_{j=1}^n \frac{2\left(\gamma_\parallel + 2\gamma_\perp\right) g_j^2 \sigma_z^j}{\kappa\left(4\Delta_c^2 + 4\Delta^j(2\Delta_c + \Delta^j) + \left(\gamma_\parallel + 2\gamma_\perp\right)^2\right)}\right)^2 + \left(\Delta_c + \sum_{j=1}^n \frac{4g_j^2(\Delta_c + \Delta^j)\sigma_z^j}{\left(\gamma_\parallel + 2\gamma_\perp\right)^2 + 4\Delta_c^2 + 4\Delta^j(2\Delta_c + \Delta^j)}\right)^2}, \end{aligned} \tag{4.6}$$

with n the total number of the spins coupled. In the following we only consider a drive resonant with the cavity (i.e. $\Delta_c = 0$), which simplifies these expressions to:

$$\begin{aligned} \sigma_z^j &= -\frac{\gamma_\parallel}{\gamma_\parallel + \frac{8\left(\gamma_\parallel + 2\gamma_\perp\right)|a|^2 g_j^2}{\left(\gamma_\parallel + 2\gamma_\perp\right)^2 + 4\Delta_j^2}}, \\ |a|^2 &= \frac{\eta^2}{\kappa^2\left(1 - \sum\limits_{j=1}^{n} \frac{2\left(\gamma_\parallel + 2\gamma_\perp\right) g_j^2 \sigma_z^j}{\kappa\left(4\Delta_j^2 + \left(\gamma_\parallel + 2\gamma_\perp\right)^2\right)}\right)^2 + \left(\sum\limits_{j=1}^{n} \frac{4 g_j^2 \Delta^j \sigma_z^j}{\left(\gamma_\parallel + 2\gamma_\perp\right)^2 + 4\Delta_j^2}\right)^2}. \end{aligned} \tag{4.7}$$

The second equation can be simplified even further by assuming a symmetric spin distribution around its center frequency (which is generally the case), since the sum $(\sum \Delta_j)^2$ averages to zero. We are finally left with

$$\begin{aligned} \sigma_z^j &= -\frac{\gamma_\parallel}{\gamma_\parallel + \frac{8\left(\gamma_\parallel + 2\gamma_\perp\right)|a|^2 g_j^2}{\left(\gamma_\parallel + 2\gamma_\perp\right)^2 + 4\Delta_j^2}} \\ |a|^2 &= \frac{\eta^2}{\kappa^2\left(1 - \sum\limits_{j=1}^{n} \frac{2\left(\gamma_\parallel + 2\gamma_\perp\right) g_j^2 \sigma_z^j}{\kappa\left(4\Delta_j^2 + \left(\gamma_\parallel + 2\gamma_\perp\right)^2\right)}\right)^2}. \end{aligned} \tag{4.8}$$

We can now define the aforementioned cooperativity factor for a single spin as

$$C_j = \frac{g_j^2}{\kappa\left(\frac{\gamma_\parallel}{2} + \gamma_\perp\right)\left(1 + \frac{\Delta_j^2}{\left(\frac{\gamma_\parallel}{2} + \gamma_\perp\right)^2}\right)}, \tag{4.9}$$

and the collective cooperativity as $C_{\text{coll}} = \sum C_j$. With this definition of cooperativity the steady state solution for the cavity intensity and the inversion simplifies to

$$\begin{aligned} \sigma_z^j &= -\frac{1}{1 + \frac{4|a|^2 C_j \kappa}{\gamma_\parallel}}, \\ |a|^2 &= \frac{\eta^2}{\kappa^2\left(1 - \sum\limits_{j=1}^{n} C_j \sigma_z^j\right)^2}. \end{aligned} \tag{4.10}$$

We can immediately see that this gives rise to different regimes. As long as the

Holstein-Primakoff approximation is valid (i.e. $\sigma_z^j = -1$) the cavity transmission is

$$|T|^2 = \frac{\kappa^2 |a|^2}{\eta^2} = \frac{1}{(1 + C_{\text{coll}})^2}, \tag{4.11}$$

which for a collective cooperativity that is large tends towards zero. It should be noted that strictly speaking the transmission intensity as given above is only valid for an over-coupled symmetric cavity (see Section 3.1.4). As this is the case in the following experiment, the statement holds true.

Driving the system strongly and with a lot of photons in the cavity mode, Eq. (4.10) tells us that $\sigma_z^j = 0$ for $|a|^2 \to \infty$. Thus, the transmission through the cavity becomes

$$|T|^2 = \frac{\kappa^2 |a|^2}{\eta^2} = 1. \tag{4.12}$$

This behavior can be understood as the transition between a system that acts like two coupled harmonic oscillators in the low excitation regime, which gives low transmission when driven on resonance due to the normal mode splitting, to the point where the spin system is completely saturated and does effectively not couple to the cavity mode anymore. All that is left in this scenario is the bare cavity transmission function.

Bistable Behavior

As presented in the previous paragraph a large cooperativity parameter gives rise to two different regimes of cavity QED and a breakdown of the Holstein-Primakoff approximation when driving the system strongly. However, so far we only have looked at two extreme cases where the system is either driven very weakly or very strongly.

To understand the steady states in between these two extremes, we can first reduce the two equations for the spin inversion and the intra-cavity intensity to a single equation as

$$|a|^2 = \frac{\eta^2}{\kappa^2 \left(1 + \sum\limits_{j=1}^{n} \frac{C_j}{1+|a|^2/n_0^j}\right)^2}. \tag{4.13}$$

Here we introduced the additional dimensionless parameter $n_0^j = \gamma_\| / 4 C_j \kappa$, sometimes called the saturation photon number [102]. $n_0 = \sum n_0^j$ is (roughly) the number of photons necessary in the cavity mode where the Holstein-Primakoff approximation starts to break down [44].

This equation does not have a closed solution for $|a|^2$ and therefore can only be

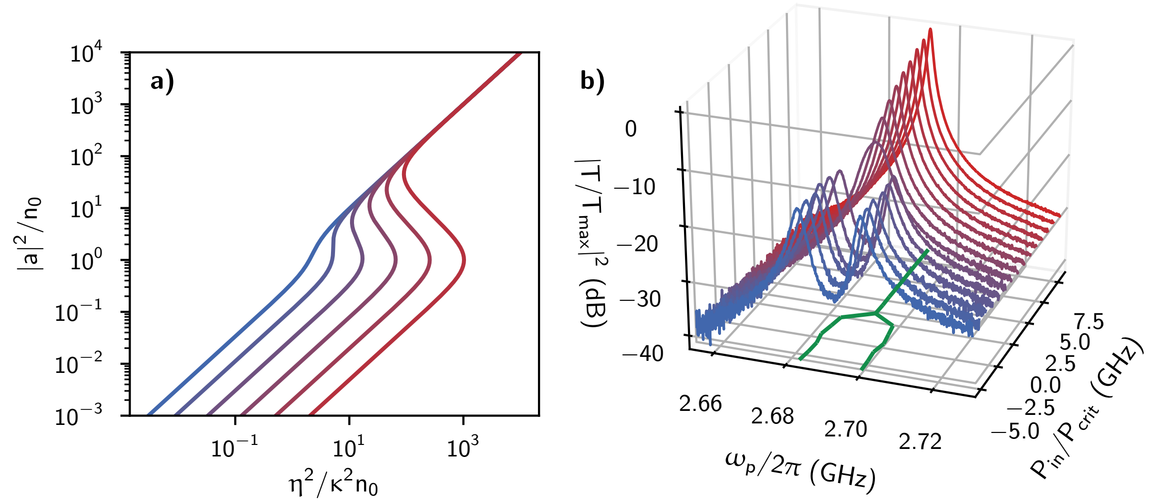

Figure 4.3: a) Steady state bistability simulated according to Eq. (4.15) for different values of cooperativity ($C = 2, 8, 32, 128, 512, 2048$ from blue to red) for a single spin without detuning in resonance with the cavity mode. We observe that starting with a critical cooperativity of $C = 8$ the system starts to exhibit three stable solutions for one input power. This is the effect known as amplitude bistability. **b)** Measured steady state transmission spectra for different drive powers for two sub-ensembles in resonance with the cavity mode. For small drive powers the system behaves like two coupled harmonic oscillators, and exhibits normal mode splitting; for a certain critical drive power ($P_{\text{in}} = P_{\text{crit}}$) the splitting vanishes and only one peak is visible (note the green curve denoting the position of the maxima/maximum) (Source [103])

solved numerically. However, we already see that this equation is a non-linear equation in $|a|$ with the cooperativity value defining how large this non-linearity becomes.

To gain qualitative understanding of this equation, we only consider a single spin coupled to the cavity mode, such that the equation simplifies to

$$|a|^2 = \frac{\eta^2}{\kappa^2 \left(1 + \frac{C}{1+|a|^2/n_0}\right)^2}. \tag{4.14}$$

With $x^2 n_0 = |a|^2$ and $y^2 = \eta^2/\kappa^2 n_0$, the now dimensionless equation finally simplifies to

$$y^2 = \frac{x^2\left(1 + C + x^2\right)^2}{\left(1 + x^2\right)^2}. \tag{4.15}$$

In Fig. 4.3a) we plot the steady states as computed from Eq. (4.15) and different cooperativity values. This plot shows that for a certain cooperativity value ($C \geq 8$) the transmission (or intra-cavity intensity) starts to show more than one stable solution for a given input power y.

This behavior is known as amplitude bistability, where operating between these two regimes shows two stable solutions depending on the history of the system. Which steady state the system tends towards, depends on the history of the system.

Even though an analytic solution is not possible in a many spins scenario with different cooperativity values for each spin, numerical simulations show a similar behavior. If the system starts from a state that is driven weakly, the steady state it approaches is the one in the lower branch. If, however, the system is prepared in the strongly driven branch, the system relaxes to the steady state in the upper branch.

Experimental Implementation

We perform the steady-state experiments on a $\lambda/2$-transmission line resonator (see Section 2.1) with a cavity line-width of $\kappa/2\pi = 440\,\mathrm{kHz}$ (HWHM) and a fundamental resonance frequency of $\omega_c/2\pi = 2.691\,\mathrm{GHz}$. The cavity is operating in the over-coupled regime such that the internal losses of the cavity are much smaller than the coupling losses ($\kappa_{\text{int}} \ll \kappa_{\text{ext}}$), which allows to approximate the total losses as $\kappa \approx \kappa_{\text{ext}}$. The system is always probed with a frequency resonant with the cavity resonance frequency $\omega_p = \omega_c$. This cavity design gives us a single spin coupling rate of $g \approx 12\,\mathrm{Hz}$. We estimate the transverse relaxation rate as $\gamma_\perp/2\pi \leq 33\,\mathrm{kHz}$ and the longitudinal relaxation rate as $\gamma_\parallel/2\pi \leq 3.6\,\mathrm{mHz}$ ($T_1 = 44\,\mathrm{s}$)[30][1].

The spin system has a spin density according to a q-Gaussian distribution [84, 85], with a full-width-half-maximum line-width of $\gamma_q = 2\pi \cdot 9.4\,\mathrm{MHz}$ and shape parameter $q = 1.39$ [93] (For more information about the sample and the implications of the specific shape of the spin distribution the reader is referred to [93]).

We perform this experiment for three different cooperativity values which we change by bringing two or four sub-ensembles into resonance with the cavity. This changes the collective cooperativity value by roughly a factor of two. Since the experiment is performed on a transmission line resonator we can only apply magnetic fields parallel to the $[1, 1, 0]$ direction, which limits us to the case of either two of four sub-ensembles in resonance with the cavity mode (see Section 3.2.1). The thin superconducting Niobium layer of the resonator does not allow magnetic fields perpendicular to it. Niobium as a type II superconductor would create normal conducting vortices until the superconductivity breaks down which lowers the quality of the cavity until the resonance

---

[1] As we learned later [53], this is actually not the real T_1 time, but the spin diffusion time T_1^*, which is orders of magnitude shorter than the real one. Since it has the same effect in this experiment we use it here as an effective T_1 time.

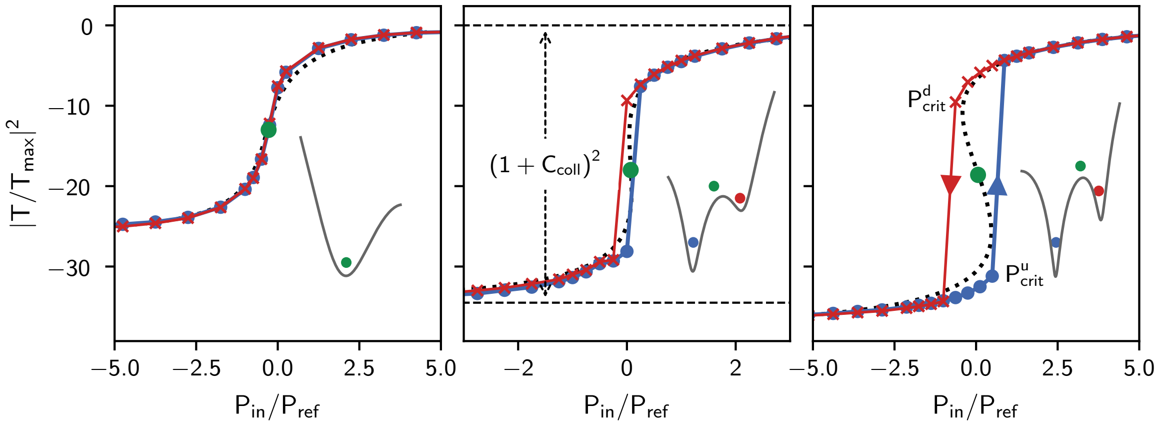

Figure 4.4: Measurement of the steady-state bistability transmission through the cavity as a function of increasing (blue) and decreasing (red) input power P_{in}. In **a)**, the transmission measurements are plotted for the cooperativity value $C_{\text{coll}} \approx 18$ using two sub-ensembles in resonance with the cavity, while partly quenching the cavity to lower the cooperativity value. **b)** Same transmission measurement with $C_{\text{coll}} \approx 49$. A small bistable area is visible where the system evolves to different steady states depending on the history of the system in either the upper or lower branch. **c)** Same measurement as in a), with an increased cooperativity of $C_{\text{coll}} \approx 78$ (by using all four NV sub-ensembles in resonance with the cavity). The dashed curves are numerical solutions of Eq. (4.8). The dashed lines in b) show the asymptotic solutions in the limit of large and small drive amplitudes η. Two critical values of the input power, at which a phase transition between two stable branches occurs, are characterized by a saddle-node bifurcation and labeled as P^d_{crit} and P^u_{crit}. For all three cases, a sketch of the corresponding potential is also depicted, which shows the occurrence of either one or two stable solutions (red and blue solid circles) and one unstable solution (in figures b) and c)) (green solid circles) for a fixed value of the input power P_{ref}. Tunneling through the potential barrier does not occur in our case because of the large system size such that the system does not switch back and forth between the steady states in the bistable area. (Source: [103])

vanishes completely. We can, however, lower the cooperativity value intentionally by applying weak perpendicular magnetic fields for a short amount of time. This increases the cavity line-width to $\kappa/2\pi = 1.2\,\text{MHz}$ and consequently decreases the cooperativity of the system.

We start the experiment by probing the full transmission spectrum of the Hybrid system with two sub-ensembles in resonance with the cavity (and high quality factor) for different drive powers. We start with a low drive power, measure the transmission spectrum and then increase the power in a step-wise manner. The experimental data is shown in Fig. 4.3b), where we immediately spot the two regimes. For low drive powers we observe the normal mode splitting (indicated by the blue trace in front) which corresponds to the linear regime (or the description of the two coupled harmonic oscillators). For a certain threshold power (called P_{crit}) the system undergoes the transition to a decoupled system where the spin system is bleached ($\sigma_z^j \approx 0$) and the spins are uncoupled. The cavity starts to behave like an empty cavity again.

This nonlinear saturation behavior is the first step towards measuring bistability. However, whether it is observable or not is only determined by the systems cooperativity value (see previous section). In order to investigate that, we do not perform full transmission spectra but we drive the system only on resonance. We again start in the low drive regime and wait until a steady state of the transmission is reached. Afterwards we increase the drive power and repeat the experiment. For a critical drive power ($P^{\text{u}}_{\text{crit}}$), and if the cooperativity is large enough, the system undergoes a phase transition from the lower branch to the upper branch. Once we are deep in the strongly driven branch, we decrease the drive power again and measure the transmission intensity of the steady state.

Again, for a critical drive power ($P^{\text{d}}_{\text{crit}}$) the system undergoes the transition from the large drive power branch to the lower branch. If now $P^{\text{u}}_{\text{crit}} \neq P^{\text{d}}_{\text{crit}}$ we observe bistability which is only dependent on the value of the cooperativity.

The behavior of amplitude bistability can also be understood as a bifurcation, where close to the critical drive a saddle-node bifurcation occurs (for more details about saddle-node bifurcation see [104]). For input powers between $P^{\text{u}}_{\text{crit}}$ and $P^{\text{d}}_{\text{crit}}$ two attractors coexist and the system evolves to one of these two attractors depending if they are approached from below or above. These two attractors are connected – if the cooperativity is large enough – by a first order phase transition.

To define the critical cooperativity for which bistability exists, we take Eq. (4.13) and express η as a function of the cavity amplitude $|a|$ as

$$\eta = |a|\,\kappa \left(1 + \sum_{j=1}^{n} \frac{C_j}{1 + |a|^2 n_0^j}\right). \tag{4.16}$$

If the slope of this function $\eta(|a|)$ becomes negative for any value of the cavity amplitude, amplitude bistability is observed. Thus,

$$1 + \sum_{j=1}^{n} \frac{C_j\left(1 - |a|^2 n_0^j\right)}{\left(1 + |a|^2 n_0^j\right)^2} \leq 0, \tag{4.17}$$

is the necessary condition for observing bistable behavior. For a homogeneously broadened line-shape of the spin distribution this can be computed to be $C_{\text{coll}} \geq 8$, while for a q-Gaussian distribution only numerical results are available. These numerical

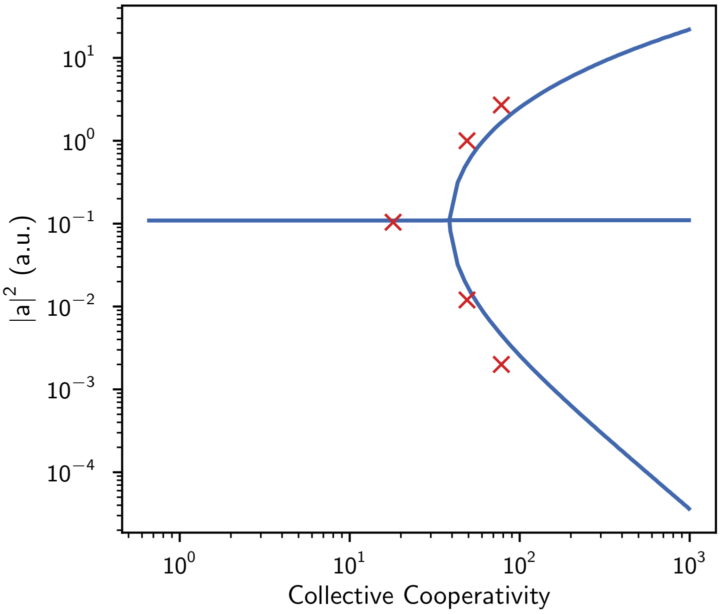

Figure 4.5: Simulated steady state solutions by solving Eq. (4.13) for the steady states for the reference power P_{ref}. For the simulation we use our system parameter and change the cooperativity by changing the collective coupling strength. We simulate with $n = 3001$ spins, a number sufficiently high enough to model our experiment. For a critical cooperativity of $C_{\text{coll}} = 42.2$ the system starts to show more than one steady state, with the middle one unstable and impossible to prepare in the experiment. Which of the other stable fix-points the system tends towards is determined by the history of the system. Shown are also the measured values for the cavity amplitude as in Fig. 4.4 for the three cooperativity values presented there. As it is obvious from the plot the occurrence of the saddle node-bifurcation is very well reproduced by the experimental data.

simulations show that, for a distribution as used for our experiment, the effect of bistability can be observed for a collective cooperativity (as defined in Eq. (4.9)) $C_{\text{coll}} \geq 42.2$, as shown in Fig. 4.5.

This is very well reproduced by the experiment as shown in Fig. 4.4 and Fig. 4.5 where for three different cooperativity values the measurements are shown. For a cooperativity value of $C_{\text{coll}} = 18$ – by coupling to two sub-ensembles and partly quenching the resonator – the cooperativity value is not large enough to show bistable behavior. For a cooperativity value of $C_{\text{coll}} = 49$ – by using two sub-ensembles and the unperturbed cavity – we see a small bistable area, where two stable solutions for one input power start to form. For a cooperativity value much larger than the critical cooperativity of $C_{\text{coll}} = 78$ – using all four sub-ensembles – we observe clear signs of amplitude bistability within a 2 dB range.

For these three cases we also plot the corresponding potential $\propto \mathrm{d}^2\eta/\mathrm{d}|a|^2$ (for the reference drive power P_{ref}) which shows that as soon as bistable behavior occurs more than one local minimum in the potential exists. In general a tunneling between these "stable" steady states should happen on its own driven by quantum fluctuations [105], however, due to our large number of spins these quantum fluctuations are extremely mitigated and a switching between these steady states does not occur in a measurable timescale.

4.1.3 Temporal Behavior of the Phase Transition

Steady state bistability is a well-known and well-understood effect. Many experiments have observed it using cold atom setups or trapped ions and it has led to numerous technological applications and is nowadays commonly used in optical switches [106]. Our implementation of amplitude bistability allows us to do something that has not been possible (or very limited [107, 108]) with other experiments so far. Our solid state hybrid quantum system shows properties, where the difference in dissipation rates are huge and ordered as $\kappa > \gamma_\perp \gg \gamma_\parallel$. This difference allows us to adiabatically eliminate the a and the σ_-^j variables, since in first order approximation the cavity amplitude $|a|$ and the polarization σ_-^j always are in a steady state (since their dynamics is much faster, due to the much larger rates) compared to the extremely slow behavior of the spin inversion σ_z^j, and follow the evolution of the σ_z^j variable adiabatically [109].

To understand the temporal evolution it is, therefore, only necessary to consider the time evolution of the spin inversion, which gives (see Eq. (2.49))

$$\begin{aligned} 0 &\simeq -\kappa a - i\Delta_c a + \sum_j g_j \sigma_-^j + \eta \\ 0 &\simeq -i\Delta^j \sigma_-^j + g_j a \sigma_z^j - \left(\gamma_\perp + \frac{\gamma_\parallel}{2}\right)\sigma_-^j \\ \dot{\sigma}_z^j &= -\gamma_\parallel \left(1 + \sigma_z^j\right) - 2g_j\left(\sigma_-^j a^\dagger + \sigma_+^j a\right). \end{aligned} \tag{4.18}$$

These equations capture the dynamics on a timescale where all the dynamics is defined by the slow evolution of the σ_z^j variable. All the fast dynamics that happens in the a and σ_-^j variables are not playing a role there anymore (such as coherent Rabi oscillations). In fact in this limit the evolution of both of these variables is enforced by the evolution of the σ_z^j variable, as a change in σ_z^j also changes both the cavity amplitude and the σ_-^j variable. This can be seen by reducing Eq. (4.18) to a set of two equations (again we omit Δ_c), one for the cavity amplitude one for the spin z-component, as

$$\begin{aligned} |a|^2 &= \frac{\eta^2}{\kappa^2 \left(1 - \sum_{j=1}^{n} C^j \sigma_z^j\right)^2}, \\ \dot{\sigma_z^j} &= -\gamma_{\|} \left(1 + \sigma_z^j\right) - \frac{\eta^2 \gamma_{\|} \sigma_z^j}{\kappa^2 n_j \left(1 - \sum_{j=1}^{n} C^j \sigma_z^j\right)^2}. \end{aligned} \tag{4.19}$$

This equations show that the cavity amplitude is enslaved by the evolution of the σ_z^j variable, and changes with it adiabatically.

Still, for this set of equations a closed polynomial expression for the cavity amplitude does not exist when including in-homogeneous broadening and many spins. In order to analyze the qualitative behavior of the collective spin ensemble we can, however, derive an equation for a giant spin in resonance with the cavity mode (i.e. a single spin that couples with a coupling strength $\sqrt{N}g$) which gives for the temporal evolution of the cavity amplitude (enforced by the evolution of the σ_z^j variable) a first-order differential equation of the form

$$\frac{d|a|^2}{dt} = -\frac{8C_{\text{coll}}\kappa^2|a|^5}{\eta} + 8C_{\text{coll}}\kappa|a|^4 - \frac{2\kappa\gamma_{\|}}{\eta}\left(1 + C_{\text{coll}}\right)|a|^3 + 2\gamma_{\|}|a|^2. \tag{4.20}$$

Using the same dimensionless parameters as before this reduces to the very simple equation

$$\frac{dx^2}{dt} = -2\gamma_{\|}\left(\frac{x^5}{y} - x^4 + \frac{x^3\left(1 + C_{\text{coll}}\right)}{y} - x^2\right). \tag{4.21}$$

This equation describes the temporal evolution of the cavity intensity for an arbitrary drive amplitude. The equation again does not have a simple analytic solution, but is rather straightforward to solve numerically. We immediately see that the whole evolution is globally scaled by the longitudinal relaxation rate – with the cooperativity being the only parameter affecting the “shape” of the evolution – which in the case of the NV center is orders of magnitude smaller than for other implementations of amplitude bistability. One should note that, even though this is only the equation for a single spin coupling to the cavity mode and such a nice closed form does not exist for an in-homogeneously broadened line-width, the results for a more complicated line-width show the same qualitative behavior.

In Fig. 4.6 we show the solution of this equation for a collective cooperativity value of $C = 128$ and a longitudinal relaxation rate of $\gamma_{\|} = 0.0001$. The initial state is such that the system is prepared in an initial state with $y \rightarrow \infty$, after which the temporal evolution of the system with a smaller drive value is studied. We observe, that close

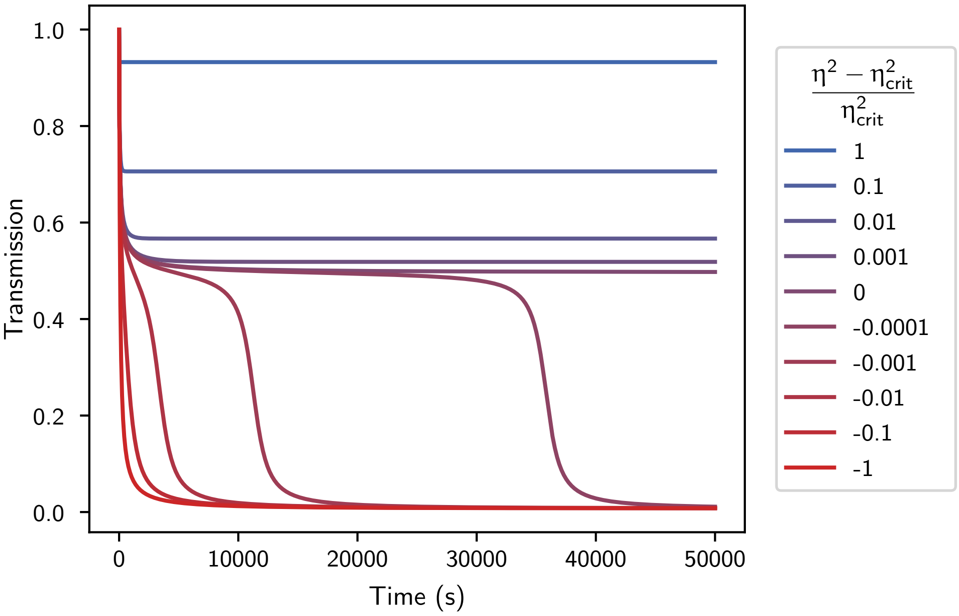

Figure 4.6: Simulated behavior for a quench measurements solving the differential equation Eq. (4.21) for a cooperativity of 128 and $\gamma_{||} = 0.0001$. As long as the system is driven harder than a critical drive power η^2_{crit} the system settles to a steady state in the upper branch. For drive powers lower than this critical drive the system relaxes to a steady state in the lower branch. Close to the critical drive the evolution becomes extremely slow and it takes an increasingly long time for the system to settle in a steady state.

to the critical drive value $y \to n_0$ the system takes increasingly long to settle to a steady state. For drive values, which are either much smaller or larger than the critical drive the system settles to a steady state much faster. The effect of extremely slow evolution close to the critical drive is known as “critical slowing down” or saddle-node “ghost” [110] and is usually hard to observe since the relative magnitudes of the decay rates have to have the proper ratios [107]. Note that instead of the cavity amplitude $\propto x$ we plot the transmission $|T| \propto x/y$, since it corresponds to what we measure in the experiment and gives the intuitive picture that the transmission approaches 1 for $y \to \infty$.

In our solid state system the extremely small longitudinal relaxation rate of the NV center allows to observe this critical slowing down on extremely long timescales, which allows to study the temporal evolution of the phase transition directly.

Experimental Implementation

In the experiment we perform this quench dynamics measurement with four sub-ensembles in resonance with the cavity. Quench refers to the abrupt switching of the drive power from very high drive powers to lower drive powers. We start the experiment by preparing the system in an initial state to $P_{\mathrm{in}} \gg P_{\mathrm{crit}}^{\mathrm{d}}$ for several minutes, such that the spin system is completely saturated and decoupled from the cavity. We then non-adiabatically switch to a lower "target" drive power, after which we look at the evolution of the transmission through the cavity.

The results are shown in Fig. 4.7 where we observe that close to the critical drive value $\eta_{\mathrm{in}}^2 \approx \eta_{\mathrm{crit}}^2$ (see Fig. 4.4) the system takes extremely long to reach a steady state. When driven far away from the critical drive value either in the strongly or the weakly driven branch the system on the other hand settles to a steady state rather quickly. If the drive is stronger than the critical drive it settles in the upper branch where the drive is stronger than any dissipation mechanisms in the system and a steady state with (mainly) saturated spins is reached.

For a drive much smaller than the critical drive, the combination of all dissipation rates dominate and the system loses energy faster than it is replenished by the drive, and thus settles in a steady state in the linear branch.

Very close to the critical drive, the drive power, putting energy back in the system, and the dissipation mechanisms are (almost) equal and opposite in effect, and, thus, the system cannot set in a steady state fast. This results in a very slow evolution towards the steady state of the system on a timescale of $\sim 40\,000\,\mathrm{s}$, known as "critical slowing down" in literature [107]. According to Eq. (4.20) close to the critical drive, the system becomes scale invariant and is characterized by an infinite correlation time [111]. Here the system shows a saddle-node bifurcation where the dynamics exhibits power law divergence. The timescale of this evolution is governed by the slowest decay rate in the system – in our case given by the longitudinal decay $\gamma_{\|}$.

In Fig. 4.7b) we also show the time derivative of the cavity amplitude, closer and closer to the critical drive value η_{crit}^2. We see that the derivative can approach zero arbitrarily close, the closer we approach the critical drive.

A nice thing about our implementation is that due to its slow dynamics (which makes it also tedious to measure) it allows us to extract rather easily the behavior of the phase transition close to the critical drive value. If we compute the time it takes for the system to undergo the phase transition from the upper to the lower branch (for powers smaller than the critical drive), we observe a simple power law divergence, as it is expected from such a phase transition. By using the ansatz $t_{\mathrm{switch}} \approx |\eta_{\mathrm{in}}^2 - \eta_{\mathrm{crit}}^2|^{-\alpha}$ – note that we define the switching time as the inverse of the smallest time derivative for

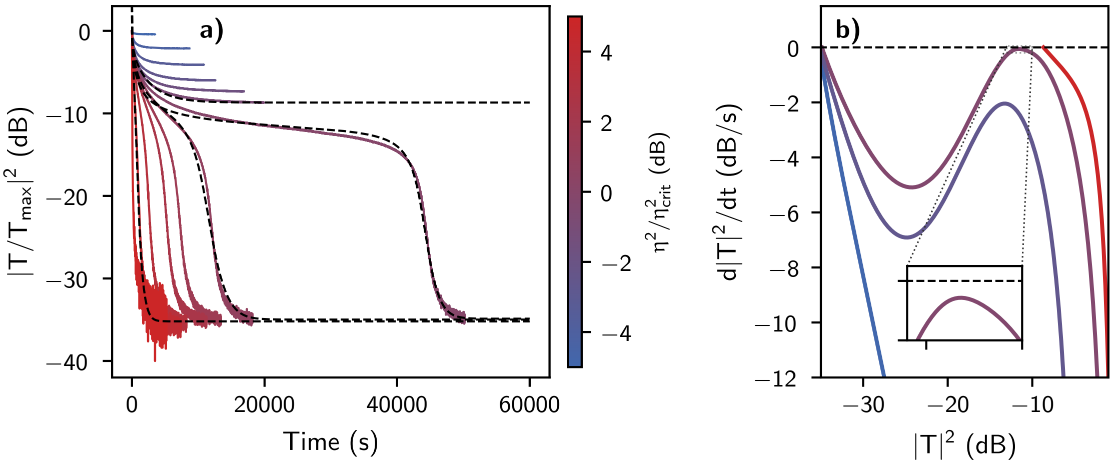

Figure 4.7: **a)** Quench dynamics of the high cooperativity $C_{\text{coll}} \approx 78$ configuration and an initial state far in the strong driving branch. The transmission $|\mathrm{T}/\mathrm{T}_{\max}|^2$ is plotted over time for different drive intensities where the time to reach a steady state strongly depends on the input intensity. For drive intensities larger than a critical drive value η_{crit} (defined as the power where the system undergoes the phase transition from the upper to the lower branch, the spin system remains saturated and sets into a state on the upper branch, whereas in the opposite case, the system evolves into a steady state on the lower branch. Close to the critical drive this time scale is extremely prolonged and approaches 4×10^4 s. The dashed lines correspond to full numerical simulations predicted from solving Eq. (4.18). The similarity to Fig. 4.6 is immediately apparent. **b)** The numerically calculated time derivative of the transmission through the cavity when doing a quench measurement as in a). The further away from the critical drive (either to high or too low), the faster the system evolves to a steady state. Close to the critical drive (small inset) the system can take arbitrarily long to reach a steady state, and the evolution becomes extremely slow. (Source [103])

a given curve – we observe a critical exponent of $\alpha = 1.2 \pm 0.04$ (see Fig. 4.8).

The value for the measured critical exponent depends on the precise structure of the so-called normal form (given for a system without in-homogeneous broadening by Eq. (4.20)). For the case without in-homogeneous broadening it is pretty straightforward to see that the critical exponent should be given by $\alpha = 1$. If we, however, include in-homogeneous broadening and solve Eq. (4.18) numerically, we observe excellent agreement between theory and experiment.

Therefore, this experiment is the first of its kind that really allows to study the dynamics of the bistable phase transition in a regime not accessible before, and a critical slowing down on a timescale not observable before, and gives the opportunity to study the nature of the occurring phase transition.

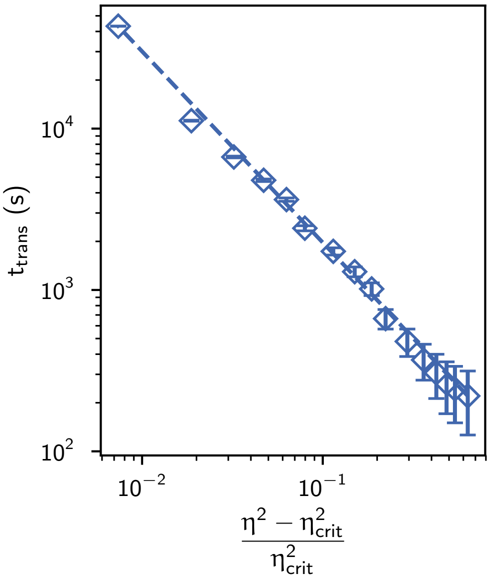

Figure 4.8: Time it takes for the system to undergo the phase transition from the strongly driven branch to the lower branch. We define the switching time (t_{trans}) as the inverse of the smallest gradient for a given curve extracted from Fig. 4.7. Close to the critical drive, the switching time diverges, and the time to reach a steady becomes arbitrarily long. The dashed blue line is a fitting function of the form $t_{\mathrm{trans}} \approx |\eta^2 - \eta^2_{\mathrm{crit}}|^\alpha$ with $\alpha = 1.20 \pm 0.04$.

4.1.4 Outlook and Discussion

To summarize, we have shown how to implement a first non-linear experiment in cavity QED based on driving the system strong enough to break the description of two coupled harmonic oscillators. The spin system saturates and decouples from the cavity mode. By measuring the steady state behavior of the system we saw that changing the cooperativity value, changes the occurrence of a bistable region – a regime where the hybrid system shows, depending on its history, more than one stable solution. The occuring phase transition also allows us to set-up our system to switch between the linear and non-linear regime.

Due to its peculiar ordering of the decay rates we then showed that this allows us to use adiabatic elimination to also explain the temporal behavior of this occurring phase transition in a regime not easily accessible. This allows us to extract a critical exponent of the phase transition, and show that it exhibits a power law divergence close to the critical drive value.

This experiment is a first experiment to better understand the non-linear behavior of such hybrid systems, and paves the way towards quantum technological applications, such as microwave isolators or microwave switches, which all rely on these type of non-linear effects.

4.2 Superradiance – Collective Non-linear Behavior

Parts of this chapter are based on:

- **“Superradiant emission from colour centres in diamond”**
  Andreas Angerer, Kirill Streltsov, Thomas Astner, Stefan Putz, Hitoshi Sumiya, Shinobu Onoda, Junichi Isoya, William J. Munro, Kae Nemoto, Jörg Schmiedmayer, Johannes Majer
  Nature Physics 14, 1168–1172 (2018)

In the previous sections I have presented a first experiment showing a non-linear effect in cavity QED. It is fundamentally based on saturating the spin system such that the coupling of the spins to the cavity mode becomes zero. This means that when driving the system, we lose all the coherence and operate between two states where the spins are either all in the ground state (and by definition a phase or coherence is not defined there) or in a state where all the coherence is gone, because the system has been driven much longer than dephasing and decoherence times.

This is, however, not the only way to show and study non-linear effects in our system. An inverted spin system is fundamentally something that is different from a harmonic oscillator (in a sense it is actually exactly what a harmonic oscillator isn’t, since a harmonic oscillator cannot be in its “excited” state).

The non-linearity of an excited spin ensemble becomes apparent in an effect known as superradiance. Superradiance is the effect where an ensemble of excited spins decay fundamentally different than a single spin, as it was pointed out by Dicke in 1954 [50]. Dicke introduced this idea with two neutrons that are close to each other with a distance smaller than the radiation wavelength but still far enough from each other so that dipole-dipole interaction is negligible.

A single neutron that is prepared in its excited state (for example the higher energy spin state in a magnetic field) decays with a rate that corresponds to its spontaneous emission rate. The naive assumption would be that putting a second neutron which is in its ground state would not alter the radiation process of the excited neutron. However, this assumption is not correct. With one of the neutrons being in the excited state and the other one in the ground state, the probability of finding one neutron in the excited state tends towards 1/2 and not 0, and after $t \to \infty$ we still find a probability of 1/2 for one of the two neutrons excited (even though it is impossible to say which one is excited and which one de-excited).

The difference in the radiation process stems from the fact that an arrangement of two neutrons with one of them excited and the other one in its ground state can be either a singlet or triplet state, like

$$\begin{aligned}
|\Psi\rangle_{\text{triplet}} &= \frac{1}{\sqrt{2}}\left(|\uparrow\downarrow\rangle + |\downarrow\uparrow\rangle\right) \\
|\Psi\rangle_{\text{singlet}} &= \frac{1}{\sqrt{2}}\left(|\uparrow\downarrow\rangle - |\downarrow\uparrow\rangle\right).
\end{aligned} \tag{4.22}$$

As we already derived in Section 2.2.4 only the triplet state couples to the electromagnetic field of radiation and can therefore decay; the other one is usually referred to as "dark" state and cannot decay. Since both of these configurations are equally likely, the chance to find both neutrons in their ground state tends towards 1/2 for time goes to infinity. From that we immediately see that the radiation process of a single emitter is fundamentally different from that of an ensemble of emitters that are placed in a distance smaller than the wavelength of the emitted radiation.

Superradiance is now the case when the system is prepared in the symmetric triplet state, where it turns out that the spins decay with a rate four times as large as a single spin – hence the name superradiance.

4.2.1 Superradiance – An Interference Effect

Even though Eq. (4.22) suggests that the effect observed is of quantum mechanical nature, superradiance can actually be understood in terms of classical fields and is fundamentally a "classical" interference effect. The difference between the singlet and the triplet state in the previous example is obviously the phase relation between spin one and spin two. In the case of the singlet, the emitted wave would interfere destructively (their phase difference is π) and therefore no light is emitted, thus, the emitter cannot get de-excited by emitting a photon. For the case of the triplet state the phase difference between the two particles is zero and the light emitted interferes constructively.

This means that if the phase of the emitters during decay is and stays zero, the amplitude adds up and, since the intensity is the proportional to the square of the amplitude, the emitted photon number scales as[1] N^2. If on the other hand we prepare the ensemble in a state where the emitted radiation interferes destructively, the spins can not decay at all (sometimes called "sub-radiance", even though everyone uses these notions a bit differently)

There are several states that show this constructive interference: If the permutation of two particles does not change the sign of the wave function the phase between the emitters has to be zero. If there is no mechanism to change the symmetry of the wave function during decay this coherence is maintained and superradiance unavoidably occurs.

---

[1] This is similar to how a laser works. Coherence is maintained through the common radiation field which preserves this amplification. This is, however, significantly different to superradiance, where the coherence is maintained by the spins themselves

States that are obviously symmetric states are the Dicke states as introduced in Section 2.2.4. They are symmetric under permutations of two spins, and therefore decay superradiantly. As such a cavity QED system is the perfect system to study superradiance as its coupling term does not allow to leave this symmetric subspace. This is the same as saying, that when starting with an excited spin system (which is the uppermost Dicke state), and considering only the interaction with the cavity, we can never leave this symmetric subspace of Dicke states and superradiance will occur.

But the Dicke states are not the only states that exhibit the necessary symmetry to observe superradiance. Also the spin coherent state – which is the state we obtain in the spin system when driving the cavity with a coherent drive – has a phase of zero between its emitters and, thus, shows superradiance[1]:

$$|\psi\rangle = \prod_{i=1}^{N} \left(\cos\left(\frac{\theta}{2}\right) |{\downarrow}\rangle_i + i \sin\left(\frac{\theta}{2}\right) |{\uparrow}\rangle_i \right). \tag{4.23}$$

Here θ goes between 0 and π and gives the inclination of the coherent state from the ground state. To obtain this state we use the displacement operator for spins on the ground state and rotate them with an angle θ. This has the same effect as driving the spins with a coherent laser field, as this is equivalent to the time evolution operator for a spin (system) driven by a coherent drive:

$$|\psi\rangle = e^{i\theta S_x} |{\downarrow\downarrow}\dots{\downarrow}\rangle. \tag{4.24}$$

This state, even though not showing any entanglement as it is a product state, is symmetric under permutations of the spins, and therefore shows constructive interference i.e. superradiance[2]. All states that show constructive interference (i.e. a phase difference of zero for all times) show superradiance and entanglement is therefore not a necessary condition to observe it.

Let us now turn to the qualitative description: Classical Dicke superradiance with the typical N^2 scaling of the emitted radiation, only exists when the emitters are coupled to the vacuum mode (as it was introduced in Dicke's thought experiment), let us therefore neglect the cavity mode for now (for details how we solve the “problem” of the cavity mode in our experiment see Section 4.2.2).

---

[1] These states are in a sense the analogous extension of the coherent state as in introduced in Section 2.1.3. They are the most "classical" spin states, and are obtained by using an unitary displacement operator

[2] The excited spin state is both: a spin coherent state and the uppermost Dicke state

The Hamiltonian for N spins in vacuum is simply given by

$$H_{\text{vac}} = \hbar\omega_s \frac{S_z}{2}. \tag{4.25}$$

Here we only consider identical spins, but qualitatively the same can be derived with in-homogeneous broadening.

By again making a Master-equation approach, the only way to dissipate energy in this system is by spontaneous emission processes with a rate $\gamma_\parallel$ due to of vacuum fluctuations that happen by the coupling to the vacuum mode. This is often referred to as the natural T_1 time and fundamentally limited by Heisenbergs uncertainty relation. In addition we also consider decoherence processes through the transverse rate $\gamma_\perp$ (the whole derivation is very similar to the one done in Section 2.2.6), which destroy coherence but do not dissipate energy.

This then gives the equation of motion as

$$\dot{\rho} \;=\; -i\frac{\omega_s}{2}\left[S_z,\rho\right] \;+\; \gamma_\parallel\left(2S_-\rho S_+ - S_+S_-\rho - \rho S_+S_-\right) + \frac{\gamma_\perp}{2}\left(S_z\rho S_z - \rho\right). \tag{4.26}$$

For the inversion and the polarization we then obtain in the frame rotating with the spin

$$\begin{aligned} \langle \dot{S_z} \rangle &= -\,2\gamma_\parallel \langle S_+S_- \rangle \\ \langle \dot{S_-} \rangle &= -\,i\Delta_s \langle S_- \rangle - \left(\gamma_\perp + \frac{\gamma_\parallel}{2}\right)\langle S_- \rangle\,, \end{aligned} \tag{4.27}$$

also known as optical Bloch equations. Due to conservation of energy a loss in inversion has to correspond to the emission of photons into the vacuum mode, thus, $\langle S_+S_- \rangle \propto \langle n \rangle$ [112] and:

$$I_{\text{em}} = I_0 \langle S_+S_- \rangle\,, \tag{4.28}$$

with the emitted radiation as I_{em} and some reference intensity I_0.

For a symmetric state (we will use the Dicke states here because they are the easiest to compute, but the calculation would be analogous for any other symmetric states with phase difference of zero), this straightforwardly computes to

$$I_{\text{em}} = I_0 \langle S, m_s | \, S_+S_- \, | S, m_s \rangle = I_0(S+m_s)(S-m_s+1). \tag{4.29}$$

We immediately see that for an excited spin system ($S = N/2, m_s = N/2$), this is proportional to the number of spins N and equivalent to each spin decaying with its individual decay rate. If, however, we consider the symmetric state with $\langle S_z\rangle$-projection $m_s = 0$, correlations (i.e. coherence) have build up within the spin system and the emission intensity becomes proportional to N^2. This non-linear scaling of the emitted radiation intensity is the characteristic behavior of superradiance.

Not only the scaling of the emitted radiation is of interest but also the shape and dynamics of this burst of photons, which can be extracted from Eq. (4.27). For an arbitrary Dicke state the first Bloch equation becomes ($S = N/2$)

$$\langle \dot{S_z}\rangle = -2\gamma_{\|}\left(\frac{N}{2} + \langle S_z\rangle\right)\left(\frac{N}{2} - \langle S_z\rangle + 1\right), \tag{4.30}$$

which can be solved for the condition $\langle S_z\rangle(t_\mathrm{d}) = 0$ (i.e. for a certain delay time t_d the system has $\langle S_z\rangle$-component zero where correlations are largest) as

$$\langle S_z\rangle = -\frac{N}{2}\tanh\left(\gamma_{\|}N\left(t - t_\mathrm{d}\right)\right), \tag{4.31}$$

when assuming $N \gg 1$. Since $\langle \dot{S_z}\rangle \propto \langle a^\dagger a\rangle$ we get

$$I \propto -\frac{\mathrm{d}S_z}{\mathrm{d}t} = \frac{N^2}{2}\operatorname{sech}^2\left(\gamma_{\|}N\left(t - t_\mathrm{d}\right)\right), \tag{4.32}$$

with a FWHM of the photon burst duration of

$$\tau_\mathrm{sr} = \frac{2\cosh^{-1}\left(\sqrt{2}\right)}{N}. \tag{4.33}$$

For emitters that emit photons independently from each other we would assume a rate $\Gamma_s = 2\gamma_t N$, i.e. a rate that is dependent on the number of emitters, but scales linearly. In the case of superradiance however, the rate changes such that cascading down the Dicke ladder the sth $= (S - m_s)$th spin decays with a rate (as derived before)

$$\Gamma_s = \Gamma_{m_s \to m_s - 1} = 2\gamma_{\|}\left(S + m_s\right)\left(S - m_s + 1\right). \tag{4.34}$$

For the beginning of the decay this can be “linearized” to [48]

$$\Gamma_s = 2\gamma_{\|}Ns. \tag{4.35}$$

This means that the first spin decays with a rate $2\gamma_{\|}N$ the second with a rate $4\gamma_{\|}N$ and so on. The average time interval of this process can then be approximated by summing the inverse of these decay rates

$$t_{\mathrm{d}} \sim \frac{1}{2N\gamma_{\parallel}}\left(1+\frac{1}{2}+\frac{1}{3}+\ldots+\frac{1}{N}\right)=\frac{\log(N)}{2N\gamma_{\parallel}}. \tag{4.36}$$

4.2.2 Operating in the "Fast" Cavity Limit of Cavity QED

As shown in the previous section, superradiance is an effect that shows up when coupling an ensemble of emitters to the vacuum mode of radiation. This poses a problem though since the initial assumption of emitters that are close enough to share correlations in their wavefunctions, but still are far enough from each other in order to retain their mutual coherence is problematic. In fact, as it turns out, dipole-dipole interaction between emitters is always just large enough to destroy the necessary coherence to observe the effect [48] and "pure" superradiance in a cloud of atoms is impossible to observe. This makes sense intuitively as the coupling between emitters has the same nature as the coupling of an emitter to the electromagnetic vacuum which leads to an energy shift. This can be seen from Eq. (4.27), where a dipole dipole interaction leads to a slight detuning, which changes the dynamics considerably and destroys the non-linear scaling.

As we have seen in the previous section, the operator that is related to the coherence in the system is the two spin operator which we can write as

$$\langle S_+S_-\rangle = \sum_{i}^{N}\left\langle \sigma_+^i\sigma_-^i\right\rangle + \sum_{i\neq j}^{N}\left\langle \sigma_+^i\sigma_-^j\right\rangle . \tag{4.37}$$

As obvious from the second Bloch equation, a detuning (as it would originate from dipole-dipole interaction) leads to a pick up of phase. For the case of dipole-dipole interaction (or in-homogeneous broadening in general) this is random for each spin, and the second term in Eq. (4.37) averages to zero. Only the first term, which is proportional to the number of emitters, remains.

However, the requirement for superradiance is that the relative phase of emitters is zero (or a multiple of 2π). Clever configurations in optical lattices [113–115] or other special geometries (1D BEC [116]) allow to observe superradiance in these type of systems with the atoms much further apart than the wavelength of the emitted radiation, where dipole-dipole interaction between emitters is indeed negligible.

A different approach is to use a cavity, where the coupling to the mode of radiation is enhanced by the Purcell factor (an effect I will explain later), while the dipolar interaction stays the same [117]. Nevertheless, in order to resemble the conditions in vacuum one has to use a “fast” (or “bad”) cavity where the cavity line-width is much larger than the dynamics that occur in the system [118, 119]. That allows to resemble a situation where the effect is similar to the case in vacuum with the difference that the coupling to the mode is enhanced.

The starting point for the “fast” cavity description is the Hamiltonian as derived in Eq. (2.43), and assuming homogeneous coupling (see Section 4.2.3)

$$H = \hbar\Delta_c a^\dagger a + \frac{\hbar}{2}\sum_{i=1}^{N}\Delta_s^i\sigma_z^i + i\hbar g\sum_{i=1}^{N}(\hat{\sigma}_-^i a^\dagger - \sigma_+^i a) + i\hbar\eta(a^\dagger - a). \tag{4.38}$$

As derived earlier this gives rise to an equation of motion for the cavity amplitude as

$$\dot{a} = -\frac{\kappa}{2}a - i\Delta_c a + g\sum_j \sigma_-^j + \eta. \tag{4.39}$$

Note that here we use κ as the FWHM (thus the additional factor of one half), as it allows easier comparison of quantities in the fast cavity limit.

For the limit of $\kappa \gg g\sqrt{N}$, we can make the ansatz $\dot{a} = 0$ since the presence of the spins (i.e. the coupling) does not alter the cavity amplitude which remain unchanged by the presence of the spin system.

The limit of $\kappa \gg g\sqrt{N}$ is often called the “bad” cavity limit, but I would like to make distinction between a “bad” and a “fast” cavity: A cavity that loses energy very quickly through internal losses is indeed a “bad” cavity (and not what is generally desired), whereas a “fast” cavity is determined through a strong coupling to the environment. This allows to effectively put photons into the system and get them out, which is fundamentally different to a “bad” cavity, where the photons are lost through ohmic losses (i.e. heat) or scattering out of the mode. This means that the limit for a “fast” cavity really is (see Section 3.1.4) $\kappa_{\text{ext}} \gg \kappa_{\text{int}}, g\sqrt{N}$.

If we also assume the pump tone to be in resonance with the cavity mode ($\Delta_c = 0$), we can extract

$$a = \frac{2g}{\kappa}\sum_j \sigma_-^j + \frac{2\eta}{\kappa} \tag{4.40}$$

and the Hamiltonian changes to the form

$$H_{\text{at}} = \frac{\hbar}{2}\sum_{j=1}^{N}\Delta_{\text{s}}^j\sigma_z^j - 2\hbar\frac{g\eta}{\kappa}\sum_{j=1}^{N}\left(\sigma_+^j + \sigma_-^j\right). \tag{4.41}$$

Again using the Lindblad master equation as in the derivation of Eq. (2.49), introducing loss channels for the cavity mode and the spins we derive the equations of motion for the cavity spin system in the fast cavity limit. Note that we also express the Lindblad superoperator for the cavity losses in terms of atomic operators as

$$\mathcal{L}_{\mathrm{cav}} = \frac{2g^2}{\kappa} \sum_{j,k}^{N} \left(2\sigma_-^j \rho \sigma_+^k - \sigma_+^j \sigma_-^k \rho - \rho \sigma_+^j \sigma_-^k \right) . \tag{4.42}$$

This then finally gives the equations of motion describing the dynamics of our system as

$$\langle \dot{S}_z \rangle = -\frac{4g\eta}{\kappa} \langle S_y \rangle - \gamma_{\|} \left(\langle S_z \rangle + \frac{N}{2} \right) - \frac{4g^2}{\kappa} \langle S_+ S_- \rangle . \tag{4.43}$$

Here the collective operator $S_y = i \sum (\sigma_- - \sigma_+)$.

This equations shows very strong resemblance to the equation derived in vacuum as in Eq. (4.27). We see that instead of spontaneous emission into the vacuum mode ($\gamma_{\|}$) the correlations enhance the so called Purcell factor $4g^2/\kappa$. The Purcell factor describes how much stronger the coupling of the spin to a cavity mode is compared to the coupling to the vacuum mode of the electromagnetic field.

Even though the coupling to the mode is enhanced by many orders of magnitude, for a single spin this effect is still very hard to observe [120], as the value in our case is as small as $\Gamma_{\mathrm{Purcell}} = 10^{-10}$. However, due to the N^2 enhancement of $\langle S_+ S_- \rangle$ and the huge number of spin ($\sim 10^{16}$) in our experiment, the effect becomes visible.

The longitudinal relaxation $\gamma_{\|}$ in our case is not given by spontaneous emission into the vacuum mode, but by relaxation due to phonon interaction with the solid state environment and is small enough to be neglected [53]. That leaves the first term, which describes the evolution of the spin system due to a coherent drive. This term allows us to use a coherent drive to achieve inversion of our spin system after which we set $\eta = 0$ and only consider the undriven evolution of the spins.

4.2.3 Experimental Implementation

Having derived the theoretical framework, let us now turn to the experimental implementation. For this experiment we are using a 3D Lumped element resonator (as introduced in Section 3.1.3) that allows us to coherently drive all the spins and prepare states with almost full inversion of all spins. We estimate the single spin coupling rate to be $\approx 72\,\mathrm{mHz}$ which with the number of spins of $\approx 10^{15}$ changes the coupling from 3.1 to 6.2 MHz depending on the number of sub-ensembles coupled (see Section 3.2.1). In order to increase the number of photons in the cavity – a necessary requirement to perform fast spin inversion – we operate the cavity in the largely over-coupled regime

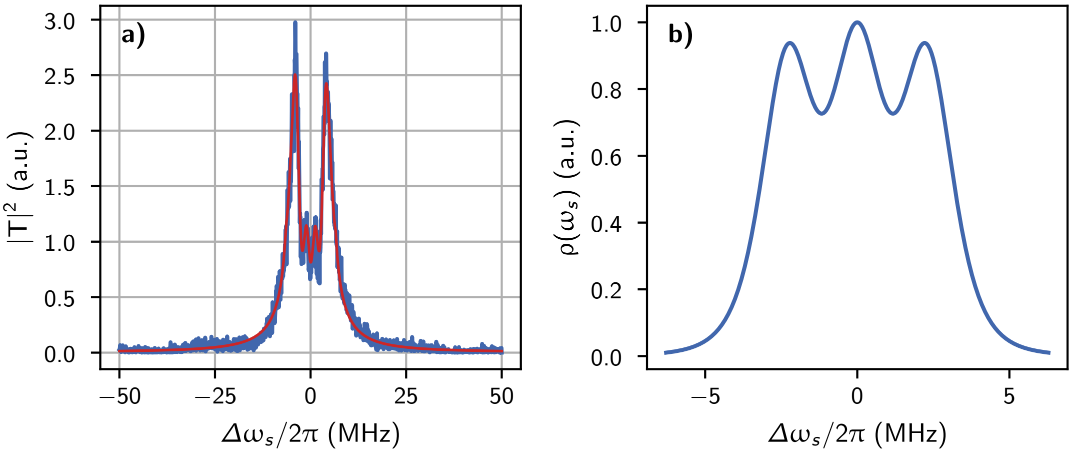

Figure 4.9: a) Measured transmission spectrum for the case of one sub-ensemble in resonance with the cavity mode. We can fit the measured spectrum with the steady state solution of Eq. (2.49) (orange curve), which allows to reconstruct the coupling strength of 3.1 MHz and the spin density in **b)**, as well as all the other parameters such as the spin line-width and q-value. The cavity line-width we measure separately with the spins far detuned. We can also clearly observe the hyper-fine splitting of 2.8 MHz which becomes visible because of the small broadening of the individual lines. Note that in order to extract the coupling and spin line-width more precisely, this plot was done with a "good" cavity with $Q = 1200$, which puts the cavity far from the "fast" cavity limit. In order to increase the cavity line-width afterwards we only increased the input coupling, which in turn is not changing the coupling strength or the spin properties.

with the input coupling much larger than the output coupling ($\kappa_1 \gg \kappa_2 \gg \kappa_{\text{int}}$; i.e. fast cavity limit).

Since the total decay rate of the cavity is given by the sum $\kappa_1 + \kappa_2 + \kappa_{\text{int}}$, this also means that the cavity decay rate $\kappa_{\text{tot}} \approx \kappa_2 = 13.6$ MHz is larger than the collective coupling and the in-homogeneous broadening of the spin distribution. This allows to assume that we are working in the fast cavity regime (see Section 4.2.2).

The sample is a type-Ib high-pressure, high-temperature diamond crystal with an initial nitrogen concentration of 50 ppm. To create lattice vacancies, the sample is irradiated with electrons of energy 2 MeV at 800 °C and is subsequently annealed multiple times at 1000 °C. The total electron dose was $5.6 \times 10^{18}\,\text{cm}^{-2}$. This gives a total NV density of 13 ppm and an in-homogeneously broadened line-width of $\gamma_{\text{inh}} = 4.7$ MHz (see Fig. 4.9) (FWHM). This value is fundamentally limited by the hyperfine coupling to the nuclear spin of nitrogen (2.3 MHz). The small spectral broadening allows us to increase our signal-to-noise ratio and number of photons emitted during the superradiant decay, since coherence is maintained more effectively.

The longitudinal decay of the spin ensemble is mediated by phonon-phonon interactions [53] and can be as small as $3 \times 10^{-5}\,\mathrm{s}^{-1}$ but is still orders of magnitude larger than the single spin Purcell factor which on resonance computes to

$$\Gamma_{\mathrm{P}} = 4\frac{g^2}{\kappa} = 2\pi \cdot 7.5 \times 10^{-10}\,\mathrm{Hz}. \tag{4.44}$$

As introduced in Section 3.1.3 an optical fiber grants us additional access to measure the spin projection of our NV centers and observe the decaying spins directly.

4.2.4 Thermal Occupation

In order to reduce the time that is needed to perform a π-pulse – this is important because the shorter the pulse the less dephasing and decoherence effects have an influence during drive – we remove all the attenuators going from room temperature down to 30 mK. The result of that is, that the cavity mode is effectively at a temperature close to 300 K, which naively means that the spin system should be affected and be at the same temperature in a thermal state as well.

Looking closer at numbers though this assumption is misleading: For a thermal (steady) state the number of excitations in the cavity mode can be computed by Bose statistics [84, 85] as

$$\langle n \rangle_{\mathrm{therm}} = \frac{1}{e^{\frac{\hbar\omega_c}{k_B T}} - 1}. \tag{4.45}$$

Even for room temperature at 300 K this computes to the very small number of $\langle n \rangle_{\mathrm{therm}} \approx 2000$, which gives a ratio of $\langle n \rangle_{\mathrm{therm}} / N_{\mathrm{spins}} \approx 10^{-12}$, and, therefore, can be neglected compared to the number of spins[1]. This can be seen in Fig. 4.10 where we show the thermal occupation of the cavity mode versus the temperature, which shows that for a cavity resonance frequency of 3 GHz the influence of thermal photons in the cavity mode is negligible.

4.2.5 Optical Measurements

For an experiment that measures the enhanced decay of the spins it is imperative that a direct measurement of the spins is possible. As laid out in Section 3.3 this is

---

[1] That is also the reason why strong coupling can be shown at room temperature, if the number of spins coupled to the cavity mode is large enough [121], since the thermal occupation at room temperature does not change the spin state considerably

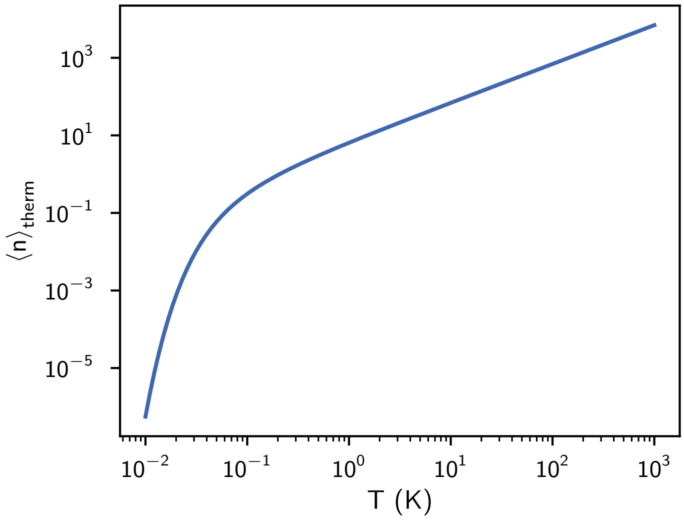

Figure 4.10: Thermal cavity occupation over temperature and a cavity frequency of 3 GHz. For low temperatures the thermal population is negligible, but even for higher temperatures the thermal population is as small as 2000 photons which is 12 orders of magnitude smaller than the number of spins in the ensemble.

possible in our experiment by using an optical multi-mode fiber that both sends green light to the sample using a high bandwidth laser-diode and collects the scattered red light which is then separated by a dichroic mirror and measured using an avalanche photo-detector.

In Fig. 4.11b) it is depicted how this is done in the experiment. We drill a hole in one side of the resonator (this doesn't change the Q-factor of the resonator much, since the current density is small there) and glue the fiber onto the sample directly using super-glue.

In Fig. 4.11a) we see two measured fluorescence curves, one before an inversion pulse (high fluorescence) and one after an inversion pulse. The difference in fluorescence gives us a direct measurement for the inversion of our spin system and allows us to monitor the evolution of the spin after inversion.

4.2.6 Nonlinear Scaling and Enhanced Decay

We start the measurements by applying 50 ns microwave pulses to the sample with a certain power level, and look at the response of the system. By repeating this measurement after all spins have relaxed back into their ground state – either due to

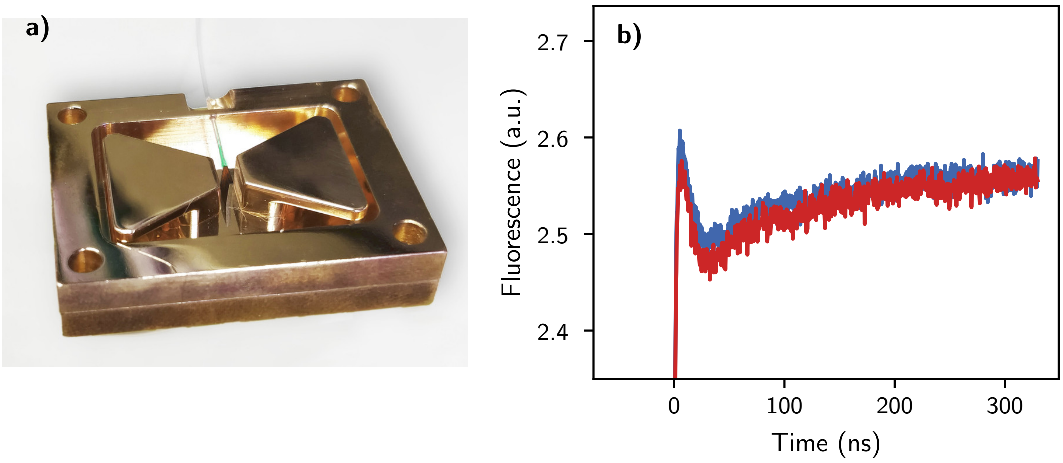

Figure 4.11: **a)** Photograph of the cavity with a fiber glued onto the diamond sample. The diamond is illuminated with green laser light and the scattered red light is collected through the same fiber. **b)** The difference in fluorescence for the spins in the ground state (blue curve) before any microwave pulse was played, compared to the fluorescence after maximum inversion pulse was played (red curve). The measurement is averaged 500 times. The small difference in fluorescence makes it very hard to measure the population difference.

the enhanced decay or longitudinal relaxation for the remaining incoherent inversion – with increased power, at some point we reach the point where the spin ensemble is maximally inverted.

The state we produce by the coherent drive of the cavity, can be computed from Eq. (4.41), where the time evolution operator (assuming no in-homogeneous broadening for simplicity) applied to the ground states produces states like:

$$|\psi\rangle = U(t)\,|\downarrow\downarrow \dots \downarrow\rangle = e^{-\frac{i}{\hbar}Ht}\,|\downarrow\downarrow \dots \downarrow\rangle\,. \tag{4.46}$$

With the Hamiltonian from Eq. (4.41) this generates the aforementioned spin coherent states

$$|\psi\rangle = \prod_{l=1}^{N}\left(\cos\left(t\frac{2g\eta}{\kappa}\right)|\downarrow\rangle_l + i\sin\left(t\frac{2g\eta}{\kappa}\right)|\uparrow\rangle_l\right), \tag{4.47}$$

with the value of $\theta/2 = 2tg\eta/\kappa$ defining the inclination "angle". This state, as we showed in Section 4.2.1, is a fully symmetric state, and thus shows superradiance.

If the angle θ is now large enough by increasing the drive amplitude η (for a fixed duration t) we enter the previously defined non-linear regime and the correlations become strong enough such that the emission of radiation gets enhanced.

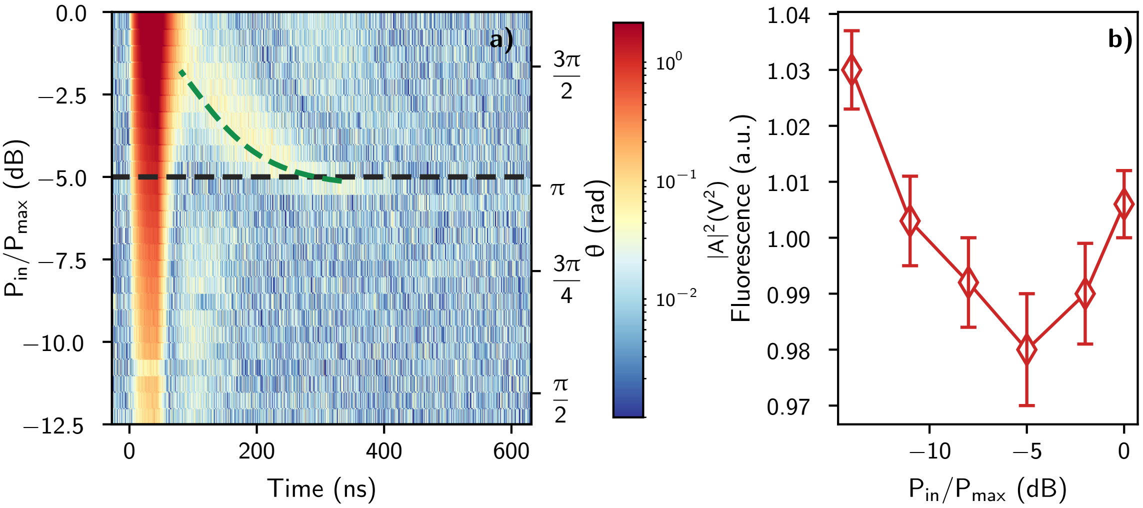

Figure 4.12: a) Intra-cavity intensity of a measurement where we apply a 50 ns MW pulse and continuously increase the power while monitoring the emitted radiation with three sub-ensembles in resonance with the cavity. At a power level of ≈ 5 dB attenuation of the maximum power available for the experiment (this is indicated by the black dashed line) we observe maximum inversion and see a (relatively strong) pulse being emitted from the cavity (the delay of this pulse is indicated by the green dashed line and is fitted according to Eq. (4.51)). For higher powers the delay of the burst becomes smaller, since excess photons in the cavity lead to stimulated emission (source [89]). **b)** Fluorescence measured directly after the MW pulse ended, to confirm that the inversion is maximum for an input power of −5 dB, which corresponds to the lowest fluorescence.

For small drive powers not much happens. The spin system gets partly inverted but the inversion is not large enough that correlations can build up and the spins decay back into their ground state without emitting a significant amount of radiation. When increasing the power of the drive pulse, we start to enter the non-linear regime where correlations leads to an increased emission of photons.

This can be seen in Fig. 4.12 where by increasing the power, we see more and more additional radiation after the drive pulse is turned off. This we can attribute to constructive interference.

For a certain threshold amplitude η the state in Eq. (4.23) becomes fully inverted (i.e. $\theta = \pi$; roughly at -5 dB in Fig. 4.12). This is the same situation as derived in Section 4.2.1 from which we can deduce the delay and shape of the superradiant burst. If we further increase the drive power, we "over-rotate" our spin system (i.e. inclination angles $\theta > \pi$, which has the effect that the delay becomes shorter again. Note, that the amplitude of the emitted burst does not change in this case, since the amount of coherence (or correlations) is maximum at the equator, which means that as long as we don't over-rotate with an angle $\theta > 3\pi/2$ we don't change the amount of coherence in the decaying spin system

We can plug the definition of the spin coherent state into Eq. (4.43) (omitting $\gamma_{\|}$ and setting $\eta = 0$), and get

$$\langle \dot{S_z} \rangle = -\frac{4g^2}{\kappa}\left(\frac{N^2}{4} + \frac{N}{4} + \langle S_z \rangle - \langle S_z \rangle^2 + \frac{\langle S_z \rangle^2}{N}\right) \tag{4.48}$$

which again shows the N^2 dependence.

The expectation value for the $\langle S_z \rangle$ component of the spin for a spin coherent state can be computed as

$$\langle S_z \rangle = -\frac{N}{2}\cos\left(\theta(t)\right), \tag{4.49}$$

which allows to solve the differential equation analytically with the initial state $\langle S_z(0) \rangle = -N/2\cos(\theta)$, and then solved for t and $\langle S_z \rangle = 0$ in order to determine the delay of the emitted pulse (as the emission is maximum at the equator of the Bloch sphere). This gives

$$t_{\mathrm{delay}} = \frac{\kappa}{4g^2N}\log\left(-\frac{(N+1)\left(\cos(\theta)-1\right)}{N\cos(\theta) - \cos(\theta) + N + 1}\right), \tag{4.50}$$

which for $N \gg 1$ simplifies to

$$t_{\mathrm{delay}} \approx \frac{\kappa}{4g^2N}\log\left(\tan^2\left(\frac{\theta}{2}\right)\right), \tag{4.51}$$

which can be seen in Fig. 4.12 as the green dashed line. The line-shape and dynamics of the spin decay can be obtained from this solution as

$$\langle S_z \rangle = -\frac{N}{2}\tanh\left(\frac{2g^2N}{\kappa}(t - t_{\mathrm{d}})\right), \tag{4.52}$$

with the intensity of the emitted radiation as (note the nonlinear scaling)

$$I \propto -\frac{\mathrm{d}S_z}{\mathrm{d}t} = \frac{g^2N^2}{\kappa}\operatorname{sech}^2\left(\frac{2g^2N}{\kappa}(t - t_{\mathrm{d}})\right) \tag{4.53}$$

and a FWHM for the burst duration of

$$\tau_{\mathrm{sr}} = \frac{\kappa\cosh^{-1}(\sqrt{2})}{Ng^2}. \tag{4.54}$$

Even though these equations model the maximum delay for full inversion and can explain the width of the emitted pulses reasonably well, naively we would assume a symmetric response around full inversion no matter if we under-rotate or over-rotate the spins. As long as we are dealing with a perfect system this assumption is true, no matter if we drive the system to a state with angle $\theta - \alpha = \pi$ or $\theta + \alpha = \pi$ (with $0 \leq \alpha \leq \pi/2$) the response of the system is the same. This can be seen in Fig. 4.13b) where a same powerscan is simulated without in-homogeneous broadening and decoherence. We observe maximum delay for a fully inverted spin system and the delay and the amplitude of the emitted pulse is symmetric for cases where we under- or over-rotate with respect to full inversion.

As soon as we include decoherence and/or dephasing, this symmetry vanishes and it seems that coherence is lost for states with an inclination angle smaller than π (see Fig. 4.13a)). The reason for that can be explained by looking at Eq. (2.49) which shows that inhomogeneous broadening (i.e. a detuning) and decoherence only has an effect on the dynamics if the $\langle S_- \rangle$ value (often referred to as polarization) is not equal to zero. This means that a larger integrated $\langle S_- \rangle$ value leads to more decoherence which destroys the built-up correlations.

To understand why states with $\theta < \pi$ have a larger integrated $\langle S_- \rangle$ value, Fig. 4.14 compares the case of an in-homogeneously broadened ensemble that is driven into a state with $\theta = 3\pi/4$ and a state with $\theta = 5\pi/4$. It is obvious that the state with $\theta = 3\pi/4$ has a larger integrated $\langle S_- \rangle$ value, which in turn reduces the amplitude of the superradiant burst. This also makes sense intuitively because in this case the dynamics have to “slow down” close to the equator. The drive and the decay have opposite signs in the evolution of the $\langle S_z \rangle$-component, which keeps the spins close to the equator for an extended period of time.

For a drive that brings the spins further than full inversion, this effect is reversed, as the spins do not have to slow down but rather only speed up through the decay process towards their ground state. The smaller decoherence and dephasing in the system the less this effect is pronounced.

Enhanced Decay

If we now take a closer look at experimental data and an individual trace for maximum inversion we see the expected behavior: We drive the system until the system reaches full inversion. After that the cavity empties itself very fast (since we are working in a fast cavity), but the excitations stay in the spin system for an extended period of time. Some fluctuations (be it thermal, quantum or seeded polarization) drive the system then out of the metastable equilibrium position – something that is comparable to a

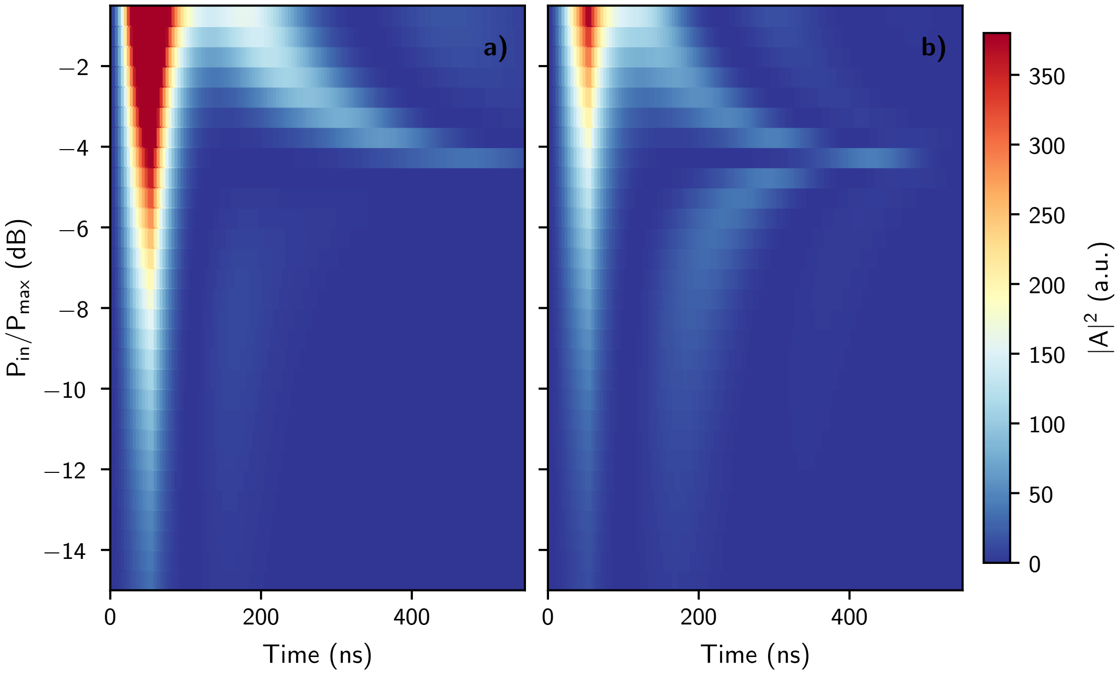

Figure 4.13: Numerical solution of the intra-cavity intensity for Eq. (2.49) for the same parameters as in the experiment, but once with (**a**) and without (**b**) in-homogeneous broadening. For the case of in-homogeneous broadening we see the same asymmetry as in the experiment, whereas for the non broadened case we see a symmetric structure around the maximum inversion, as explained in the main text.

pendulum that is turned upside down – and the spins decay with a fast rate, while emitting a lot of photons into the cavity mode at the same time.

As explained earlier, the optical transition in the NV center also allows us to measure the spin inversion directly, as is shown in Fig. 4.15 as blue trace. This confirms that the decay of the spin is fastest when a maximum of photons are emitted from the system and that the spins stay excited for an extended period of time after the microwave pulse is turned off. The maximum decay rate is 16 orders of magnitude faster than the single spin Purcell rate. This can be approximated by fitting the trace by Eq. (4.52), and looking at the maximum slope of this function. This gives a maximum decay rate of $\Gamma_{sr} \approx 17\,\text{MHz}$; an increase of more than 16 orders of magnitude compared to the Purcell enhancement for a single spin.

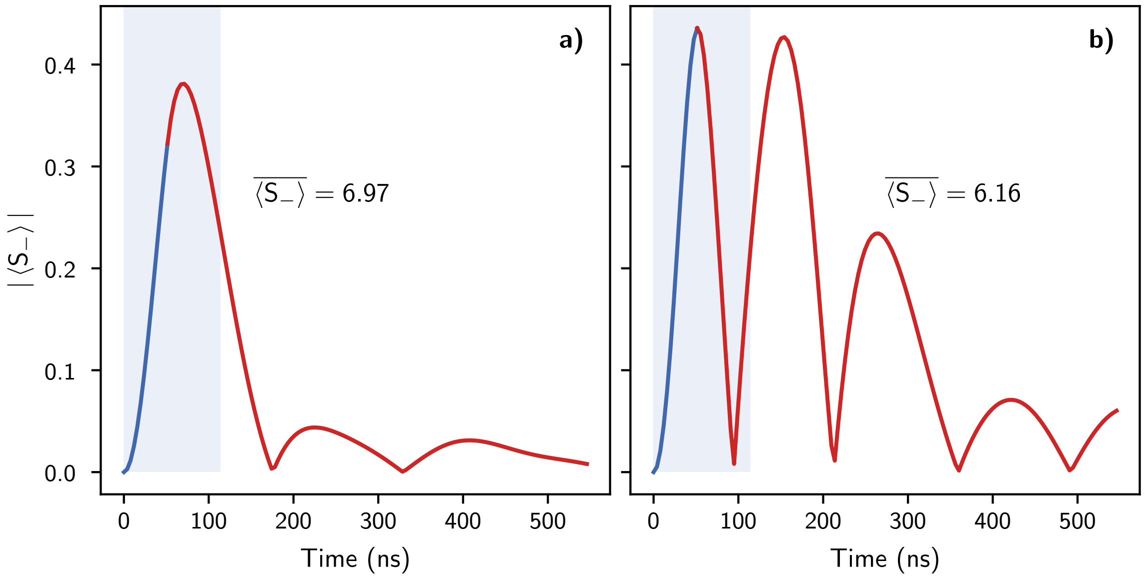

Figure 4.14: $|\langle S_- \rangle|$ values for traces for inclination of **(a)** $\theta = 3\pi/4$ and **(b)** $\theta = 5\pi/4$. Shown are the integrated values of the $\langle S_- \rangle$ up until the time when both traces reach the inversion corresponding to this inclination (shaded gray area). As it can be seen from this simulation, due to the fact that the state with smaller inclination has a larger integrated $\langle S_- \rangle$ value, it makes sense that decoherence and dephasing have a stronger effect, reducing the intensity of the emitted radiation.

Non-linear Scaling

The enhanced decay and the nice accordance with the expected behavior gives strong evidence of the superradiant nature of the emitted light, but in order to claim non-linear behavior we have to explicitly show the non-linearity. Fortunately the NV center allows to intrinsically change the number of emitters that is coupled to the cavity mode by applying different magnetic fields as explained in Section 3.2.1. By doing so and adjusting the power such that we get maximum inversion for all of these four cases we can study the emitted radiation for all of them.

As it turns out the emitted power for these four cases indeed shows a non-linear behavior, i.e. the emitted radiation intensity does not scale linearly ($P_{\text{emitted}} \not\propto N$). In Fig. 4.16 we show the non-linearity. It is apparent that the radiation does not scale linearly but exhibits a scaling that is proportional to $P_{\text{emitted}} \propto N^{1.52}$. The scaling is not N^2 as it would be expected from perfect superradiance, but this we can mainly attribute to the fact that we are not working deep enough in the bad cavity limit. The approximations in Section 4.2.2 that provide the N^2 scaling are only valid in the

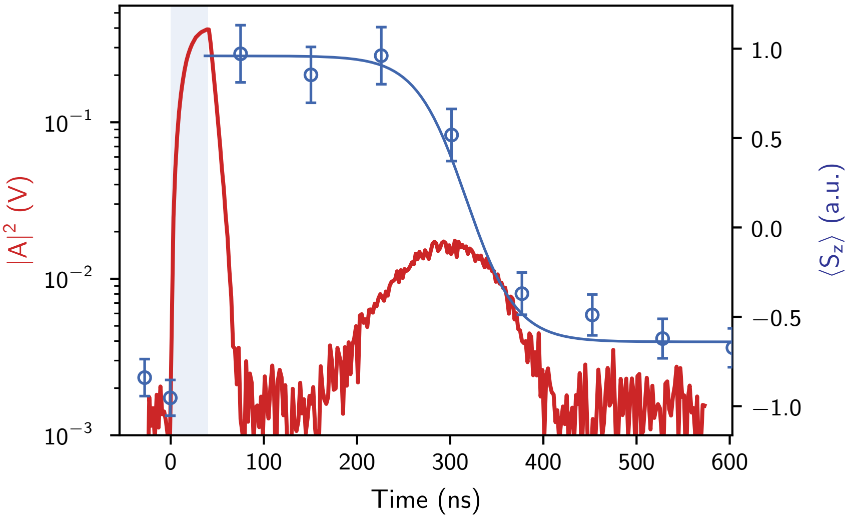

Figure 4.15: The red measurement curve shows a detailed view of the trace for the emitted photon intensity with three NV sub-ensembles in resonance with the cavity and where the inversion of the spin ensemble is maximum (depicted as a black dashed line in Fig. 4.12). The shaded area is the time for which the excitation drive is turned on. Shown in blue is the dynamics of the spin inversion, measured using the optical transition of the NV center and the inversion polarization normalized to the number of spins. After maximum inversion is reached the spins remain in a metastable state until fluctuations lead to a superradiant decay. This is accompanied by a burst of photons that builds up in the cavity mode. The blue solid line represents a fit of the fluorescence data according to a hyperbolic tangent as in Eq. (4.52). (Source [89])

limit of a perfect vacuum, and operating in the cavity changes this scaling factor [122]. Further, the more sub-ensembles have to be brought in resonance with the cavity mode the harder it becomes to align the magnetic fields exactly. If the magnetic fields are slightly mistuned, this leads to an additional line-broadening which again leads to more dephasing and reduces the amplitude of the emitted burst for more sub-ensembles in resonance.

Nonetheless, the non-linear scaling shows that the observed effect cannot be explained in the framework of the Holstein-Primakoff approximation and is, thus, a clear signature of non-linear physics in this system.

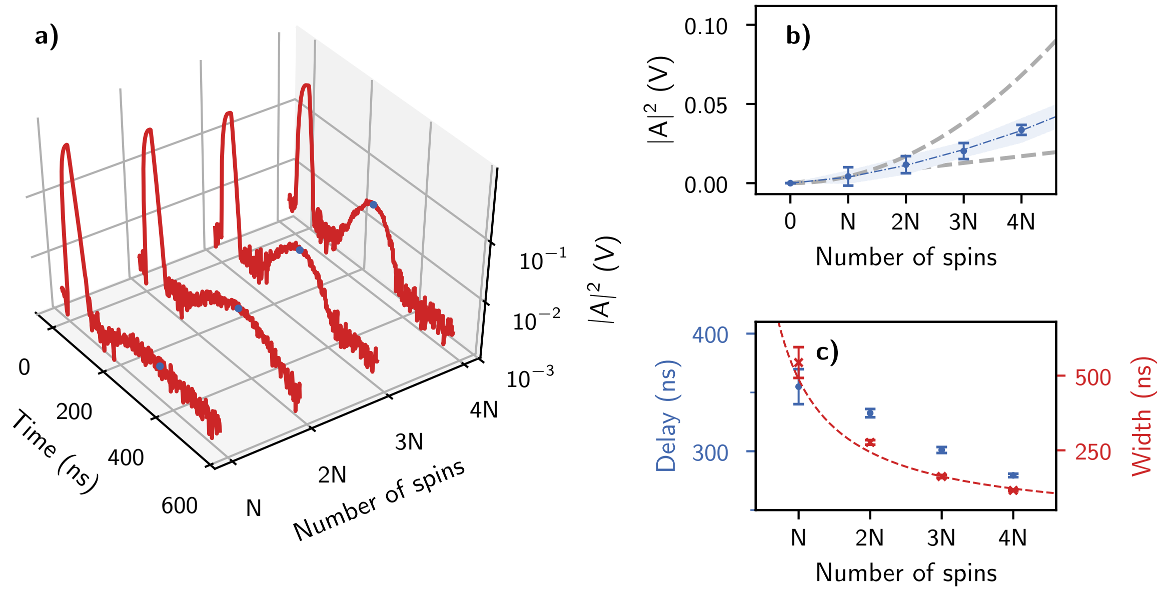

Figure 4.16: **a)** Measurement of either N, $2N$, $3N$ or $4N$ spins in resonance with the cavity mode showing the dependence of the emitted photon intensity on the number of spins. Depicted here are the traces for each of these cases where maximum inversion is reached, and a microwave drive duration of 50 ns, with the blue dots indicating the maximum power of the emitted radiation intensity. **b)** By measuring the maximum value of the emitted intensity we observe the nonlinear scaling of $|A|^2 \propto N^{1.52}$. The dashed gray lines show N and N^2 scaling. **c)** The delay and the width of the superradiant burst as functions of the number of spins. The width of the pulse can be modeled by Eq. (4.54), and shows the expected $1/N$ dependence. The delay of the burst does not closely follow Eq. (4.51), since it is very sensitive to small deviations in the inclination angle, which are experimentally hard to prevent. Further, for smaller number of spins the theoretically predicted delay is much longer than other fluctuations driving the spins out of the metastable state earlier. (Source [89])

4.2.7 Outlook and Discussion

The presented experiment is one of the first experiments that shows superradiance in a solid-state system in the microwave regime. It has proven to be extremely difficult to show superradiance in such a system, because dephasing and decoherence processes usually destroy phase coherence, the ultimately most important thing to sustain for a superradiant enhancement. By using our newly developed 3D lumped element resonators and NV samples with remarkably small line-widths we were able to overcome these limitations and show real Dicke superradiance the first time in a solid state spin system. The enhanced radiation together with the non-linear scaling are clear evidence that we observe the effect.

Superradiance as an effect, will play a very important role in the development of quantum technologies, as it enables the development of technologies such as the superradiant maser or high precision sensors [123, 124] or even single microwave detectors and quantum batteries. Especially the NV center is a promising candidate for these applications as its interesting level structure – it offers an optical level that could be used for pumping a maser transition – and its long coherence provides a promising framework for implementation of them [69].

More experiments that study the nature of the emitted light are also of interest, since the emitted light most certainly exhibits quantum entanglement, which might give the possibility to observe non-classical states of light and/or spin squeezing. This would in turn be interesting for quantum entanglement experiments and/or high precision sensing applications.

5 Outlook and Conclusion

The two presented experiments both showed how we can design experiments to leave the well-known, and in a sense, well-understood linear regime of cavity QED. The common thing for both these experiments is that in order to leave this linear regime, especially for a large number of spins, strong driving of the system is necessary to achieve that. In the following concluding chapter we will introduce ideas and first implementations to make that easier by either using optimal control to improve the fidelity of pulses applied to the spin system and on the other hand a new and improved version of the 3D lumped element resonator to further increase the coupling strength of the spin ensemble to the cavity.

5.1 Optimal Control of a Hybrid System

For the superradiance experiment as introduced in Section 4.2, one of the most challenging parts was to achieve full inversion of the spin system in order to monitor the decay of such an inverted spin ensemble. The way we achieved that was to use simple rectangular pulses, as per construction they provide the maximum energy over the shortest period of time. On the other hand step functions are always smeared out by the cavity response and are not the most optimal way to achieve full inversion.

During the last decades big progress has been made in how to control a (potentially complex) system, in the framework of optimal control theory (OCT).

I will introduce here a very basic implementation of optimal control theory in a hybrid system (I'm by no means an expert in OCT), but I think that this can lead to important applications and could make the presented experiments much more convincing.

The goal of optimal control pulses in our setup would be to achieve full inversion of a spin system starting in the ground state with no photons in the cavity. According to Eq. (3.39) there are two drive amplitudes corresponding to the two quadratures of the microwave radiation we can use to manipulate our spin system. This large degree of freedom allows to efficiently manipulate the spin system, much better than simple rectangular pulses.

The most straightforward ansatz is then to use a Fourier series ansatz for both of these time dependent amplitudes

$$\begin{aligned} I(t) &= \sum_{j=1}^{n} I_j \sin\left(j\omega_g t\right) \\ Q(t) &= \sum_{j=1}^{n} Q_j \sin\left(j\omega_g t\right). \end{aligned} \tag{5.1}$$

That gives two time dependent amplitudes with arbitrary number of Fourier components n and base frequency ω_g. Note that this is only one simple ansatz (commonly known as CRAB ansatz [125] and used in one of our published experiments [126, 127]), but different basis functions or ways to produce pulses might give much better results.

To find the time dependent amplitudes we use a Metropolis algorithm [128] implemented in pythons scipy library as `scipy.optimize.basinhopping`, that searches for a minimum in a landscape with many local minima. Our fitness function is then simply $1 - \langle S_z \rangle$, which we need to minimize in order to achieve full inversion.

The most straightforward and "clean" way to optimize these kind of pulses would be directly on the experiment (direct optimal control), and try to optimize on the output of the experiment. This is, however, not possible in our implementation because we don't have direct access to the inversion (the quantity we want to optimize on), and therefore have to revert to optimization on simulations. Fortunately it is possible to model our experiment very precisely and numerics gives us an almost perfect agreement between theory and experiment [92] (see also Section 3.3.2). This can be achieved by modeling the in-homogeneous broadened spin density as ~ 1000 spins equally distributed over the frequency region of interest, with coupling strengths corresponding to the spectral density. This proven to be correct and useful way [92, 93] allows to include in-homogeneous broadening into the system of coupled differential equations given by Eq. (3.39), and solving 1000 differential equations is easily doable on modern computer hardware.

I present again here the figure showing a first implementation of such a pulse (Fig. 5.1b), for an input power that is much smaller than the necessary power to achieve full inversion, in order to confirm the agreement between theory and experiment. As stated already in Section 3.3.2, we see that the agreement between theory and experiment is almost perfect, which gives confidence that also the simulated inversion is accurate.

In Fig. 5.2 we then see the (predicted) behavior for the correct input power, which ideally should give 80% inversion. This is better by almost 30% compared to a simple

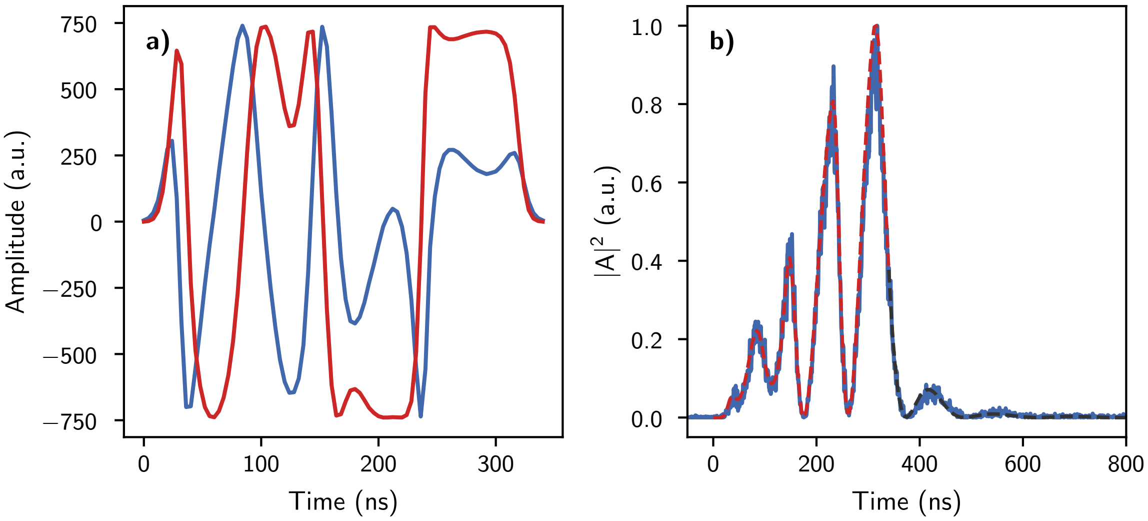

Figure 5.1: First implementation of an OCT pulse in our hybrid quantum system in the linear regime. In **a)** we see the pulse that is send into the cavity, generated by optimizing on maximum inversion after the pulse. In **b)** the resulting cavity amplitude is measured and compared to the simulation. The parameters for the simulation are as stated in Section 3.3.2.

rectangular pulse with the same input power and shows the advantage of using these kind of pulses over un-optimized pulses.

So far I was not able to show a perfectly successful implementation of these pulses, as it requires very precise control of the microwave radiation, something difficult to achieve experimentally. Also, the ever present in-homogeneity in the coupling strength, that, albeit mitigated by the 3D LER design, is still present, will make the agreement between theory and experiment smaller. Further, more understanding of the right ansatz and optimization routine is necessary to increase to convergence of these pulses.

This would allow to create arbitrary states for this system and definitely will allow for interesting future experiments, using inverted spin ensembles or even arbitrary initial states.

A fully inverted spin-ensemble would immediately lead to interesting applications like quantum batteries or weak microwave signal detectors, as technologies relying on an extremely non-linear system.

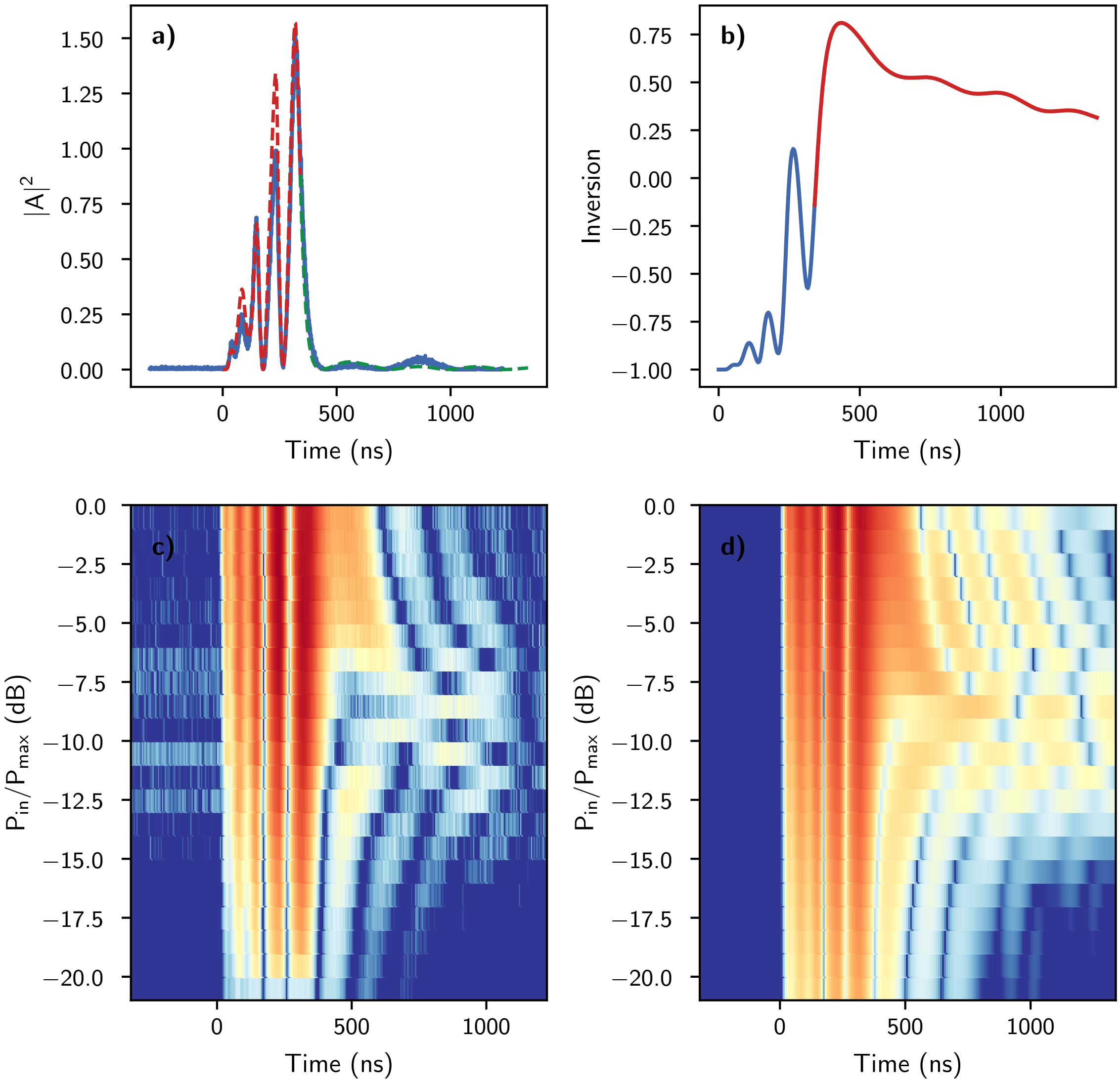

Figure 5.2: **c)** and **d)** show experimental results and numerical modeling of the intra-cavity intensity of a power scan performed with the pulse presented in Fig. 5.1. The agreement between theory and experiment is good, as can be seen in **a)**, where the cavity intensity for maximum inversion is plotted. The simulated inversion of the pulse is shown in **b)**. Compared to the linear regime (see Fig. 5.1) the agreement is still not satisfactory and further care has to be taken to control the experiment more precisely.

5.2 Loop Gap Resonators for Stronger Coupling

In both presented experiments the cooperativity value played a crucial role as it describes how strong the coupling is compared to the losses in the system. On a general

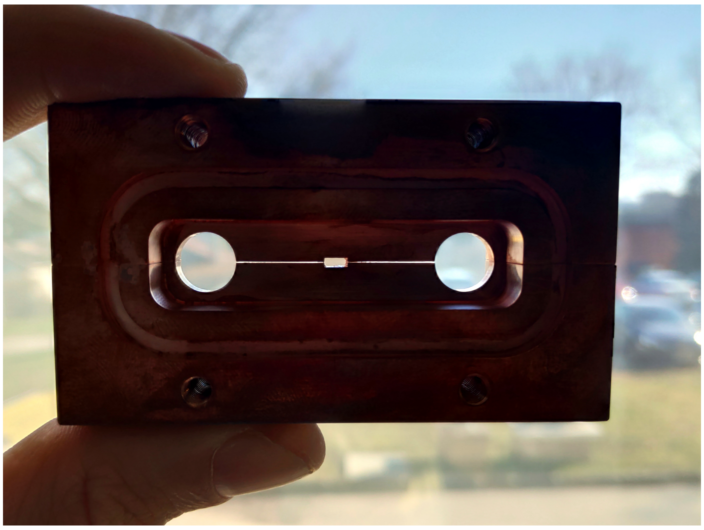

Figure 5.3: Photograph of the new resonator design, with an even smaller mode volume, and, therefore, stronger coupling. One can clearly see the capacitance as the small air-gap between top and bottom part. The diamond sample is placed in the hole in the middle. The two round circles on each site are necessary to close the magnetic field lines. Simulations show that an improvement in coupling of roughly a factor 5 is feasible.

level a higher cooperativity value is desired, as a stronger coupling usually leads to a stronger effect (cf. the cooperativity value in the bistability experiments). Moreover, the stronger the coupling, the more interesting fields of physics can be explored where for example the rotating wave approximation starts to break down.

The coupling of the spin system to the quantized mode of radiation is only determined by the mode volume and consequently by the current that is flowing in a resonator geometry as it is the quantity producing the magnetic field. As introduced in Section 3.1.3 our three-dimensional resonator design allows to do that and is a first step towards reducing the mode volume down to the minimum amount.

A design that is using the same principle of a 3D lumped element resonator but decreases the mode volume even further has been published by [129] in 2018. As we are also interested in stronger coupling we used this design to increase the coupling of our spin system to the cavity mode even further. Simulations and first tests show that an increase in coupling strength of a factor of approximately five is within reach, compared to our current 3D LER design.

In Fig. 5.3 we see the design of such a cavity, showing the building blocks for the discrete LC circuit that builds up the resonator. The small gaps act as the capacitor necessary for tuning the resonance frequency to a value reasonable for our experiments. Analogous to our design the inductance is simply given by the path the current has to go to close the circuit; in this case the path is closed around the two big holes in the design. These holes are also necessary because the magnetic field has to close its field lines, which are guided through these two holes on the left and right side and then through the smaller hole in the middle. Because of that all the magnetic field lines are forced to go through the relatively small hole in the middle, where the sample is then placed. This reduces the mode volume and therefore increases the coupling even further.

Further measurements have to be carried out, but first tentative results show that an improvement of roughly a factor of five in terms of coupling strength (albeit slightly smaller Q-values because of the higher current densities) is possible. This should improve the cooperativity value by the same amount and would allow to carry out more interesting experiments in the near future.

Higher Q-values by using dielectric materials instead of conducting materials might be another way to improve the cooperativity of the system while keeping all other parameters the same.

5.3 Conclusion

The presented work revealed fundamental physical effects in hybrid quantum systems. Contrary to most of the physics dealt with in these kind of systems, I have shown how it can be brought one step further, leaving the well understood linear regime of cavity QED and showing experiments where the Holstein-Primakoff approximation breaks down.

After introducing the theoretical framework in Section 2 and the setup to carry out the experiments in Section 3.3 I have shown two examples of experiments that show this non-linear behavior. First, an experiment showing amplitude bistability has been presented, one of the most fundamental experiments to show this non-linear behavior has given valuable insight. As one of the first experiments this implementation has allowed us to study the temporal behavior of the occurring phase transition something almost impossible with implementations so far. This also allowed us to extract a critical exponent for the phase transition. This effect gives important insight in fundamental physics, and could potentially find use in microwave switches or generation of squeezed microwave radiation.

The second experiment, dealt with one of the most important non-linear effects, namely superradiance, which has also sparked a lot of interest in the last few years as it is one of the effects that will lead to applications in quantum technology rather immediate. As one of the first implementations in a solid state system this is a milestone in solid state hybrid systems. Developments like superradiant masers or high sensitivity measurements are the next logical steps. Our implementation clearly shows that we indeed see superradiance with an improved decay rate of many orders of magnitude compared to a single spin and a clear non-linear scaling as another building block in non-linear cavity QED. Further experiments using optimal control theory and our newest resonator design will bring these experiments to a new level.

Many interesting experiments are still waiting to be explored, using different spin systems that couple much stronger than the NV centers; more dense samples showing the direct NV-NV interaction in the samples or experiments using the microwave to optical properties of the NV center.

I'm confident many more interesting things will be explored in this Lab!

List of Publications

Parts of this thesis have been published in the following publications:

- **"Collective strong coupling with homogeneous Rabi frequencies using a 3D lumped element microwave resonator"**
  Andreas Angerer, Thomas Astner, Daniel Wirtitsch, Hitoshi Sumiya, Shinobu Onoda, Junichi Isoya, Stefan Putz, and Johannes Majer
  Applied Physics Letters 109, 089901 (2016)
- **"Ultralong relaxation times in bistable hybrid quantum systems"**
  Andreas Angerer, Stefan Putz, Dmitry O. Krimer, Thomas Astner, Matthias Zens, Ralph Glattauer, Kirill Streltsov, William J. Munro, Kae Nemoto, Stefan Rotter, Jörg Schmiedmayer and Johannes Majer
  Science Advances (2017) Vol. 3, no. 12, e1701626
- **"Superradiant emission from colour centres in diamond"**
  Andreas Angerer, Kirill Streltsov, Thomas Astner, Stefan Putz, Hitoshi Sumiya, Shinobu Onoda, Junichi Isoya, William J. Munro, Kae Nemoto, Jörg Schmiedmayer, Johannes Majer
  Nature Physics 14, 1168–1172 (2018)

Other contributions have been made to:

- **"Spectral hole burning and its application in microwave photonics"**
  Stefan Putz, Andreas Angerer, Dmitry O. Krimer, Ralph Glattauer, William J. Munro, Stefan Rotter, Jörg Schmiedmayer and Johannes Majer
  Nature Photonics 11, 36–39 (2017)
- **"Solid-state electron spin lifetime limited by phononic vacuum modes"**
  Thomas Astner, Johannes Gugler, Andreas Angerer, Sebastian Wald, Stefan Putz, Norbert J. Mauser, Michael Trupke, Hitoshi Sumiya, Shinobu Onoda, Junichi Isoya, Jörg Schmiedmayer, Peter Mohn and Johannes Majer
  Nature Materials 17, 313–317 (2018)
- **"Coherent Coupling of Remote Spin Ensembles via a Cavity Bus"**
  Thomas Astner, Stefan Nevlacsil, Noomi Peterschofsky, Andreas Angerer, Stefan

Rotter, Stefan Putz, Jörg Schmiedmayer, and Johannes Majer
Physical Review Letters 118, 140502 (2017)

- **“Smooth Optimal Quantum Control for Robust Solid-State Spin Magnetometry”**
  Tobias Nöbauer, Andreas Angerer, Björn Bartels, Michael Trupke, Stefan Rotter, Jörg Schmiedmayer, Florian Mintert, and Johannes Majer
  Physical Review Letters 118, 140502 (2017)
- **“Subnanotesla quantum-interference magnetometry with a single spin in diamond”**
  Andreas Angerer, Tobias Nöbauer, Georg Wachter, Matthew L. Markham, Alastair Stacey, Johannes Majer, Jörg Schmiedmayer, Michael Trupke
  arXiv:1509.01637 [quant-ph] (2015)
- **“Creation of ensembles of nitrogen-vacancy centers in diamond by neutron and electron irradiation”**
  Tobias Nöbauer, Kathrin Buczak, Andreas Angerer, Stefan Putz, Georg Steinhauser, Johanna Akbarzadeh, Herwig Peterlik, Johannes Majer, Jörg Schmiedmayer, Michael Trupke
  arXiv:1309.0453 [quant-ph] (2014)
- **“Ab initio calculation of the spin lattice relaxation time T_1 for nitrogen-vacancy centers in diamond”**
  Johannes Gugler, Thomas Astner, Andreas Angerer, Jörg Schmiedmayer, Johannes Majer, and Peter Mohn
  Physical Review B 98, 214442

List of Figures

2.1 Representation of the quantized field inside two perfectly conducting walls. The boundary conditions force the electric field to be zero at 0 and L, whereas the strength of the magnetic field has to be maximum there. The electric field and magnetic field are perpendicular to each other and $\pi/2$ out of phase. 4

2.2 Jaynes-Cummings ladder for cavity and spin in resonance ($\omega_c = \omega_s = \omega$). In the n-excitation regime the coupled eigenstates are shifted by a factor $\propto \pm\sqrt{n}$ compared to the uncoupled eigenstates. 9

2.3 Dicke ladder for an ensemble of N spins. The leftmost states are the Dicke states, generated by applying the spin raising operator with N excitations and a total spin of $S = N/2$. Transitions between two Dicke states exist, as indicated by the red arrows. Dephasing leads to an evolution into the subradiant states that still decay within their subspace but with a smaller coupling to the electromagnetic field (blue shaded area) and a smaller total spin quantum number. Going up and down in this manifold is again possible with spin raising and lowering operators. The dark states are the ground states of their respective manifolds and cannot decay (red shaded area) since their transition matrix element to the real ground state is zero. 13

3.1 Simple schematic of a LC-circuit with inductance and capacitance in series. By putting charges into the circuit, they will oscillate with an eigenfrequency of $\omega = (LC)^{-1/2}$ between the capacitance and the inductance. 20

3.2 Rendering of a transmission line resonator as it is used in the experiment. On the left side the capacitance is shown that couples the resonator to its environment. The quantized mode is generated between two capacitors on both sides of the resonator. The center conductor is meandering in order to increase the overlap of the oscillating magnetic field with the sample which is placed on top of the resonator. On the right side the taper down to the central line is shown with the bonding to a copper PCB on the far right. 22

3.3 Picture of a transmission line resonator loaded with a diamond sample. The superconducting resonator is bonded in a printed circuit board, which is put in a closed copper box to avoid unwanted box resonances. The diamond sample is the black object in the center of the device. . . 22

3.4 **a)** Measured cavity response spectrum fitted with a Lorentzian line-shape according to Eq. (3.16). From the transmission spectrum we can easily deduce the line-width (i.e. κ) and the resonance frequency of of the cavity. **b)** Time response of the cavity under a 8 µs pulse on resonance. The time for which the MW drive is turned on is depicted as blue shaded area. The cavity field builds up and decays with a characteristic time constant given by the cavity line-width κ. The time response is equivalent to a Fourier transform of the spectrum as shown in a) and vice versa. 23

3.5 Transverse magnetic field distribution of a 2D resonator design showing the magnetic field generated by a single photon in the cavity mode. The black shaded area shows the niobium thin film with the center conductor in the middle and the ground plane on the outside. As can be seen from the plot, the magnetic field distribution is such that the magnetic field is almost exclusively focused to a region close to the surface of the thin film. Only spins close to the surface experience a strong effect of the magnetic field, whereas spins further away are almost not influenced. This produces a huge gradient in the individual coupling strengths and makes it impossible to coherently manipulate all spins at the same time. 24

3.6 Simulated field distribution inside a 3D box resonator. As visible from the arrows, the electric field (note that this analogous for the magnetic field) is uniformly pointing in one direction. Also the magnitude is very homogeneous in a wide area in the center of the cavity. However, the plot also shows that the resonator becomes bulky (see the black dashed lines denoting the dimensions of the cavity) for a resonance frequency of 3 GHz, and, due to its huge mode volume, also the coupling to a single spin is very small. 25

3.7 **a)** Photo of the 3D lumped element resonator design. Shown is a polished copper cavity with the top lid and the side walls removed for illustrative purposes. The diamond is placed in between the two metallic "bow-ties" as can be seen in the photo. **b)** A cut through the cavity, perpendicular to the direction of the mode. The two capacitors together with the inductance create an oscillating magnetic field focused in between the two metallic structures that is pointing out of the plane. The field is coupled into the mode with two pins, one for coupling into the mode, and the other one for measuring the transmission (Source [60]). 27

3.8 Equivalent circuit for the lumped element resonator. 50 Ω terminated input and output ports are coupled via two coupling capacitors (C_{coupl}) to the LC circuit. Inductors and capacitors are labeled according to Fig. 3.7b) (Source [60]). 27
3.9 Field distribution within the 3D lumped element resonator generated by a single photon in the cavity mode. The hatched area is where the diamond is located, and the contourlines show the RMS deviation of the coupling strength for 1%, 3%, 5% and 7%. 28
3.10 Transmission spectroscopy of the 3D lumped element resonator. Visible are two resonances with the lower one generally having slightly higher Q values (narrower line-width), but no magnetic field in the region of interest, and the higher one used in our experiments to couple the spins to. Apart from the two resonances no higher harmonics are present, with the box-modes at a much higher frequency. 29
3.11 Schematic representation of a cavity with input and output fields and losses as described in the main text. Since we drive the cavity only from the left side we omit b_{in}. 31
3.12 The structure of the NV center in the diamond lattice with its ground state term-scheme. **a)** The NV center consists of a nitrogen atom that replaces a carbon atom in the diamond lattice which then forms the NV center together with an adjacent vacancy. Plotted is the computed spin density, which shows that the electron of the NV center is mainly located close to the adjacent carbon atoms. **b)** The ground state level scheme of the NV center. The NV center exhibits a zero-field splitting (ZFS) of ≈ 2.88 GHz at low temperatures. A magnetic field allows to tune the $m_s = \pm 1$ states in order to change the transition energy and bringing them in resonance with the cavity mode (Picture taken from [53]). 34
3.13 Dependence of the NV resonance frequency depending on the direction and strength of an external bias field. Shown is the response of $m_s = 0$ to the higher energy excited state transition of the different sub-ensembles for three different magnetic field directions (see legend). For the $[1, 0, 0]$ direction all four sub-ensembles experience the same shift in the resonance frequency. For the $[1, 1, 1]$ direction 3+1 and for the $[1, 1, 0]$ direction 2+2 NV-sub-ensembles experience the same projection of the magnetic field on their quantization axis, respectively. 35
3.14 Fluorescence time traces for the two different spin projections with strong saturated excitation. The simulation is done using a simple five-level rate equation model with parameters taken from [81] 37

3.15 Term scheme of the NV center with the optical excited and ground state. Electrical dipole (i.e. optical photon emitting) transitions are indicated as solid (dark) red arrows with the transition rates written next to the dashed lines. The $m_s = 0$ state in the optical excited state almost exclusively decay back in the optical $m_s = 0$ state whereas the $m_s = \pm 1$ states primarily take the detour via a meta-stable state with a comparably long lifetime of $\approx 300\,\mathrm{ns}$. This gives a fluorescence difference (i.e. less directly emitted red photons) that we can use to distinguish the $m_s = 0$ from the $m_s = \pm 1$ states (Numbers taken from [80]). 38

3.16 Thermal polarization of the NV center over temperature. The thermal mean value of the S_Z^2 operator (blue curve) tells us how many spins are thermally polarized in the ground state. The red curve shows the value of $1 - \langle S_z \rangle$, which is a measure for how many spins are thermally polarized in the ground state. For temperatures $< 50\,\mathrm{mK}$ almost all spins are in the $m_s = 0$ i.e. the ground state, with the $\langle S_Z^2 \rangle$-value close to zero. For temperatures $T \to \infty$ the polarization into the $m_s = \pm 1$ states approaches $2/3$ and the spin system is in a completely mixed thermal state with the $m_s = 0$ and the $m_s = \pm 1$ states equally occupied. 39

3.17 **a)** Frequency response measurement scheme using a Vector Network Analyzer (VNA) to perform frequency spectrum measurements. The down-line to the resonator are heat-anchored on every stage to properly cool down the line. A low-noise amplifier (LNF) amplifies the signal coming out of the resonator, which is then fed back into the VNA, which then measures the forward scattering parameter $S21(\omega)$. **b)** Photograph of the lowest stage of the fridge showing three measurement setups, each with their respective 3D Helmholtz magnetic field cage (Source: [88]). . 42

3.18 Experimental setup for time resolved measurements showing our homodyne detection setup. A local oscillator (LO) frequency source sends in the probe tone which is split up with one arm going into the fridge and the other one used for reference. An IQ mixer modulates a signal from a fast AWG onto the carrier signal which is then amplified and sent into the fridge. The signal going through the fridge is down-modulated using the reference signal and recorded by a fast oscilloscope. Shown is also the optical detection scheme where a fast laser-diode provides short green laser pulses which are sent to the NV center using a multimode fiber. The scattered fluorescence is then collected by the same fiber and measured by an avalanche photo-diode (Source: [89]) 43

3.19 Discretization of the spin ensemble. Each frequency step ω_k is approximated by a rectangle with width $\Delta\omega$ for which the spin density is assumed to be constant (not to scale). 46

3.20 Comparison for experiment and theory. In **a)** we see the pulse that is send into the cavity, with non constant amplitude in both quadratures. In **b)** the resulting cavity amplitude is measured and compared to the simulation. Shown in blue is the experimental data, while the red curve shows the simulated cavity amplitude as long as the pulse is turned on, and the black dashed curve the simulated free evolution afterwards. The parameters for the simulation are as stated in the main text. 47

4.1 The two eigenmodes of a coupled harmonic oscillator system. The oscillators can be either in phase, oscillating in the same direction (upper plot), which corresponds to the symmetric eigenstate in the experiment, or out of phase, oscillating against each other, corresponding to the anti-symmetric eigenstate. In the case of these classical oscillators the anti-symmetric mode has the higher energy (contrary to our cavity-spin system) due to a negative sign in the coupling force. 51

4.2 **a)** Magnetic field spectroscopy on our hybrid system with two sub-ensembles in resonance with the cavity, showing the transmission through the cavity. By tuning the spins into resonance we see that the eigenstates split up with the maximum separation on resonance, for a magnetic field of 8.4 mT. **b)** Measured strong coupling with two (blue) or four (orange) sub-ensembles in resonance with the cavity. Increasing the number of spins by a factor of two corresponds to an increase in the splitting by a factor of $\sqrt{2}$. The two eigenstates ($|+\rangle$ and $|-\rangle$) are clearly distinguishable in both cases. The slight asymmetry in the peak height stems from a Fano resonance [101]. 52

4.3 **a)** Steady state bistability simulated according to Eq. (4.15) for different values of cooperativity ($C = 2, 8, 32, 128, 512, 2048$ from blue to red) for a single spin without detuning in resonance with the cavity mode. We observe that starting with a critical cooperativity of $C = 8$ the system starts to exhibit three stable solutions for one input power. This is the effect known as amplitude bistability. **b)** Measured steady state transmission spectra for different drive powers for two sub-ensembles in resonance with the cavity mode. For small drive powers the system behaves like two coupled harmonic oscillators, and exhibits normal mode splitting; for a certain critical drive power ($P_{\text{in}} = P_{\text{crit}}$) the splitting vanishes and only one peak is visible (note the green curve denoting the position of the maxima/maximum) (Source [103]) 56

4.4 Measurement of the steady-state bistability transmission through the cavity as a function of increasing (blue) and decreasing (red) input power P_{in}. In **a)**, the transmission measurements are plotted for the cooperativity value $C_{\mathrm{coll}} \approx 18$ using two sub-ensembles in resonance with the cavity, while partly quenching the cavity to lower the cooperativity value. **b)** Same transmission measurement with $C_{\mathrm{coll}} \approx 49$. A small bistable area is visible where the system evolves to different steady states depending on the history of the system in either the upper or lower branch. **c)** Same measurement as in a), with an increased cooperativity of $C_{\mathrm{coll}} \approx 78$ (by using all four NV sub-ensembles in resonance with the cavity). The dashed curves are numerical solutions of Eq. (4.8). The dashed lines in b) show the asymptotic solutions in the limit of large and small drive amplitudes η. Two critical values of the input power, at which a phase transition between two stable branches occurs, are characterized by a saddle-node bifurcation and labeled as P^{d}_{crit} and P^{u}_{crit}. For all three cases, a sketch of the corresponding potential is also depicted, which shows the occurrence of either one or two stable solutions (red and blue solid circles) and one unstable solution (in figures b) and c)) (green solid circles) for a fixed value of the input power P_{ref}. Tunneling through the potential barrier does not occur in our case because of the large system size such that the system does not switch back and forth between the steady states in the bistable area. (Source: [103]) 58

4.5 Simulated steady state solutions by solving Eq. (4.13) for the steady states for the reference power P_{ref}. For the simulation we use our system parameter and change the cooperativity by changing the collective coupling strength. We simulate with $n = 3001$ spins, a number sufficiently high enough to model our experiment. For a critical cooperativity of $C_{\mathrm{coll}} = 42.2$ the system starts to show more than one steady state, with the middle one unstable and impossible to prepare in the experiment. Which of the other stable fix-points the system tends towards is determined by the history of the system. Shown are also the measured values for the cavity amplitude as in Fig. 4.4 for the three cooperativity values presented there. As it is obvious from the plot the occurrence of the saddle node-bifurcation is very well reproduced by the experimental data. 60

4.6 Simulated behavior for a quench measurements solving the differential equation Eq. (4.21) for a cooperativity of 128 and $\gamma_{\|} = 0.0001$. As long as the system is driven harder than a critical drive power η^2_{crit} the system settles to a steady state in the upper branch. For drive powers lower than this critical drive the system relaxes to a steady state in the lower branch. Close to the critical drive the evolution becomes extremely slow and it takes an increasingly long time for the system to settle in a steady state. 63

4.7 **a)** Quench dynamics of the high cooperativity $C_{\text{coll}} \approx 78$ configuration and an initial state far in the strong driving branch. The transmission $|\mathrm{T}/\mathrm{T}_{\text{max}}|^2$ is plotted over time for different drive intensities where the time to reach a steady state strongly depends on the input intensity. For drive intensities larger than a critical drive value η_{crit} (defined as the power where the system undergoes the phase transition from the upper to the lower branch, the spin system remains saturated and sets into a state on the upper branch, whereas in the opposite case, the system evolves into a steady state on the lower branch. Close to the critical drive this time scale is extremely prolonged and approaches 4×10^4 s. The dashed lines correspond to full numerical simulations predicted from solving Eq. (4.18). The similarity to Fig. 4.6 is immediately apparent. **b)** The numerically calculated time derivative of the transmission through the cavity when doing a quench measurement as in a). The further away from the critical drive (either to high or too low), the faster the system evolves to a steady state. Close to the critical drive (small inset) the system can take arbitrarily long to reach a steady state, and the evolution becomes extremely slow. (Source [103]) 65

4.8 Time it takes for the system to undergo the phase transition from the strongly driven branch to the lower branch. We define the switching time (t_{trans}) as the inverse of the smallest gradient for a given curve extracted from Fig. 4.7. Close to the critical drive, the switching time diverges, and the time to reach a steady becomes arbitrarily long. The dashed blue line is a fitting function of the form $t_{\text{trans}} \approx |\eta^2 - \eta^2_{\text{crit}}|^\alpha$ with $\alpha = 1.20 \pm 0.04$. 66

4.9 **a)** Measured transmission spectrum for the case of one sub-ensemble in resonance with the cavity mode. We can fit the measured spectrum with the steady state solution of Eq. (2.49) (orange curve), which allows to reconstruct the coupling strength of 3.1 MHz and the spin density in **b)**, as well as all the other parameters such as the spin line-width and q-value. The cavity line-width we measure separately with the spins far detuned. We can also clearly observe the hyper-fine splitting of 2.8 MHz which becomes visible because of the small broadening of the individual lines. Note that in order to extract the coupling and spin line-width more precisely, this plot was done with a "good" cavity with $Q = 1200$, which puts the cavity far from the "fast" cavity limit. In order to increase the cavity line-width afterwards we only increased the input coupling, which in turn is not changing the coupling strength or the spin properties. 76

4.10 Thermal cavity occupation over temperature and a cavity frequency of 3 GHz. For low temperatures the thermal population is negligible, but even for higher temperatures the thermal population is as small as 2000 photons which is 12 orders of magnitude smaller than the number of spins in the ensemble. 78

4.11 **a)** Photograph of the cavity with a fiber glued onto the diamond sample. The diamond is illuminated with green laser light and the scattered red light is collected through the same fiber. **b)** The difference in fluorescence for the spins in the ground state (blue curve) before any microwave pulse was played, compared to the fluorescence after maximum inversion pulse was played (red curve). The measurement is averaged 500 times. The small difference in fluorescence makes it very hard to measure the population difference. 79

4.12 **a)** Intra-cavity intensity of a measurement where we apply a 50 ns MW pulse and continuously increase the power while monitoring the emitted radiation with three sub-ensembles in resonance with the cavity. At a power level of ≈ 5 dB attenuation of the maximum power available for the experiment (this is indicated by the black dashed line) we observe maximum inversion and see a (relatively strong) pulse being emitted from the cavity (the delay of this pulse is indicated by the green dashed line and is fitted according to Eq. (4.51)). For higher powers the delay of the burst becomes smaller, since excess photons in the cavity lead to stimulated emission (source [89]). **b)** Fluorescence measured directly after the MW pulse ended, to confirm that the inversion is maximum for an input power of −5 dB, which corresponds to the lowest fluorescence. 80

4.13 Numerical solution of the intra-cavity intensity for Eq. (2.49) for the same parameters as in the experiment, but once with (**a**) and without (**b**) in-homogeneous broadening. For the case of in-homogeneous broadening we see the same asymmetry as in the experiment, whereas for the non broadened case we see a symmetric structure around the maximum inversion, as explained in the main text. 83

4.14 $|\langle S_- \rangle|$ values for traces for inclination of (**a**) $\theta = 3\pi/4$ and (**b**) $\theta = 5\pi/4$. Shown are the integrated values of the $\langle S_- \rangle$ up until the time when both traces reach the inversion corresponding to this inclination (shaded gray area). As it can be seen from this simulation, due to the fact that the state with smaller inclination has a larger integrated $\langle S_- \rangle$ value, it makes sense that decoherence and dephasing have a stronger effect, reducing the intensity of the emitted radiation. 84

4.15 The red measurement curve shows a detailed view of the trace for the emitted photon intensity with three NV sub-ensembles in resonance with the cavity and where the inversion of the spin ensemble is maximum (depicted as a black dashed line in Fig. 4.12). The shaded area is the time for which the excitation drive is turned on. Shown in blue is the dynamics of the spin inversion, measured using the optical transition of the NV center and the inversion polarization normalized to the number of spins. After maximum inversion is reached the spins remain in a metastable state until fluctuations lead to a superradiant decay. This is accompanied by a burst of photons that builds up in the cavity mode. The blue solid line represents a fit of the fluorescence data according to a hyperbolic tangent as in Eq. (4.52). (Source [89]) 85

4.16 **a)** Measurement of either N, $2N$, $3N$ or $4N$ spins in resonance with the cavity mode showing the dependence of the emitted photon intensity on the number of spins. Depicted here are the traces for each of these cases where maximum inversion is reached, and a microwave drive duration of 50 ns, with the blue dots indicating the maximum power of the emitted radiation intensity. **b)** By measuring the maximum value of the emitted intensity we observe the nonlinear scaling of $|A|^2 \propto N^{1.52}$. The dashed gray lines show N and N^2 scaling. **c)** The delay and the width of the superradiant burst as functions of the number of spins. The width of the pulse can be modeled by Eq. (4.54), and shows the expected $1/N$ dependence. The delay of the burst does not closely follow Eq. (4.51), since it is very sensitive to small deviations in the inclination angle, which are experimentally hard to prevent. Further, for smaller number of spins the theoretically predicted delay is much longer than other fluctuations driving the spins out of the metastable state earlier. (Source [89]) 86

5.1 First implementation of an OCT pulse in our hybrid quantum system in the linear regime. In **a)** we see the pulse that is send into the cavity, generated by optimizing on maximum inversion after the pulse. In **b)** the resulting cavity amplitude is measured and compared to the simulation. The parameters for the simulation are as stated in Section 3.3.2. 91

5.2 **c)** and **d)** show experimental results and numerical modeling of the intra-cavity intensity of a power scan performed with the pulse presented in Fig. 5.1. The agreement between theory and experiment is good, as can be seen in **a)**, where the cavity intensity for maximum inversion is plotted. The simulated inversion of the pulse is shown in **b)**. Compared to the linear regime (see Fig. 5.1) the agreement is still not satisfactory and further care has to be taken to control the experiment more precisely. 92

5.3 Photograph of the new resonator design, with an even smaller mode volume, and, therefore, stronger coupling. One can clearly see the capacitance as the small air-gap between top and bottom part. The diamond sample is placed in the hole in the middle. The two round circles on each site are necessary to close the magnetic field lines. Simulations show that an improvement in coupling of roughly a factor 5 is feasible. 93

References

[1] Albert Einstein. “Über einen die Erzeugung und Verwandlung des Lichtes betreffenden heuristischen Gesichtspunkt”. In: *Annalen der physik* 322.6 (1905), pp. 132–148.

[2] Paul Adrien Maurice Dirac. “The quantum theory of the emission and absorption of radiation”. In: *Proceedings of the Royal Society of London. Series A, Containing Papers of a Mathematical and Physical Character* 114.767 (1927), pp. 243–265.

[3] Richard Phillips Feynman. *QED: the strange theory of light and matter.* OCLC: 1025427656. Princeton, N.J.: Princeton University Press, 2006.

[4] Herbert Walther, Benjamin T. H. Varcoe, Berthold-Georg Englert, and Thomas Becker. “Cavity quantum electrodynamics”. In: *Reports on Progress in Physics* 69 (May 2006), pp. 1325–1382. DOI: 10.1088/0034-4885/69/5/R02.

[5] R. J. Thompson, G. Rempe, and H. J. Kimble. “Observation of normal-mode splitting for an atom in an optical cavity”. In: *Physical Review Letters* 68.8 (Feb. 1992), pp. 1132–1135. DOI: 10.1103/PhysRevLett.68.1132.

[6] Gerhard Rempe, Herbert Walther, and Norbert Klein. “Observation of quantum collapse and revival in a one-atom maser”. In: *Physical Review Letters* 58.4 (Jan. 1987), pp. 353–356. DOI: 10.1103/PhysRevLett.58.353.

[7] J. M. Raimond, M. Brune, and S. Haroche. “Manipulating quantum entanglement with atoms and photons in a cavity”. In: *Reviews of Modern Physics* 73.3 (Aug. 2001), pp. 565–582. DOI: 10.1103/RevModPhys.73.565.

[8] David J. Wineland. “Nobel Lecture: Superposition, entanglement, and raising Schrödinger’s cat”. In: *Reviews of Modern Physics* 85.3 (July 2013), pp. 1103–1114. DOI: 10.1103/RevModPhys.85.1103.

[9] Serge Haroche. “Controlling Photons in a Box and Exploring the Quantum to Classical Boundary (Nobel Lecture)”. In: *Angewandte Chemie International Edition* 52.39 (Sept. 2013), pp. 10158–10178. DOI: 10.1002/anie.201302971.

[10] J. I. Cirac and P. Zoller. “Quantum Computations with Cold Trapped Ions”. In: *Physical Review Letters* 74.20 (May 1995), pp. 4091–4094. DOI: 10.1103/PhysRevLett.74.4091.

[11] Daniel Loss and David P. DiVincenzo. “Quantum computation with quantum dots”. In: *Physical Review A* 57.1 (Jan. 1998), pp. 120–126. DOI: 10.1103/PhysRevA.57.120.

[12] Immanuel Bloch, Jean Dalibard, and Sylvain Nascimbène. “Quantum simulations with ultracold quantum gases”. In: *Nature Physics* 8.4 (Apr. 2012), pp. 267–276. DOI: 10.1038/nphys2259.

[13] J. Kelly, R. Barends, A. G. Fowler, et al. “State preservation by repetitive error detection in a superconducting quantum circuit”. In: *Nature* 519.7541 (Mar. 2015), pp. 66–69. DOI: 10.1038/nature14270.

[14] K. Stannigel, P. Komar, S. J. M. Habraken, et al. “Optomechanical Quantum Information Processing with Photons and Phonons”. In: *Physical Review Letters* 109.1 (July 2012), p. 013603. DOI: 10.1103/PhysRevLett.109.013603.

[15] Alexei M. Tyryshkin, Shinichi Tojo, John J. L. Morton, et al. “Electron spin coherence exceeding seconds in high-purity silicon”. In: *Nature Materials* 11.2 (Feb. 2012), pp. 143–147. DOI: 10.1038/nmat3182.

[16] B. Hensen, H. Bernien, A. E. Dréau, et al. “Loophole-free Bell inequality violation using electron spins separated by 1.3 kilometres”. In: *Nature* 526.7575 (Oct. 2015), pp. 682–686. DOI: 10.1038/nature15759.

[17] H. J. Kimble, M. Dagenais, and L. Mandel. “Photon Antibunching in Resonance Fluorescence”. In: *Physical Review Letters* 39.11 (Sept. 1977), pp. 691–695. DOI: 10.1103/PhysRevLett.39.691.

[18] Jean-Claude Besse, Simone Gasparinetti, Michele C. Collodo, et al. “Single-Shot Quantum Nondemolition Detection of Individual Itinerant Microwave Photons”. In: *Physical Review X* 8.2 (Apr. 2018), p. 021003. DOI: 10.1103/PhysRevX.8.021003.

[19] P. Michler, A. Kiraz, C. Becher, et al. “A Quantum Dot Single-Photon Turnstile Device”. In: *Science* 290.5500 (Dec. 2000), pp. 2282–2285. DOI: 10.1126/science.290.5500.2282.

[20] Kunihiro Inomata, Zhirong Lin, Kazuki Koshino, et al. “Single microwave-photon detector using an artificial Λ-type three-level system”. In: *Nature Communications* 7 (July 2016), p. 12303. DOI: 10.1038/ncomms12303.

[21] Tomoyuki Yoshie, Lingling Tang, and Shu-Yu Su. “Optical Microcavity: Sensing down to Single Molecules and Atoms”. In: *Sensors (Basel, Switzerland)* 11.2 (Feb. 2011), pp. 1972–1991. DOI: 10.3390/s110201972.

[22] S. Forstner, S. Prams, J. Knittel, et al. “Cavity Optomechanical Magnetometer”. In: *Physical Review Letters* 108.12 (Mar. 2012), p. 120801. DOI: 10.1103/PhysRevLett.108.120801.

[23] K. Jensen, N. Leefer, A. Jarmola, et al. “Cavity-Enhanced Room-Temperature Magnetometry Using Absorption by Nitrogen-Vacancy Centers in Diamond”. In: *Physical Review Letters* 112.16 (Apr. 2014), p. 160802. DOI: 10.1103/PhysRevLett.112.160802.

[24] Atac Imamoğlu. “Cavity QED based on collective magnetic dipole coupling: spin ensembles as hybrid two-level systems”. In: *Physical review letters* 102.8 (2009), p. 083602.

[25] Gershon Kurizki, Patrice Bertet, Yuimaru Kubo, et al. “Quantum technologies with hybrid systems”. In: *Proceedings of the National Academy of Sciences* 112.13 (2015), pp. 3866–3873.

[26] J Verdú, H Zoubi, Ch Koller, et al. “Strong magnetic coupling of an ultracold gas to a superconducting waveguide cavity”. In: *Physical review letters* 103.4 (2009), p. 043603.

[27] M. Afzelius, I. Usmani, A. Amari, et al. “Demonstration of Atomic Frequency Comb Memory for Light with Spin-Wave Storage”. In: *Physical Review Letters* 104.4 (2010), p. 040503. DOI: 10.1103/PhysRevLett.104.040503.

[28] Hua Wu, Richard E. George, Janus H. Wesenberg, et al. “Storage of Multiple Coherent Microwave Excitations in an Electron Spin Ensemble”. In: *Physical Review Letters* 105.14 (Sept. 2010), p. 140503. DOI: 10.1103/PhysRevLett.105.140503.

[29] Y. Kubo, F. R. Ong, P. Bertet, et al. “Strong Coupling of a Spin Ensemble to a Superconducting Resonator”. In: *Physical Review Letters* 105.14 (Sept. 2010), p. 140502. DOI: 10.1103/PhysRevLett.105.140502.

[30] R. Amsüss, Ch. Koller, T. Nöbauer, et al. “Cavity QED with Magnetically Coupled Collective Spin States”. In: *Physical Review Letters* 107.6 (Aug. 2011), p. 060502. DOI: 10.1103/PhysRevLett.107.060502.

[31] Xiaobo Zhu, Shiro Saito, Alexander Kemp, et al. “Coherent coupling of a superconducting flux qubit to an electron spin ensemble in diamond”. In: *Nature* 478.7368 (Oct. 2011), pp. 221–224. DOI: 10.1038/nature10462.

[32] D. I. Schuster, A. P. Sears, E. Ginossar, et al. “High-Cooperativity Coupling of Electron-Spin Ensembles to Superconducting Cavities”. In: *Physical Review Letters* 105.14 (Sept. 2010), p. 140501. DOI: 10.1103/PhysRevLett.105.140501.

[33] S. Probst, H. Rotzinger, S. Wünsch, et al. “Anisotropic Rare-Earth Spin Ensemble Strongly Coupled to a Superconducting Resonator”. In: *Physical Review Letters* 110.15 (Apr. 2013), p. 157001. DOI: 10.1103/PhysRevLett.110.157001.

[34] Christoph W. Zollitsch, Kai Mueller, David P. Franke, et al. “High cooperativity coupling between a phosphorus donor spin ensemble and a superconducting microwave resonator”. In: *Applied Physics Letters* 107.14 (Oct. 2015), p. 142105. DOI: 10.1063/1.4932658.

[35] Yutaka Tabuchi, Seiichiro Ishino, Atsushi Noguchi, et al. “Coherent coupling between a ferromagnetic magnon and a superconducting qubit”. In: *Science* 349.6246 (July 2015), pp. 405–408. DOI: 10.1126/science.aaa3693.

[36] T. Holstein and H. Primakoff. “Field Dependence of the Intrinsic Domain Magnetization of a Ferromagnet”. In: *Physical Review* 58.12 (Dec. 1940), pp. 1098–1113. DOI: 10.1103/PhysRev.58.1098.

[37] R. P. Feynman. “The Development of the Space-Time View of Quantum Electrodynamics”. In: *Science* 153.3737 (Aug. 1966), pp. 699–708. DOI: 10.1126/science.153.3737.699.

[38] Julian Schwinger. “Relativistic Quantum Field Theory”. In: *Science* 153.3739 (Aug. 1966), pp. 949–953. DOI: 10.1126/science.153.3739.949.

[39] Shin’ichiro Tomonaga. “Development of quantum electrodynamics”. In: *Physics Today* 19.9 (Sept. 1966), pp. 25–32. DOI: 10.1063/1.3048465.

[40] Mark Fox. *Quantum optics: an introduction*. Oxford master series in physics 15. Oxford ; New York: Oxford University Press, 2006.

[41] Marlan O. Scully. *Quantum Optics*. Cambridge University Press, Sept. 1997.

[42] John David Jackson. *Classical Electrodynamics*. 3. New York: Wiley, 1998.

[43] Christopher Gerry and Peter Knight. *Introductory Quantum Optics*. Cambridge, UK ; New York: Cambridge University Press, Nov. 2004.

[44] Howard J. Carmichael. *Statistical Methods in Quantum Optics 2: Non-Classical Fields*. Softcover reprint of hardcover 1st ed. 2008. Berlin: Springer, Nov. 2010.

[45] Roy J. Glauber. “Coherent and Incoherent States of the Radiation Field”. In: *Physical Review* 131.6 (Sept. 1963), pp. 2766–2788. DOI: 10.1103/PhysRev.131.2766.

[46] D. F. Walls and Gerard J. Milburn. *Quantum Optics*. 2nd ed. Berlin Heidelberg: Springer-Verlag, 2008.

[47] E. T. Jaynes and F. W. Cummings. “Comparison of quantum and semiclassical radiation theories with application to the beam maser”. In: *Proceedings of the IEEE* 51.1 (Jan. 1963), pp. 89–109. DOI: 10.1109/PROC.1963.1664.

[48] M. Gross and S. Haroche. “Superradiance: An essay on the theory of collective spontaneous emission”. In: *Physics Reports* 93.5 (Dec. 1982), pp. 301–396. DOI: 10.1016/0370-1573(82)90102-8.

[49] Michael Tavis and Frederick W. Cummings. “Exact Solution for an N-Molecule – Radiation Field Hamiltonian”. In: *Physical Review* 170.2 (June 1968), pp. 379–384. DOI: 10.1103/PhysRev.170.379.

[50] R. H. Dicke. “Coherence in Spontaneous Radiation Processes”. In: *Physical Review* 93.1 (Jan. 1954), pp. 99–110. DOI: 10.1103/PhysRev.93.99.

[51] Garraway Barry M. “The Dicke model in quantum optics: Dicke model revisited”. In: *Philosophical Transactions of the Royal Society A: Mathematical, Physical and Engineering Sciences* 369.1939 (Mar. 2011), pp. 1137–1155. DOI: 10.1098/rsta.2010.0333.

[52] Howard J. Carmichael. *Statistical Methods in Quantum Optics 1: Master Equations and Fokker-Planck Equations*. Theoretical and Mathematical Physics, Statistical Methods in Quantum Optics. Berlin Heidelberg: Springer-Verlag, 1999.

[53] T. Astner, J. Gugler, A. Angerer, et al. “Solid-state electron spin lifetime limited by phononic vacuum modes”. In: *Nature Materials* 17.4 (Apr. 2018), p. 313. DOI: 10.1038/s41563-017-0008-y.

[54] C. Koller. “Towards the experimental realization of hybrid quantum systems”. In: (2012).

[55] M. Hatridge, S. Shankar, M. Mirrahimi, et al. "Quantum Back-Action of an Individual Variable-Strength Measurement". In: *Science* 339.6116 (Jan. 2013), pp. 178–181. DOI: 10.1126/science.1226897.

[56] Chen Wang, Yvonne Y. Gao, Philip Reinhold, et al. "A Schrödinger cat living in two boxes". In: *Science* 352.6289 (May 2016), pp. 1087–1091. DOI: 10.1126/science.aaf2941.

[57] Hanhee Paik, D. I. Schuster, Lev S. Bishop, et al. "Observation of High Coherence in Josephson Junction Qubits Measured in a Three-Dimensional Circuit QED Architecture". In: *Physical Review Letters* 107.24 (Dec. 2011), p. 240501. DOI: 10.1103/PhysRevLett.107.240501.

[58] C. Axline, M. Reagor, R. Heeres, et al. "An architecture for integrating planar and 3D cQED devices". In: *Applied Physics Letters* 109.4 (July 2016), p. 042601. DOI: 10.1063/1.4959241.

[59] David M. Pozar. *Microwave Engineering*. 4. Hoboken, NJ: Wiley, 2011.

[60] Andreas Angerer, Thomas Astner, Daniel Wirtitsch, et al. "Collective strong coupling with homogeneous Rabi frequencies using a 3D lumped element microwave resonator". In: *Applied Physics Letters* 109.3 (July 2016), p. 033508. DOI: 10.1063/1.4959095.

[61] Brian C. Wadell. *Transmission Line Design Handbook*. Boston: ARTECH HOUSE INC, 1991.

[62] Crispin Gardiner and Peter Zoller. *Quantum Noise: A Handbook of Markovian and Non-Markovian Quantum Stochastic Methods with Applications to Quantum Optics*. 3rd ed. Springer Series in Synergetics. Berlin Heidelberg: Springer-Verlag, 2004.

[63] C. W. Gardiner and M. J. Collett. "Input and output in damped quantum systems: Quantum stochastic differential equations and the master equation". In: *Physical Review A* 31.6 (June 1985), pp. 3761–3774. DOI: 10.1103/PhysRevA.31.3761.

[64] Alexander Stark, Nati Aharon, Thomas Unden, et al. "Narrow-bandwidth sensing of high-frequency fields with continuous dynamical decoupling". In: *Nature Communications* 8.1 (Oct. 2017), p. 1105. DOI: 10.1038/s41467-017-01159-2.

[65] F. Dolde, H. Fedder, M. W. Doherty, et al. "Electric-field sensing using single diamond spins". In: *Nature Physics* 7.6 (June 2011), pp. 459–463. DOI: 10.1038/nphys1969.

[66] E. L. Rosenfeld, L. M. Pham, M. D. Lukin, and R. L. Walsworth. "Sensing Coherent Dynamics of Electronic Spin Clusters in Solids". In: *Physical Review Letters* 120.24 (June 2018), p. 243604. DOI: 10.1103/PhysRevLett.120.243604.

[67] Nanyang Xu, Fengjian Jiang, Yu Tian, et al. "Wavelet-based fast time-resolved magnetic sensing with electronic spins in diamond". In: *Physical Review B* 93.16 (Apr. 2016), p. 161117. DOI: 10.1103/PhysRevB.93.161117.

[68] V. M. Acosta, K. Jensen, C. Santori, D. Budker, and R. G. Beausoleil. “Electromagnetically Induced Transparency in a Diamond Spin Ensemble Enables All-Optical Electromagnetic Field Sensing”. In: *Physical Review Letters* 110.21 (May 2013), p. 213605. DOI: 10.1103/PhysRevLett.110.213605.

[69] Liang Jin, Matthias Pfender, Nabeel Aslam, et al. “Proposal for a room-temperature diamond maser”. In: *Nature Communications* 6 (Sept. 2015), p. 8251. DOI: 10.1038/ncomms9251.

[70] Alison Mainwood. “Nitrogen and nitrogen-vacancy complexes and their formation in diamond”. In: *Physical Review B* 49.12 (Mar. 1994), pp. 7934–7940. DOI: 10.1103/PhysRevB.49.7934.

[71] Tobias Nöbauer, Kathrin Buczak, Andreas Angerer, et al. “Creation of ensembles of nitrogen-vacancy centers in diamond by neutron and electron irradiation”. In: *arXiv:1309.0453 [cond-mat, physics:quant-ph]* (Sept. 2013).

[72] Thomas Wolf, Philipp Neumann, Kazuo Nakamura, et al. “Subpicotesla Diamond Magnetometry”. In: *Physical Review X* 5.4 (Oct. 2015), p. 041001. DOI: 10.1103/PhysRevX.5.041001.

[73] Gopalakrishnan Balasubramanian, Philipp Neumann, Daniel Twitchen, et al. “Ultralong spin coherence time in isotopically engineered diamond”. In: *Nature Materials* 8.5 (May 2009), pp. 383–387. DOI: 10.1038/nmat2420.

[74] J. R. Maze, A. Gali, E. Togan, et al. “Properties of nitrogen-vacancy centers in diamond: the group theoretic approach”. In: *New Journal of Physics* 13.2 (Feb. 2011), p. 025025. DOI: 10.1088/1367-2630/13/2/025025.

[75] V. M. Acosta, A. Jarmola, E. Bauch, and D. Budker. “Optical properties of the nitrogen-vacancy singlet levels in diamond”. In: *Physical Review B* 82.20 (Nov. 2010), p. 201202. DOI: 10.1103/PhysRevB.82.201202.

[76] N. M. Atherton. *Principles of electron spin resonance*. Ellis Horwood series in physical chemistry. Chichester: Ellis Horwood, 1993.

[77] F. Jelezko and J. Wrachtrup. “Single defect centres in diamond: A review”. In: *physica status solidi (a)* 203.13 (Oct. 2006), pp. 3207–3225. DOI: 10.1002/pssa.200671403.

[78] L. Rondin, J.-P. Tetienne, T. Hingant, et al. “Magnetometry with nitrogen-vacancy defects in diamond”. In: *Reports on Progress in Physics* 77.5 (May 2014), p. 056503. DOI: 10.1088/0034-4885/77/5/056503.

[79] M. Lesik, T. Plays, A. Tallaire, et al. “Preferential orientation of NV defects in CVD diamond films grown on (113)-oriented substrates”. In: *Diamond and Related Materials* 56 (June 2015), pp. 47–53. DOI: 10.1016/j.diamond.2015.05.003.

[80] Tobias Nöbauer. *Sensing, coherent coupling and optimal control with nitrogen-vacancy colour centres in diamond*. 2013.

[81] Lilian Isabel Childress. “Coherent manipulation of single quantum systems in the solid state”. In: (2007), p. 188.

[82] Haixu Leng, Brian Szychowski, Marie-Christine Daniel, and Matthew Pelton. “Strong coupling and induced transparency at room temperature with single quantum dots and gap plasmons”. In: *Nature Communications* 9.1 (Oct. 2018), p. 4012. DOI: 10.1038/s41467-018-06450-4.

[83] Rohit Chikkaraddy, Bart de Nijs, Felix Benz, et al. “Single-molecule strong coupling at room temperature in plasmonic nanocavities”. In: *Nature* 535.7610 (July 2016), pp. 127–130. DOI: 10.1038/nature17974.

[84] Kathrin Sandner. *Cavity quantum electrodynamics with ultracold atoms and superconducting resonators*. 2012.

[85] K. Sandner, H. Ritsch, R. Amsüss, et al. “Strong magnetic coupling of an inhomogeneous nitrogen-vacancy ensemble to a cavity”. In: *Physical Review A* 85.5 (May 2012), p. 053806. DOI: 10.1103/PhysRevA.85.053806.

[86] Frank Pobell. *Matter and Methods at Low Temperatures*. 3rd ed. Berlin Heidelberg: Springer-Verlag, 2007.

[87] Kurt Uhlig. ““Dry” dilution refrigerator with pulse-tube precooling”. In: *Cryogenics* 44.1 (Jan. 2004), pp. 53–57. DOI: 10.1016/j.cryogenics.2003.07.007.

[88] Stefan Putz. *Circuit Cavity QED with Macroscopic Solid-State Spin Ensembles*. Springer Theses. Springer International Publishing, 2017.

[89] Andreas Angerer, Kirill Streltsov, Thomas Astner, et al. “Superradiant emission from colour centres in diamond”. In: *Nature Physics* (Sept. 2018), p. 1. DOI: 10.1038/s41567-018-0269-7.

[90] D. Le Sage, L. M. Pham, N. Bar-Gill, et al. “Efficient photon detection from color centers in a diamond optical waveguide”. In: *Physical Review B* 85.12 (Mar. 2012), p. 121202. DOI: 10.1103/PhysRevB.85.121202.

[91] Ferenc Marki and Christopher Marki. “A Tutorial for RF & Microwave Mixers”. In: (2010), p. 12.

[92] Dmitry O. Krimer, Stefan Putz, Johannes Majer, and Stefan Rotter. “Non-Markovian dynamics of a single-mode cavity strongly coupled to an inhomogeneously broadened spin ensemble”. In: *Physical Review A* 90.4 (Oct. 2014), p. 043852. DOI: 10.1103/PhysRevA.90.043852.

[93] S. Putz, D. O. Krimer, R. Amsüss, et al. “Protecting a spin ensemble against decoherence in the strong-coupling regime of cavity QED”. In: *Nature Physics* advance online publication (Aug. 2014). DOI: 10.1038/nphys3050.

[94] W. Casteels, F. Storme, A. Le Boité, and C. Ciuti. “Power laws in the dynamic hysteresis of quantum nonlinear photonic resonators”. In: *Physical Review A* 93.3 (Mar. 2016), p. 033824. DOI: 10.1103/PhysRevA.93.033824.

[95] R. Bonifacio and P. Meystre. “Transient response in optical bistability”. In: *Optics Communications* 27.1 (Oct. 1978), pp. 147–150. DOI: 10.1016/0030-4018(78)90195-5.

[96] Rahul Sawant and S. A. Rangwala. “Optical-bistability-enabled control of resonant light transmission for an atom-cavity system”. In: *Physical Review A* 93.2 (Feb. 2016), p. 023806. DOI: 10.1103/PhysRevA.93.023806.

[97] G. Rempe, R. J. Thompson, R. J. Brecha, W. D. Lee, and H. J. Kimble. “Optical bistability and photon statistics in cavity quantum electrodynamics”. In: *Physical Review Letters* 67.13 (Sept. 1991), pp. 1727–1730. DOI: 10.1103/PhysRevLett.67.1727.

[98] H. J. Kimble. “Strong Interactions of Single Atoms and Photons in Cavity QED”. In: *Physica Scripta* T76.1 (1998), p. 127. DOI: 10.1238/Physica.Topical.076a00127.

[99] Mihaly G. Benedict, ed. *Super-radiance: multiatomic coherent emission*. Optics and optoelectronics series. OCLC: 247127442. Bristol: Inst. of Physics Publ, 1996.

[100] András Dombi, András Vukics, and Peter Domokos. “Optical bistability in strong-coupling cavity QED with a few atoms”. In: *Journal of Physics B: Atomic, Molecular and Optical Physics* 46.22 (Nov. 2013). arXiv: 1305.6460, p. 224010. DOI: 10.1088/0953-4075/46/22/224010.

[101] U. Fano. “Effects of Configuration Interaction on Intensities and Phase Shifts”. In: *Physical Review* 124.6 (Dec. 1961), pp. 1866–1878. DOI: 10.1103/PhysRev.124.1866.

[102] M. J. Martin, D. Meiser, J. W. Thomsen, Jun Ye, and M. J. Holland. “Extreme nonlinear response of ultranarrow optical transitions in cavity QED for laser stabilization”. In: *Physical Review A* 84.6 (Dec. 2011), p. 063813. DOI: 10.1103/PhysRevA.84.063813.

[103] Andreas Angerer, Stefan Putz, Dmitry O. Krimer, et al. “Ultralong relaxation times in bistable hybrid quantum systems”. In: *Science Advances* 3.12 (Dec. 2017), e1701626. DOI: 10.1126/sciadv.1701626.

[104] Yuri Kuznetsov. *Elements of Applied Bifurcation Theory*. 3rd ed. Applied Mathematical Sciences. New York: Springer-Verlag, 2004.

[105] S. R. K. Rodriguez, W. Casteels, F. Storme, et al. “Probing a Dissipative Phase Transition via Dynamical Optical Hysteresis”. In: *Physical Review Letters* 118.24 (June 2017), p. 247402. DOI: 10.1103/PhysRevLett.118.247402.

[106] A. Szöke, V. Daneu, J. Goldhar, and N. A. Kurnit. “BISTABLE OPTICAL ELEMENT AND ITS APPLICATIONS”. In: *Applied Physics Letters* 15.11 (Dec. 1969), pp. 376–379. DOI: 10.1063/1.1652866.

[107] E. Garmire, J. H. Marburger, S. D. Allen, and H. G. Winful. “Transient response of hybrid bistable optical devices”. In: *Applied Physics Letters* 34.6 (Mar. 1979), pp. 374–376. DOI: 10.1063/1.90794.

[108] G. Grynberg and S. Cribier. “Critical exponents in dispersive optical bistability”. In: *Journal de Physique Lettres* 44.12 (June 1983), pp. 449–453. DOI: 10.1051/jphyslet:019830044012044900.

[109] Luigi Lugiato, Franco Prati, and Massimo Brambilla. *Nonlinear Optical Systems*. 1 edition. Cambridge, United Kingdom: Cambridge University Press, Apr. 2015.

[110] Steven H. Strogatz. *Nonlinear Dynamics And Chaos: With Applications To Physics, Biology, Chemistry, And Engineering*. Boulder (CO) etc.: Westview Press, Jan. 2001.

[111] Anatoli Polkovnikov, Krishnendu Sengupta, Alessandro Silva, and Mukund Vengalattore. "Colloquium: Nonequilibrium dynamics of closed interacting quantum systems". In: *Reviews of Modern Physics* 83.3 (Aug. 2011), pp. 863–883. DOI: 10.1103/RevModPhys.83.863.

[112] Claude Cohen-Tannoudji. *Atoms in Electromagnetic Fields*. Google-Books-ID: P6QdMag1a44C. World Scientific, 2004.

[113] D. Meiser, Jun Ye, D. R. Carlson, and M. J. Holland. "Prospects for a Millihertz-Linewidth Laser". In: *Physical Review Letters* 102.16 (Apr. 2009), p. 163601. DOI: 10.1103/PhysRevLett.102.163601.

[114] Nicolai ten Brinke and Ralf Schützhold. "Dicke superradiance as a nondestructive probe for quantum quenches in optical lattices". In: *Physical Review A* 92.1 (July 2015), p. 013617. DOI: 10.1103/PhysRevA.92.013617.

[115] Matthew A. Norcia, Matthew N. Winchester, Julia R. K. Cline, and James K. Thompson. "Superradiance on the millihertz linewidth strontium clock transition". In: *Science Advances* 2.10 (2016). DOI: 10.1126/sciadv.1601231.

[116] S. Inouye, A. P. Chikkatur, D. M. Stamper-Kurn, et al. "Superradiant Rayleigh Scattering from a Bose-Einstein Condensate". In: *Science* 285.5427 (July 1999), pp. 571–574. DOI: 10.1126/science.285.5427.571.

[117] B. C. Rose, A. M. Tyryshkin, H. Riemann, et al. "Coherent Rabi Dynamics of a Superradiant Spin Ensemble in a Microwave Cavity". In: *Physical Review X* 7.3 (July 2017), p. 031002. DOI: 10.1103/PhysRevX.7.031002.

[118] Vasily V. Temnov and Ulrike Woggon. "Superradiance and Subradiance in an Inhomogeneously Broadened Ensemble of Two-Level Systems Coupled to a Low-Q Cavity". In: *Physical Review Letters* 95.24 (Dec. 2005), p. 243602. DOI: 10.1103/PhysRevLett.95.243602.

[119] R. Jodoin and L. Mandel. "Superradiance in an inhomogeneously broadened atomic system". In: *Physical Review A* 9.2 (Feb. 1974), pp. 873–884. DOI: 10.1103/PhysRevA.9.873.

[120] A. Bienfait, J. J. Pla, Y. Kubo, X. Zhou, et al. "Controlling spin relaxation with a cavity". In: *Nature* 531.7592 (Mar. 2016), pp. 74–77. DOI: 10.1038/nature16944.

[121] G. Boero, G. Gualco, R. Lisowski, et al. "Room temperature strong coupling between a microwave oscillator and an ensemble of electron spins". In: *Journal of Magnetic Resonance* 231 (June 2013), pp. 133–140. DOI: 10.1016/j.jmr.2013.04.004.

[122] N. E. Nefedkin, E. S. Andrianov, A. A. Pukhov, and A. P. Vinogradov. "Superradiance enhancement by bad-cavity resonator". In: *Laser Physics* 27.6 (2017), p. 065201. DOI: 10.1088/1555-6611/aa6f6d.

[123] Joshua M. Weiner, Kevin C. Cox, Justin G. Bohnet, Zilong Chen, and James K. Thompson. "Superradiant Raman laser magnetometer". In: *Applied Physics Letters* 101.26 (Dec. 2012), p. 261107. DOI: 10.1063/1.4773241.

[124] A. Bienfait, J. J. Pla, Y. Kubo, M. Stern, et al. "Reaching the quantum limit of sensitivity in electron spin resonance". In: *Nature Nanotechnology* 11.3 (Mar. 2016), pp. 253–257. DOI: 10.1038/nnano.2015.282.

[125] Tommaso Caneva, Tommaso Calarco, and Simone Montangero. "Chopped random-basis quantum optimization". In: *Physical Review A* 84.2 (Aug. 2011), p. 022326. DOI: 10.1103/PhysRevA.84.022326.

[126] Tobias Nöbauer, Andreas Angerer, Björn Bartels, et al. "Smooth Optimal Quantum Control for Robust Solid-State Spin Magnetometry". In: *Physical Review Letters* 115.19 (Nov. 2015), p. 190801. DOI: 10.1103/PhysRevLett.115.190801.

[127] Björn Bartels and Florian Mintert. "Smooth optimal control with Floquet theory". In: *Physical Review A* 88.5 (Nov. 2013), p. 052315. DOI: 10.1103/PhysRevA.88.052315.

[128] Nicholas Metropolis, Arianna W. Rosenbluth, Marshall N. Rosenbluth, Augusta H. Teller, and Edward Teller. "Equation of State Calculations by Fast Computing Machines". In: *The Journal of Chemical Physics* 21.6 (June 1953), pp. 1087–1092. DOI: 10.1063/1.1699114.

[129] Jason R. Ball, Yu Yamashiro, Hitoshi Sumiya, et al. "Loop-gap microwave resonator for hybrid quantum systems". In: *Applied Physics Letters* 112.20 (May 2018), p. 204102. DOI: 10.1063/1.5025744.

Acknowledgements

A full PhD thesis cannot be done alone, and over the years a lot of people were immensely important to finish the thesis.

First I want to thank my supervisor Johannes Majer, who gave me the opportunity to work in this lab, and always gave me the freedom and support to follow my own ideas and do interesting physics. His knowledge about electronics, everything that is quantum and cold was really helpful. Also a big thanks to Jörg Schmiedmayer who offers this great work environment here at the Atominstitut. It is always a great pleasure to have unbelievably stimulating discussions about physics and get valuable input for my work. A big thanks also to Michael Trupke who brought me into the NV physics but also always was there when I had questions about any other fields in physics.

I also owe a thank you to Dmitry Krimer, Matthias Zens and Stefan Rotter. Our collaboration was extremely fruitful and I gained an immeasurable amount of insight and knowledge when discussing with them.

I would also like to thank Bill Munro and Kae Nemoto, with whom I was able to discuss a lot about my experiment and who were always there when I had questions. A lot of ideas that resulted in exciting physics had their starting points in discussions with them.

Of course the big part of the experiment has not been build by me, but I heavily relied on the previous work from Christian Koller and Robert Amsüß who started these experiments, and to which I owe a lot of gratitude for handing me over a phenomenally working experiment.

The people I owe probably most gratitude during my time here are first Tobias Nöbauer who I started to work with me in the beginning of my time here, and who was arguably the most influential person here for me. His in depth knowledge about physics in general and all things related to programming and NV centers specifically have been a perfect start for my time here; one could not wish for a better teacher to learn the way science works. Secondly Stefan Putz, with whom I was lucky enough to share the lab for two years, has been a great mentor during this time. I learned a lot from him what is the best way to tackle a problem, and his willingness to just “try it out" really just made it possible to discover a lot of the things I am presenting in this thesis.

Last but not least I want to of course also thank Thomas Astner, who has shared the lab with me almost during my whole time here. We learned a lot from each other, and it is always good to have a friend with whom you can discuss (not only about physics related things) and decide how to move forward. Wenzel Kersten has just recently joined the lab, and although our overlap has been short, still it was a tremendous pleasure to work with you. I think he is exactly the type of phyisicist this lab needs, with a lot of enthusiasm and will to do stuff.

The master students I was in charge of, namely Johannes Leitner, Ralph Glattauer and Kirill Streltsov, I would also like to thank a lot. The part of the job where I was able to teach something to someone else was truly one of the most rewarding moments, I hope I was able to offer that; I know that I learned a lot from them.

Writing a thesis s not possible without the support from family and friends. For that I especially want to thank Marine Pigneur, who made the last years of my PhD very special, life would look much darker without you. As you know it is quite tough to write a PhD thesis, and this work is also for you. I also would like to thank my family who always supported me in my endeavour to become a physicist, without this support it would be virtually impossible to do a PhD in physics.

During my five years here I had the possibility to share office with a lot of people, and it has been a great pleasure to do so. A big thanks to Qi Liang, with whom I shared an office for a year, and who taught me a lot about electronics and also Chinese culture. Later I shared an office with João Sabino and Andrew Kanagin. We had a lot of fun and discussing with the two of them (or one) always helped me when I had some problems I was not able to solve on my own. I would also like to thank all the other great people I met in this group, like Filippo Borselli with whom it is extremely easy to have a tremendous amount of fun, Mira Maiwöger who is one of the most intelligent people to talk to in the group, Federica Cataldini who is a bit the good soul of the atomchip group or Mohammadamin Tajik who has an amazing knowledge about physics he is more than willing to share. Of course there are many more people I should thank here, please feel included here.

Curriculum Vitae

Name: Andreas Angerer
Place of Birth: Lassing
Citizenship: Austria
Email: andreas.angerer89@gmail.com

- 1999-2007 / High school Stiftsgymnasium Admont / Austria
- 2007 / Begin of graduate studies of physics / TU Wien / Austria
- 2014 / End if graduate studies of physics / TU Wien / Austria
- 2014-2019 / Ph.D studies experimental solid-state physics / TU Wien / Austria